Technological developments for Laser Ion Acceleration

Christian Kreuzer

München 2018

Technological developments for Laser Ion Acceleration

Christian Kreuzer

Dissertation
an der Fakultät für Physik
der Ludwig–Maximilians–Universität
München

vorgelegt von
Christian Kreuzer
aus Illertissen

München, den 24.04.2018

Erstgutachter: Prof. Dr. Jörg Schreiber
Zweitgutachter: Prof. Dr. Ulrich Schramm
Tag der mündlichen Prüfung: 05.07.2018

Für meine Familie

Contents

Zusammenfassung **x**

1 Introduction **1**
1.1 Scientific context 1
1.1.1 Short laser pulses and high intensity 2
1.1.2 Laser Ion Acceleration 3
1.1.3 Technological challenges 6
1.2 Thesis outline 7

2 PW lasers: Infrastructure **9**
2.1 Laser infrastructure 9
2.1.1 Generation of intense ultra short laser pulses 9
2.1.2 Temporal laser contrast 11
2.1.3 Laser beam delivery 14
2.2 Experimental infrastructure 15
2.2.1 Targets for laser ion acceleration 15
2.2.2 Target characterization 20
2.2.3 Comparison of the production techniques 22
2.2.4 Target delivery and positioning system 22
2.3 Summary and conclusion 24

3 PW optics: Laser induced damage threshold Measurements **25**
3.1 Motivation 25
3.2 Theoretical understanding of laser induced damage 26
3.2.1 Laser parameters and definition of laser damage 26
3.2.2 Laser induced damage in dielectric materials 28
3.2.3 Laser damage in conducting materials 32
3.2.4 Multiple pulse damage 34
3.3 Experimental evaluation of laser induced damage threshold . . 37
3.3.1 Residual gas analysis of vacuum chamber 39
3.3.2 Measurement Procedure 41

3.3.3 Evaluation 42
3.4 Experimental results 47
3.4.1 Applicants for LBD mirror supply 48
3.4.2 Influence of vacuum on laser damage threshold 48
3.5 Damage threshold measurements of pulse compression gratings in vacuum 50
3.5.1 Surface contamination during measurements 51
3.6 Summary and conclusion 55

4 PW-lasers: Optical metrology 57
4.1 Introduction 57
4.2 Vacuum compatible camera development 58
4.2.1 Outgassing tests 59
4.2.2 Passive cooling for vacuum use 60
4.3 Electromagnetic pulse shielding of cameras in vacuum 61
4.4 Focus and target diagnostics in LION 64
4.5 Microscope setup 67
4.6 Target positioning and characterization 68
4.6.1 Whitelight interference microscopy 70
4.6.2 Theoretical background 70
4.6.3 Experimental realization of WLI and first tests 73
4.6.4 Spectral reflectance measurements 79
4.7 Laser characterization 82
4.7.1 Wavefront measurement 82
4.7.2 Laser focus diagnostic and dynamic range extension . . 88
4.8 Summary and conclusion 89
4.9 Final configuration for LION@CALA 91

5 Summary 93

6 Outlook 97
6.1 Online damage monitoring and advanced beam monitoring . . 97
6.2 Position measurement with confocal microscopy 98
6.3 Single frame high dynamic range (HDR) imaging 101

A Non laser damages on optics in vacuum 103

Danksagung 122

List of Figures

1.1 Historical intensity evolution 3
1.2 Schematic overview of a laser plasma experiment 4

2.1 Principle of CPA 11
2.2 Schematic setup of ATLAS300. 12
2.3 Overview of the ATLAS300 13
2.4 Temporal contrast of ATLAS300 13
2.5 Concept of laser beam delivery in CALA 14
2.6 Typcial laser ion acceleration experiment 16
2.7 Carbon and gold targets for laser ion acceleration 18
2.8 DLC on target holder 19
2.9 Plastic target 20
2.10 Thickness measurement of DLC 21
2.11 Target wheel 23

3.1 Pulse length dependence of LiDT 27
3.2 Comparison of the band structure 28
3.3 MPI and tunneling ionization 31
3.4 Free carrier and impact ionization 32
3.5 Electron vs ion temperature 34
3.6 Theoretical vs experimental LiDT 37
3.7 Laser damage threshold setup 38
3.8 View into the measurement chamber of LiDT setup 38
3.9 Comparison of scatter signal and online microscope detection . 40
3.10 Residual gas analysis of the measurement chamber 41
3.11 Photodiode voltage vs laser pulse energy 43
3.12 Fluence map compared to ablated area of substrate 44
3.13 Beam normal vs on substrate fluence 45
3.14 LiDT diagram 46
3.15 Laser damage threshold of commonly used optics 47
3.16 Laser damage thresholds of applied CALA mirrors 48

3.17 Influence of vacuum on LiDT 49
3.18 Typical setup of a grating type pulse compressor 51
3.19 LiDT diagrams of CALA pulse compression gratings 52
3.20 Surface contamination of grating 53
3.21 Bright field vs WLI images of damaged spots 54

4.1 RGA analysis of Ueye camera 59
4.2 Temperature dependent noise 61
4.3 Heatmap of camera during operation 62
4.4 Temperature vs cooling bodies 62
4.5 Camera with cooling body 63
4.6 Emp safe camera housing 64
4.7 Transmitted laser light during laser plasma interaction 65
4.8 Vacuum microscope setup 68
4.9 High and low magnification comparison 69
4.10 Michelson interferometer 71
4.11 Intensity vs displacement in WLI 72
4.12 Interference spectrum 73
4.13 WLI distance measurement 75
4.14 Vacuum WLI microscope setup 76
4.15 Brightfield vs WLI microscopy: Thin foils 77
4.16 Brightfield vs WLI microscopy: Broken targets 78
4.17 3D topography measured with WLI 79
4.18 Spectral reflectivity of thin films 81
4.19 Spectral reflectivity 280 nm formvar 81
4.20 Comparison of thickness measurements 82
4.21 Shack hartmann sensor 84
4.22 Feedbackloop adaptive mirror and wavefront sensor 85
4.23 Microscope setup with wavefront sensor 86
4.24 Theoretical focal spot versus measured spot 89
4.25 Intensity lineout of theoretical and experimental focal spot . . 90
4.26 3D model of the final microscope 92

5.1 Table of Laser damage thresholds of mirrors 94
5.2 Microscope in CALA 95

6.1 Scattered light on damage spot 98
6.2 Optomechanics of a LBD mirror in CALA 99
6.3 Principle of confocal microscopy 99
6.4 Confocal distance measurement 100
6.5 HDR imaging with a 2D grating 102

A.1 Non laser related damage of optic in vacuum 104

Zusammenfassung

Technologische Entwicklungen auf dem Gebiet der Laserionenbeschleunigung haben in den letzten Jahren eine große Bedeutung erlangt und unterstützen die Entwicklung der Anwendung der herausragenden Eigenschaften von lasergenerierten Teilchen. In dieser Arbeit zeigen wir Messungen und Entwicklungen, welche den Aufbau des 3 PW Lasersystems **A**danced **T**itanium-Sapphire **LAS**er (ATLAS3000) im **C**entre for **A**dvanced **L**aser **A**pplications (CALA) und das Laserionenbeschleunigungs-Experiment darin unterstützen und ermöglichten. Durch Messungen der Laserzerstörschwelle von Testspiegelsubstraten für die **L**aser **B**eam **D**elivery (LBD) konnte gezeigt werden, dass die Zerstörschwelle von Spiegeln, die für Hochintensitätslaser optimiert wurde großen Schwankungen unterliegen. Ferner konnten durch die Messungen die momentane technische Machbarkeit von Optik-Herstellern weltweit für große Spiegel die mit dem ATLAS3000 Laserstrahl kompatibel sind gezeigt werden. Messungen an Gittersubstraten zur Laserstrahlkompression im ATLAS3000 veranschaulichten die Fragilität dieser Komponenten. Nur wenige Unternehmen sind in der Lage, Gitter in gewünschter Qualität und Größe herzustellen. Ferner konnte gezeigt werden, dass mögliche Anreicherungen einer Kontaminationsschicht während einer Beleuchtung mit Hochleistungslaserimpulsen möglich sind, welche bei der Auswahl der Substrate berücksichtigt werden müssen. In dieser Arbeit haben wir Laserzerstörschwellen von Pulskompressionsgittern gemessen und große Abweichungen bei Gittern desselben Unternehmens festgestellt, wobei der Unterschied nur bei geringen Änderungen der Produktionsparameter lag. Dies zeigt, wie wichtig sorgfältige Messungen der Laserzerstörschwellen für Hochleistungslasersysteme sind.
Für die Laser-Ionen-Beschleunigung wurde mit einem fortschrittlichen Vakuummikroskop ein Analysewerkzeug für eine Untersuchung der Laserwellenfront, als auch umfassende Target Analysemöglichkeiten und Positionierungen im Vakuum mit der Erweiterungsmöglichkeit für Automatisierung, vorgestellt. Durch Modifikationen von wissenschaftlichen Kameras für Benutzung im Vakuum und unter rauen Strahlungsbedingungen konnte die Entwicklung

des Vakuummikroskops ermöglicht werden. Dieses Mikroskop löste die bis dahin üblichen Vakuum-Luft Hybridlösungen ab. Mit dem kompakten Design wurden weitere Diagnosemöglichkeiten verfügbar, wie zum Beispiel eine Online-Schichtdickenmessung von transparenten Filmen im Dickenbereich von 50-2000 nm und eine absolute Target Versatzmessung mittels in Vakuum Weißlichtinterferometrie. Ferner kann durch die Weißlichtinterferometrie eine Qualitätskontrolle von konventionellen flachen Targets, als auch komplexen geformten Targets im Vakuum kurz vor der Laserbestrahlung gewährleistet werden.

Abstract

Technological developments in the field of laser ion acceleration have become of major importance in the last years and are supporting the development of application of the outstanding characteristics of laser generated particles. In this thesis we demonstrate measurements and developments, which enabled and supported the installation of the 3 PW **A**dvanced **T**itanium-Sapphire **LAS**er (ATLAS3000) in the **C**entre for **A**dvanced **L**aser **A**pplications (CALA) and the laser ion experiment therein. Measurements of the laser damage threshold of mirror substrates showed a large fluctuation of damage threshold and demonstrated the state of the art production capabilities of optic supplier for full scale mirrors for the CALA **L**aser **B**eam **D**elivery (LBD) worldwide. Measurements on grating substrates for laser beam compression in the ATLAS3000 laser visualized the fragility of these components. Besides the fact that only few companies are able to produce gratings in demanded quality and size, also contamination accumulation via illumination of high power laser pulses needed to be taken into account, when consideration of the substrates are made. In this thesis we measured laser damage thresholds of pulse compression gratings and found large deviations at gratings of the same company with only slight modifications of the production parameters. This illustrates the importance of careful measurements of laser damage thresholds for high power laser systems.
For laser ion acceleration, an advanced diagnostic tool for laser wavefront diagnostic, as well as online in vacuum target diagnostic and position measurement with possibility of automization is demonstrated. Modifications of scientific cameras for vacuum and under harsh radiation environment lead to a development of a vacuum immersed microscope for laser and target diagnostic. This microscope superseded the semi vacuum solutions, which were state of the art until then. With the compact design, more diagnostic capabilities became available, which enabled an online target thickness measurement of transparent film of the thickness range of 50-2000 nm and an absolute target displacement measurement as well as surface topological analysis of targets via in-vacuum white light interference microscopy, which

opened the possibility of automized target quality inspections and analysis of complex topographies of shaped targets for laser ion acceleration.

Chapter 1

Introduction

1.1 Scientific context

The first laser accelerated ions in the 100 eV kinetic energy range were generated already shortly after the invention of the laser in the 1960s [58]. Their kinetic energy scaled with the laser energy/intensity. With disrupting new technologies in laser pulse generation and intensities rising to a critical level[1], ions in the MeV/nucleon range became accessible starting in the early 2000s [91, 33, 108]. Since then, the maximum laser intensity achieved in the laboratories worldwide has almost stagnated, and so did the maximum kinetic energies. Many efforts have aimed to optimize the laser-target interaction with the goal to optimize the particle beam for potential applications. Motivations range from cheap and compact proton sources for radiographic cancer therapy [4, 98], to injection sources for conventional accelerators [49] and many more. Laser ion acceleration is still a young and explorative field, however it finds itself at the transition from proof of concept experiments to first applications using the generated ions rather than just exploring how to produce them. The **C**enter for **A**dvanced **L**ight and **A**pplication (CALA) facility, which is in the final construction phase during the time of this thesis (2018) is an example of a facility specifically aimed at the advancement of the application of laser-driven particle beams. While there are still obstacles to overcome in source generation, the laser ion acceleration has come to a point, where technological developments play a key role and can decide on successful operation.
In this thesis we will take a journey from generating high intensity laser pulses, via transporting them in a vacuum system to the experiment and delivering them in a well characterized focus to a similarly well defined target.

[1] So called relativistic intensity

Our journey starts with the damage threshold of optical components, which is of vital knowledge since we need to make sure the laser pulse actually reaches the experiment. We continue with the detailed diagnostics of the laser pulse and the target in the interaction region, as their combination serves as the input for analytical or numerical models of the laser-plasma experiment and dictates its outcome. Developments and experiments presented herein were performed with ATLAS300 at **L**aboratory for **EX**treme (LEX) photonics, the predecessor lab of ATLAS3000 at CALA, operational in 2015-2016.

1.1.1 Short laser pulses and high intensity

In 1960 the laser was invented by Maiman [58] and also this was the first time, since generated light reached unprecedentedly high intensities. Kilowatts of peak power were now concentrated on less than a square centimeter and could be focused even further. This was also the time, since first light induced damages on optical surfaces with artificially generated light were observed. Scientists, who were building lasers, were advised to keep spare laser rods, in case the coating on the rods were damaged [82], a common practice even in todays lasers. A few years later Q-switching was invented [59], which reduced the pulse length from initially milliseconds (pump time of the flash lamps) down to nanoseconds. With this method the peak power and the intensity could be increased by several orders of magnitude. Laser matter interactions became increasingly interesting. With the achievable intensities nonlinear effects in matter could be triggered more easily (for example optical second harmonic generation [64]) and even the ionization threshold of matter could be reached. By the invention of mode locking ultrashort pulses could be generated and the peak intensity rose even higher. However, there was a natural limit to the intensity, because of non-linear effects in air and other transparent materials. Filamentation of laser beams could cause damages in laser crystals and also limit the beam propagation in air. In 1985 CPA[2] [95] was first demonstrated for optical lasers and the intensity limit could be circumvented. By stretching the laser pulse in time, the intensity could be drastically reduced, which allowed further amplification. The laser pulse is compressed in time after the final amplification stage, which made unreachable intensities accessible. The current published intensity record lies at $2 \cdot 10^{22} \frac{\mathrm{W}}{\mathrm{cm}^2}$ at the Hercules laser in Michigan USA [111] and has not been topped by almost a decade. Presently, several laser facilities, that will be aiming for new records, are under construction around the globe. In figure 1.1 a historical overview of the highest generated intensity can be seen. Notably

[2] **C**hirped **P**ulse **A**mplification

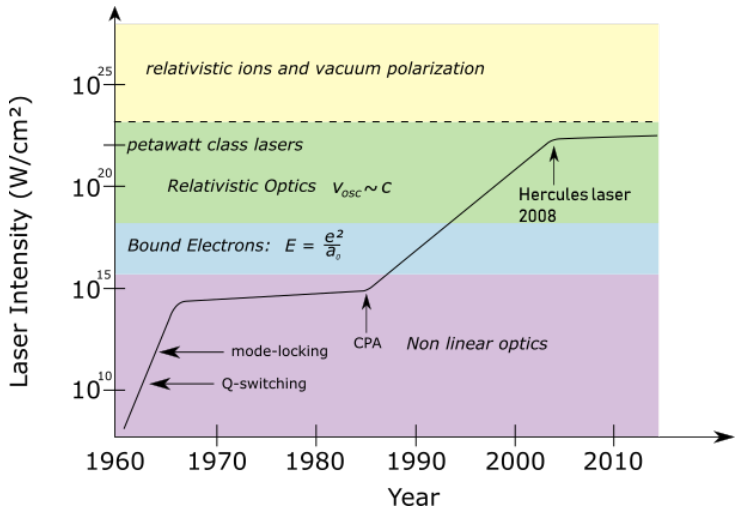

Figure 1.1: Intensity evolution over time. After the invention of the laser in 1960 intensity grew fast until mid of 1960s. Non linear effects and laser induced damage threshold inhibited a further increase until the invention of CPA in 1985. Since the intensity record in 2008 the increase has stagnated. This mirrors the technological limits of optics and laser gain media. Picture adapted from [107].

is the stagnation of the peak intensity from 2008 until present day, which can be attributed to laser damage threshold and connected manufacturing capabilities and limits.

1.1.2 Laser Ion Acceleration

With intensities exceeding $1.37{\cdot}10^{18}\frac{\mathrm{W}}{\mathrm{cm}^2}$ so called relativistic effects take place. At this intensity, electrons get accelerated to relativistic velocities within a few laser cycles. In addition, the $\vec{v} \times \vec{B}$ term in the Lorentz-force becomes dominant and pushes the electrons in the direction of the laser beam. This effect allows, depending on the target and laser parameters, to generate multiple kinds of radiation. As in this thesis the technological developments are inspired by laser ion acceleration experiments. We will thus give a coarse overview of the mechanisms for generating high energy ions via intense lasers. However, a detailed description is beyond the scope of this thesis and the interested reader is referred to the review papers [14, 57, 56] and references therein.
Multi MeV ion bunches accelerated from thin foils illuminated by a high power laser pulse were firstly observed in 2000 [91, 33, 108] and has since then boosted the research in laser plasma interaction and acceleration as

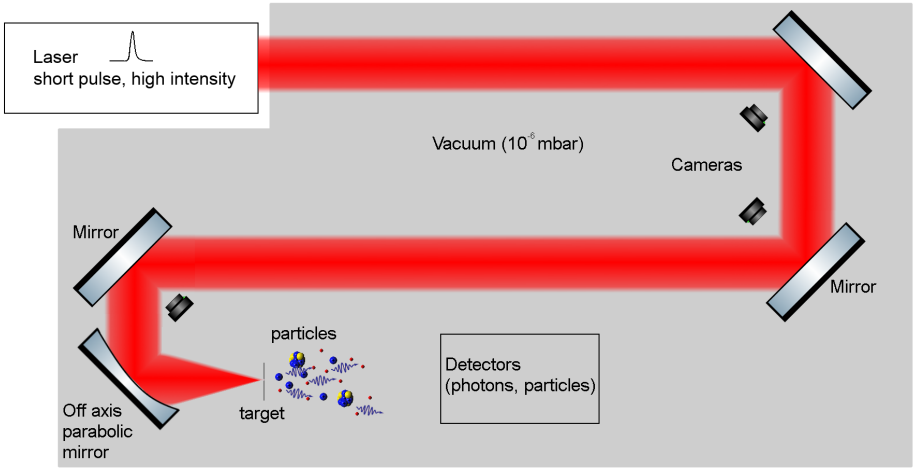

Figure 1.2: Schematic overview of a typical laser plasma experiment with laser infrastructure. The laser pulse is generated and transported with a mirror system in vacuum to the experiment where this laser pulse is focused on a target. Diagnostics analyze the generated particles

well as the development of high power laser systems worldwide. Of great interest were the investigation of the acceleration mechanisms, which were able to generate multi MeV ion beams on acceleration lengths as short as a few µm.
This accelerated particles offered remarkable properties, which made them interesting compared to conventionally generated ion bunches. For example laser accelerated ions have a large number of particles per bunch [3] and can offer very short pulse length (down to picoseconds). These and several other characteristics make laser accelerated particles ideal candidates for interesting physics, like for example fission fusion experiments [32] or medical applications [4, 98].
In laser ion acceleration experiments a high power laser beam (terawatt up to petawatt) is focused on a thin (tens of µm down to few nm) target. Non linear laser plasma interactions generate high energetic ions (protons and other heavier ions). A schematic sketch of such an experiment can be seen in figure 1.2.
In the following we highlight the two most referred acceleration mechanisms: Target normal sheath acceleration and radiation pressure acceleration.

[3] Typical total proton numbers achieved in laser ion acceleration experiments range from 10^{12} to 10^{13}, while having a broad energy spectrum 10^{6}–10^{8}/(msr× 1%Ekin)[51]

Target Normal Sheath Acceleration (TNSA)

TNSA is based on the efficient generation of fast electrons by laser target interaction. The rising edge of the laser intensity creates electric fields, high enough to ionize matter. Laser interaction is mainly restricted to the plasma created on the laser facing target side (front side). By heating of this plasma surface, hot electrons are generated, which travel through the target if the thickness is below a few tens of µm. The fast electrons reach the rear side of the target producing a sheath region. In the sheath region, a space-charge electric field is generated by the ions, which prevents the fast electrons from escaping. This large electric field ionizes atoms lying on the rear surface, creating ions. In metallic targets, protons are ordinarily present as surface impurities and are thus located near the peak of the sheath field. Ions are now accelerated in this high electric field to multiple MeV kinetic energy per nucleon. The current record lies at 85 MeV (protons) [104].

Radiation Pressure Acceleration (RPA)

When an electromagnetic wave of intensity I_L shines on a plane surface (e.g. a target) momentum is transferred, which results in a pressure [50, 56]:

$$P_{rad} = (1 + R - T)\frac{I_L}{c} = (2R + A)\frac{I_L}{c}$$

R,T and A are the reflection, transmission and absorption of the surface, with the energy conservation $R+T = 1-A$. For an overdense plasma $R = 1$ and momentum is transferred to the electrons in the plasma. This sheet of accelerated electrons travels into the target plasma and ramps up the electron density. Depending on the target thickness, the sheet can escape the rear surface (Light Sail [77]) or bores a hole into the target (Hole Boring [72]). By the creation of the electric field with the ion, the ions are 'pulled' by the electron sheet and co-propagating. The spread of kinetic energies of the ions accelerated with this mechanism can be very small and the maximum reachable energy depends on $(I \cdot t)^2$ in the non relativistic phase.
While TNSA relies on efficient heating of the electrons, which can be improved by a plasma gradient on the front surface due to pre-expansion of the target, RPA relies on a perfect overdense plasma and suppressed heating of the electrons. Thus the demands on the laser temporal intensity profile can be very different for the two mechanisms. Also the target requirements are quite different. For TNSA targets in the range of several 100s of nm to 10s of µm have proven to be most efficient, while the RPA mechanism relies on ultrathin targets (few nm to 10s of nm) for currently accessible laser intensities.

1.1.3 Technological challenges

Generating high power laser pulses is a challenging task. Around 20 years ago the first petawatt scale laser (NOVA laser [73]) has been successfully operated. Since then, laser systems worldwide have been established, however the rise in achieved intensity has slowed down (compare figure 1.1). The reason for this are technical limitations, for example dictated by the laser induced damage threshold. With rising laser power, higher demands on optics and laser gain media are imposed, which scales the effort and price nonlinearly. Petawatt class laser systems back then were based on Neodymium doped glasses as gain media, which was the material of choice, because it could be produced in sufficient size and pumped by Xenon flash lamps. However the thermal conductivity is small and combined with the broad pump light spectrum of the flash lamp, which creates a large amount of excess heat, the pulse repetition rate was limited, in order to let the gain media cool down between shots. For example the Texas Petawatt laser has a repetition rate of 1 shot every 40 minutes [29]. Modern laser systems with focus on application demand a much higher repetition rate and are mostly based on Titanium doped sapphire crystals (Ti:Sa). This gain media offers a vastly increased thermal conductivity, which allows operation of PW scale laser systems at sub Hz to several Hz rates [113, 44]. In addition Ti:Sa systems offer an increased optical bandwidth, which eventually allows a generation of shorter pulse length. While the shortest pulse length in glass laser systems was about 150 fs (Texas Petawatt [29]) pulse lengths of Ti:Sa lasers can achieve 20 fs and shorter laser pulses. However besides all this benefits compared to glass laser systems, Ti:Sa crystals are very difficult to produce in large scale and quality [42].

Not only laser crystals limit the peak power and energy, but also the damage threshold of optics in the laser system and transport system to the experiments. Ultra intense laser pulse experiments solely take place in vacuum which adds another challenge for optics to sustain the high intensities. Mirrors of large size, high quality and high laser damage threshold must be used for such experiments, which only recent development made possible. In this thesis we investigated the capabilities of companies to produce mirrors of the size to support a 280 mm beam in terms of laser damage threshold. Only few companies worldwide are able to produce such mirrors in sufficient quality and demanded damage threshold. CALA laser beam delivery will be equipped with mirrors of size hitherto not routinely used in any Ti:Sa laser system so far. Also the fluence on optics at ATLAS3000 will be higher than any other Ti:Sa laser system, pushing the limits and demands of the optics.

In this thesis we tested the laser damage threshold of samples of the applied companies for producing such mirrors and ensured that they can sustain the high fluences we anticipate.

Final challenges lie in the generation of the ultra high intensities by focusing the transported laser pulse with high precision optics[4] to diffraction limited spot sizes. Only detailed knowledge of the spatial intensity profile of such focused laser spots makes it possible to calculate the reached intensity. In case of laser ion acceleration, also precise position and measurement of the illuminated target is crucial. In this thesis we developed a fully vacuum compatible microscope, removing the cumbersomeness of semi vacuum solutions, which were standard up to then. The in-vacuum solution offers highly improved compactness. While beneficial to the rising space limitations, the compact setup allowed introduction of hitherto unaccessible features like absolute distance measurements, which can lead to high repetition rate target positioning and optical thickness determination of transparent targets in vacuum. An inclusion of a Shack-Hartmann sensor for wavefront sensing rounded up the all in one in vacuum target and laser analysis tool. The wavefront sensing in this microscope will serve as an input for a deformable mirror placed in the laser beam delivery in CALA, which will ensure diffraction limited focusing, resulting in the highest possible intensities.

1.2 Thesis outline

The aim of this thesis is to improve and provide reliable tools for laser plasma experiments. Starting from beam transport in vacuum until detection and characterization of laser pulses and targets at the experiment.

Chapter 2 describes a general overview over PW-class lasers and the infrastructure for such experiments. Generating high intensity laser pulses, guiding them to the experiment as well as target production and characterization for such experiments.

Chapter 3 describes laser damage threshold measurements of mirrors and other optics for PW class lasers. Damage threshold has been one of the aspects for choosing which pulse gratings for laser pulse compression and which mirrors for the laser beam delivery to the experiments in CALA were chosen.

Chapter 4 describes a development of a vacuum compatible microscope

[4]For example with off axis parabolic mirrors

for laser plasma experiments. Modification of cameras for vacuum compatibility paved the way for a full vacuum immersed diagnostic system for laser pulse and target characterization, as well as various optical observations in laser plasma experiments.

Chapter 5 summarizes the results and

Chapter 6 discusses future aspects of the presented technologies.

Chapter 2

PW lasers: Infrastructure

2.1 Laser infrastructure

In this section we will talk about the infrastructure around a pw- class laser system. As an example we will take the ATLAS300 in LEX photonics, where in the time from 2014 to 2016 experiments were performed. ATLAS300 was designed as a precursor of the ATLAS3000 in CALA and will serve as the frontend for the final amplifier. Among laser plasma experiments with this laser to test the developed tools, also prototype development for the CALA infrastructure was done and tested. One example is the development of motorized, vacuum compatible mirror holders for large rectangular mirrors suitable for the LBD in CALA (300 mm x 420 mm x 80 mm), as well as laser beamline developments and infrastructure at the experiments as well.

2.1.1 Generation of intense ultra short laser pulses

Based on the introduction of the generation of ultra short pulses we will here go into more detail considering the example of ATLAS300 in LEX-photonics. We will describe the laser and the future upgrade to ATLAS3000. ATLAS stands for **A**dvances **T**itanium Sapphire **LA**ser **S**ystem and is, as the name suggests, a Ti:Sa Laser system capable of producing laser pulses with 6 J energy and 20 fs pulse length, resulting in a peak power of more than 300 TW. An schematic overview of the optical setup is presented in figure 2.2

ATLAS300 is a chirped pulse amplification (CPA) [95] laser system. In CPA, a low intensity short laser pulse is stretched in time and amplified. By this technique the intensity on the optics during pulse generation and amplification is reduced, which is beneficial for laser damage threshold and unwanted nonlinear effects, due to high intensity. After final amplification the laser

pulse is compressed again and delivered to the experiments. A schematic overview of this process is shown in figure 2.1. At ATLAS300 the initial laser pulse is generated via a commercial Ti:Sa laser oscillator[1], which delivers 20 fs pulses at a repetition rate of 70 MHz with individual pulse energy of 7 nJ. The repetition rate is reduced with a pockels cell to 5 Hz and the pulses are amplified in a high gain booster amplifier to 4 mJ. This pulse is now stretched in time to about 300 ps in a grating stretcher, resulting in pulses with 100 µJ energy and pulse length of 300 ps. Following the principle of CPA, all further amplifications are carried out at this pulse length. The next amplification stage is a regenerative amplifier, which increases the pulse energy from 100 µJ to 4 mJ. A regenerative amplifier is a cavity, where the number of round trips can be adjusted. By the use of 2 pockels cells, pulses can be injected into the cavity and extracted after the desired number of passes. With each pass, an amplification of the pulse energy is achieved, and thus with this amplifier, a large gain can be accomplished. The pulse with now 4 mJ energy is amplified by a series of multipass power amplifier. In 3 different stages the laser pulse is amplified from 4 to 15 mJ, from 15 to 550 mJ and 550 mJ to 1.8 J. Between each of the multipass stages, spatial filter are implemented to retain beam quality. The final amplification stage is a multipass amplifier with a cryogenic cooled Ti:Sa-crystal. The crystal is cooled to 150 K to increase the heat conductivity in order to reduce the thermal lensing. In this stage the laser pulse is amplified from 1.8 J to a maximum of 10 J. The beam is increased in size to its final diameter (100 mm) and the wavefront is optimized with an adaptive mirror. In the vacuum pulse compressor the stretched pulse is compressed to the final pulse length of 20 fs and final energy of 6 J resulting in 300 TW optical power. The vacuum laser beam delivery guides the laser pulses to the experiments.
ATLAS3000 will be an upgrade of ATLAS300 and is build up during the time of this thesis (2018). ATLAS300 pulses will then be further amplified by two power amplifiers. The first stage increases the pulse energy from 1.5 J to 40 J and in the second stage the pulse is amplified to the final 90 J pulse energy. After compression the energy will be at 60 J in 20 fs, which results in a optical peak power of 3 PW. The beam diameter will be 280 mm resulting in a average fluence of 100 $\frac{\mathrm{mJ}}{\mathrm{cm}^2}$ and an intensity of $5{\cdot}10^{12}\,\frac{\mathrm{W}}{\mathrm{cm}^2}$ on a 0° mirror surface.

[1] Femtosource Rainbow

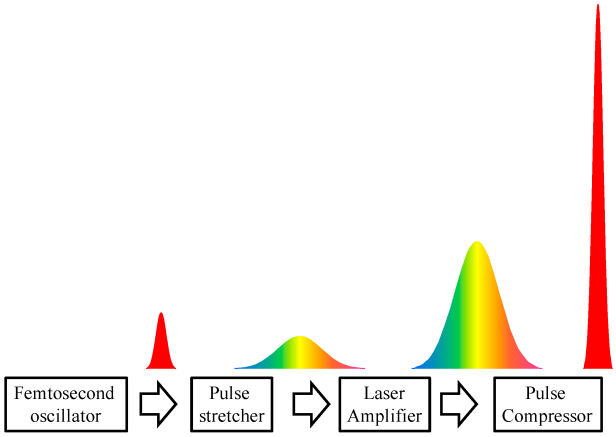

Figure 2.1: Principle of CPA taken from [65]

2.1.2 Temporal laser contrast

While most of the pulse energy of a femtosecond laser is concentrated in the short time of the main pulse of a few 10s of femtoseconds, a small, but non negligible part of the pulse energy is distributed in time around the maximum. The ratio between main pulse intensity and background intensity is called contrast.
During laser pulse generation and amplification several effects like amplified spontaneous emission (ASE) and prepulse generation can generate unwanted background signal and limit the laser contrast. With fast pockels cells the ASE time can be minimized in time to the length of the stretched pulse. To measure the temporal contrast a commercial third order autocorrelator[2] is used [53]. With a third order autocorrelator a prepulse can be distinguished from a post pulse. In figure 2.4 an example of the ATLAS300 contrast is given. The intensity is normalized to the peak intensity. Starting from 400 ps before the main pulse, the constant ASE level of 10^{-10} can be seen. Prepulses can be seen at -170, -150 and -90 ps. Prepulses in a laser system can have various origins. They can originate from reflections of optic surfaces and also postpulses can be converted to prepulses via nonlinear effects in the amplification process [18]. The noise level of the autocorrelator is indicated as 10^{-13} at -190 ps, where the beam was blocked.
For relativistic laser plasma experiments in general and laser ion acceleration in particular, the temporal laser contrast is of major importance. The peak intensity of such a laser pulse is many orders of magnitude higher than the ionization threshold of matter ($10^{12-13}\frac{\mathrm{W}}{\mathrm{cm}^2}$). Highest contrast is thus very

[2] Amplitude Sequoia

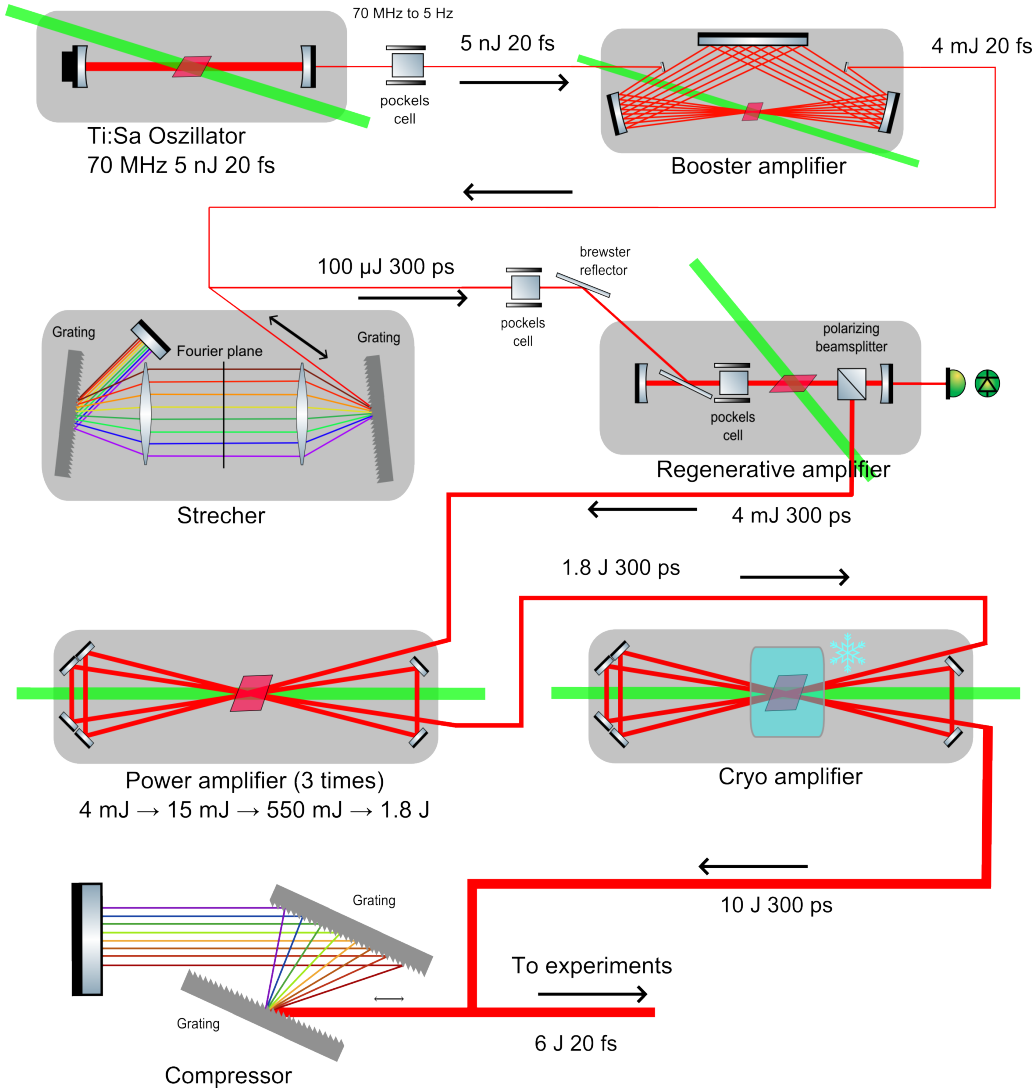

Figure 2.2: Schematic setup of ATLAS300.

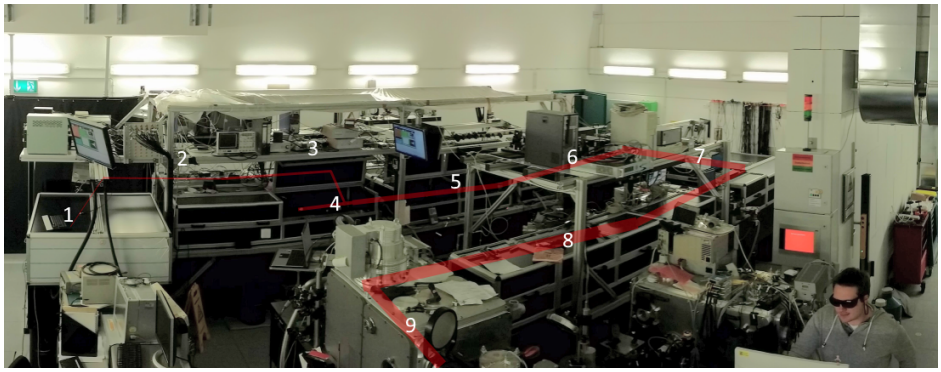

Figure 2.3: Overview of the ATLAS300 with indicated beam path and laser damage threshold setup. This different stages are as following: 1 Oszillator and booster amplifier, 2 stretcher, 3 regen and Multipass amplifier, 4,5 and 6 multipass amplifier, 7 cryo cooled amplifier, 8 adaptive mirror and 9 pulse compressor

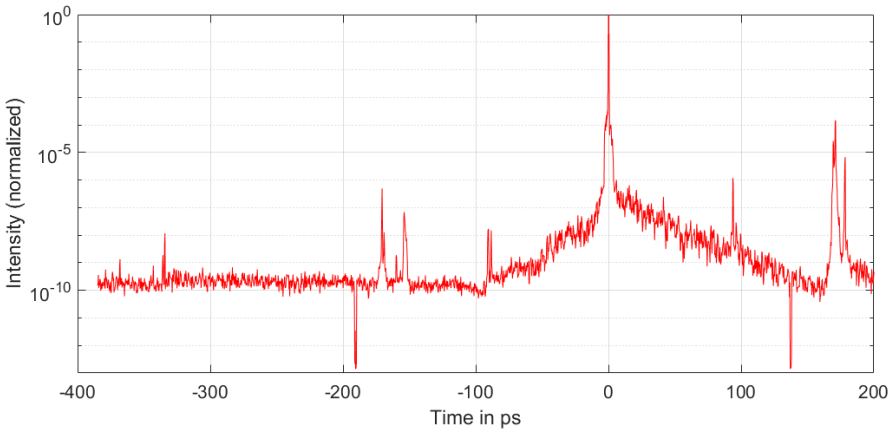

Figure 2.4: Temporal contrast of ATLAS300 recorded with a 3rd order autocorrelator

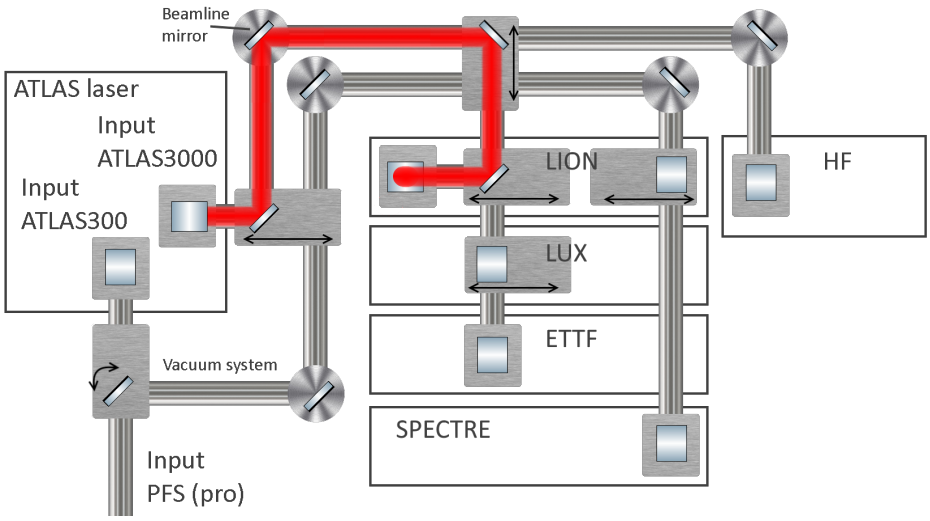

Figure 2.5: Concept of laser beam delivery in CALA

important for laser ion acceleration, as ionization of a target before the main pulse leads to expansion of the target, which can lead to unwanted plasma gradients or even undercritical plasma density at mainpulse interaction. Thus it is advisable to keep the intensity before the main pulse below the ionization threshold. This however is challenging and in order to improve the laser contrast only few techniques are available, some of which can improve the contrast during the pulse generation like a technique called XPW [43] or after, by a fast optical switch via a laser plasma mirror [19, 20].

2.1.3 Laser beam delivery

CALA will house 5 experiments of which 4 use the ATLAS3000 (**L**aser **Ion** Acceleration (LION), **L**aser-driven **U**ndulator **X**-ray Source (LUX), **E**lectron and **T**homson **T**est **F**acility (ETTF) and **H**igh **F**ield Physics (HF)). Thus, this laser needs to be transported to the different experiments. A complex vacuum tube system hosting the laser beam delivery was designed for this purpose. The system consist of 14 turning mirrors, which reflect and steer the beam into the experiments. The longest transport of the beam will be at around 50 m. Cameras imaging the surface of the mirrors are used for alignment and to make sure the beam will stay in the center of the mirrors. A sketch of the concept of the beamline is given in figure 2.5. With a diameter of 280 mm there will be an averaged fluence of $100\frac{\mathrm{mJ}}{\mathrm{cm}^2}$ in the normal beam. The averaged fluence on the beamline mirrors will be $\approx 70\frac{\mathrm{mJ}}{\mathrm{cm}^2}$ due to 45 degree incidence angle.

2.2 Experimental infrastructure

Laser ion acceleration is dependent on high intensities. Thus the high power laser pulse (TW to PW) is focused by a low F-number focusing optic to a small, diffraction limited focal spot to generate relativistic intensities ($I > 10^{18} \frac{\mathrm{W}}{\mathrm{cm}^2}$). To avoid nonlinear effects in high intensity experiments, transport and diffraction of the laser pulse is solely done with reflective optics. Thus the focusing optic is usually an off axis parabolic mirror (OAP). In figure 2.6 a typical laser ion acceleration experiment is shown at concept of the High Field Physics experiment in CALA. The individual components are marked with numbers. The laser in this example is focused by a OAP (1) with focal length of 560 mm. The focal spot is targeted at a thin foil or other topologies like levitated microspheres [70] of the material of choice, which is commonly called target. A description of common target production techniques and characterization is described in the following sections. Excellent overlap of the focal spot and target surface needs to be ensured, as the Rayleigh length of a fast focusing optic is short (The Rayleigh length of the example in figure 2.6 is 16 µm). Proper overlap is ensured by a combination of an (automated) target delivery (2) and positioning system (3). At this example, the target delivery and positioning is realized via a combination of a target wheel with a vacuum compatible microscope for a high repetition rate (0.5 Hz) experiments. This tool has already been successfully tested in the laser ion experiment in LEX photonics [27]. More details about this tool can be found in the following sections. With the laser spot on the target, energetic particles can be generated. These particles (photons, electrons, protons and heavier ions) can be detected by various diagnostics. Electrons and protons/ions are usually analyzed by magnetic spectrometers (4 and 5) [87], whereas cameras can be used for transmitted laser light for optical opacity measurement of the target during interaction as well as spectrometers for higher photon energies [54].

2.2.1 Targets for laser ion acceleration

Laser ion acceleration relies on thin targets of various materials, ranging from several micrometer to down to 100 nm thick metal foils [86, 71] to nm thin plastic, diamond like carbon or other materials [112, 54, 5]. While µm thick targets are commercially available, freestanding nm thick targets are limited in availability and versatility. This motivated us to produce these targets in our own target fabrication lab.
Thickness is a crucial parameter, as the maximum ion energies increase on the one hand with increasing intensity, but on the other hand there is an

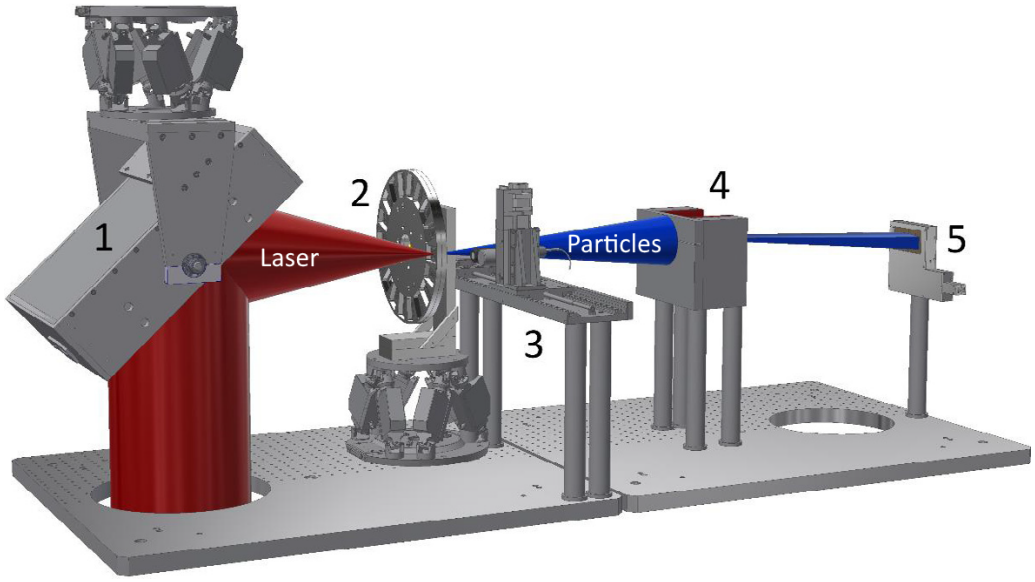

Figure 2.6: Typical laser ion acceleration experiment at the example of the high fields (HF) experiment in CALA. The components are market with numbers:
1. Focusing optic, typically an off axis parabolic mirror
2. Target, in this case a target wheel for fast target delivery and positioning
3. Target and laser diagnostic, in this case a vacuum microscope
4. Particle spectrometer, here a magnetic dipole
5. Particle detector, in this case an online ion detector (RadEye [79])
Image adapted from [52]

optimal target thickness for a given laser intensity and wavelength [14, 57]. A simplified model shows an optimal target thickness, if the electric field of the laser spot equals the electrostatic force of a fully charged target with a separation equal to the target thickness. However, depending on the laser contrast targets can be expanded prior to the main pulse interaction, which can affect the optimal thickness. Thus a high control and range of the target thickness is crucial.
The demands on targets for laser ion acceleration vary strongly with the intended goal of the experiment. For proof of concept studies with low shot number (<1000), high versatility and flexibility is demanded, which is typically achieved either with fast prototyping during experiment or pre-produced targets with dedicated properties. Production time is secondary and targets are optimized for the intended use. For high repetition rate experiments, like laser ion acceleration in CALA, where the focus lies on the application of the generated particles, production time is a crucial parameter. Such experiments can demand large number of targets (1000-10000) per day and will rely on a continuous support. The ability to mass produce, which demands well controlled production parameters and also low cost per single target renders these targets economically. In this section we demonstrate the production capabilities of thin film targets at LMU.
For all of the following described target production techniques, the transfer of the targets from substrate to the target holder is done via a technique called floating. Targets are produced on carrier substrates, which are covered with a water soluble separation layer (for example a thin layer of sodium chloride). These carrier substrates are carefully dipped into water at a shallow angle. The separation layer is dissolved by the water and the foil is floating on the water surface due to surface tension. For application onto the target holder, the target holder is immersed into the water and pulled out slowly when a target edge is touching the surface of the target holder. Due to the strong adhesion of the target to the metallic surface of the target holder, the target can be pulled out from the water surface and a freestanding foil is created over the holes in the target holder.

Thermal vacuum evaporated films

Thin metal films (i.e. gold films of a thickness ranging from 5 nm to 5 µm) can be produced via thermal evaporation of material in vacuum. Two techniques are available and commonly used at LMU: Resistive heating and electron beam heating. In resistive heating, a tantalum or tungsten container is clamped between two large copper electrodes. The resistance of the container is higher than the electrodes, thus if a low voltage is applied,

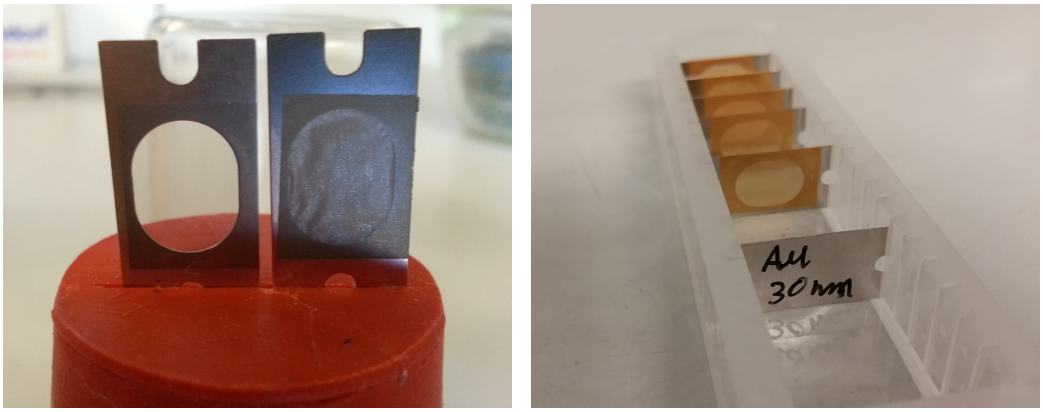

(a) Carbon foils (b) Gold foils

Figure 2.7: Targets produced with thermal vacuum evaporation. Left carbon foils 10 nm and 200 nm thick. Right gold targets 30 nm thick.

the container is heated and consequently evaporates the material placed in the container. Resistive heating is used for materials, which have a lower boiling point than the melting temperature of tantalum ($T_{melt} = 3290$ K) or tungsten ($T_{melt} = 3695$ K), for example gold ($T_{boil} = 3243$ K [114]) or sodium chloride (1732 K). For material with higher boiling point, electron gun heating is used. In this technique a high current electron beam of low energy is focused onto the material, which is placed in a cooled copper anode. By this technique the energy deposition focused to a small spot on the material. If the energy deposition is higher than the heat dissipation, the temperature of the material in the center of the electron beam rises until the boiling point is reached, while the surrounding material is cooled by the copper anode.
With those two techniques foils of basically every self supporting material can be made. Two examples of thin film targets are given in figure 2.7, which show gold and carbon films of various thicknesses. With this technique, per production run (3 h) 6 target holder can be covered with targets, resulting at $\approx$ 200 individual targets per hour. Targets are transferred to the target holder via the floating technique.

Diamond like carbon (DLC) films

Thin to ultra thin diamond like carbon foils (DLC) (3-100 nm) can be produced at LMU with a filtered cathodic vacuum arc technique [75, 55]. DLC is a carbon configuration with a high sp^3 content. In this technique, carbon ions are generated by a high current low voltage vacuum discharge between a metal anode and a carbon cathode. The high resistance of the carbon leads

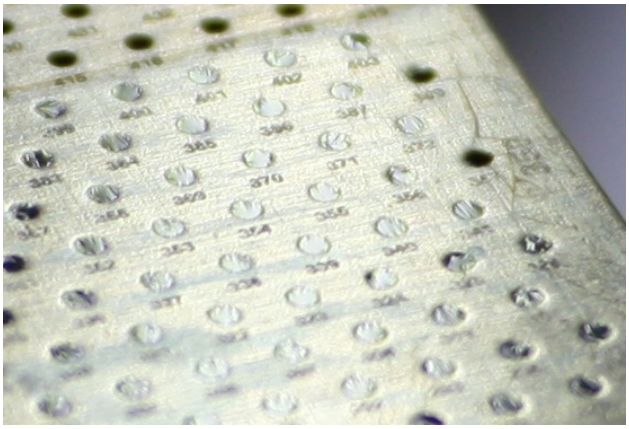

Figure 2.8: 10 nm DLC foil on a target holder. Hole diameter is 0.5 mm

to localized temperature rise, which causes local ablation and partial ionization. The generated carbon ions are accelerated by an acceleration voltage to about 80 eV energy. A magnetic duct filters neutral particles and guides the carbon ions to a biased substrate. The substrate bias and the ion energy result in a total impact energy of 100 eV, which favors the production of sp^3 bondings. This technique is interesting for production of ultra thin targets (> 20 nm) as DLC is a strong material suitable for self supporting thin films. In figure 2.8 a 10 nm DLC foil on a target holder can be seen. The foil is only visible to the eye at shallow angle light reflections. By comparing the covered holes on the target holder, damages in some foils can be seen. This demonstrates the fragility of such ultra thin targets. For thinner targets this effect is even more pronounced. The production speed is comparable with thermal vacuum evaporation techniques.

Plastic films

Thin plastic films can be produced via various methods. Among the available techniques are spin coating, dip coating, droplet method as well as chemical vapor depositions and many others. At LMU plastic films are made with spin coating and droplet method [88]. Spin coating is a technique, where a small amount of liquid is spread on a support via centrifugal force by fast rotation. Spin coating is a procedure used to deposit thin films to flat substrates. Usually a small amount of liquid is applied on the center of a substrate. The substrate is then rotated at high speed in order to spread the coating material by centrifugal force. By this means a thin liquid film is created. Depending on the vapor pressure the liquid now evaporates leaving behind the solved constituents. At LMU we used a combination of Dichloroethane

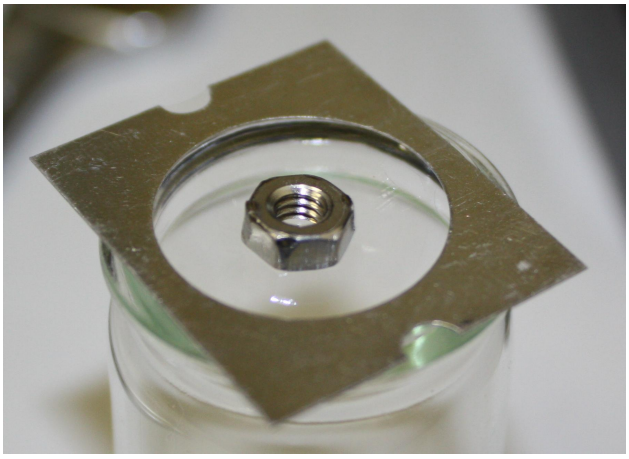

Figure 2.9: 40 nm thick formvar foil span on a target holder with free aperture of 20 mm. To demonstrate the stability a female screw is placed on the foil

with dissolved formvar. With this technique thin plastic films of thickness range 5-5000 nm can be produced. The typical coating area is 10 cm^2. Targets can be transfered from substrate to target holder via floating. For formvar and glass substrates, no parting agent is necessary, as the plastic foil can directly be released from the glass surface, if carefully dipped into water. In contrast to spin coating, the droplet method used a water surface as a substrate. In this method, a small amount of hydrophobic liquid is dropped on the water surface, which spreads out to a thin film. After evaporation of the solvent, the plastic forms a thin layer. Target transfer to the target holder is similar to the floating process, however no release from substrate is necessary, as the target is already floating on the water surface, which speeds up the production process.
Contrary to metal and DLC foils, formvar foils show high stability even at ultra thin film thicknesses. In figure 2.9 a formvar foil is span on a target holder with a free aperture of 20 mm. For stability demonstration, a female screw (m $\approx$ 600 mg) was placed onto the 40 nm thin foil center. This level of robustness drastically simplifies handling of ultra thin targets.

2.2.2 Target characterization

For laser ion acceleration, target thickness is the main parameter and depending on the production method, the target thickness can be measured by various methods. For thickness determination, high resolution profilers are

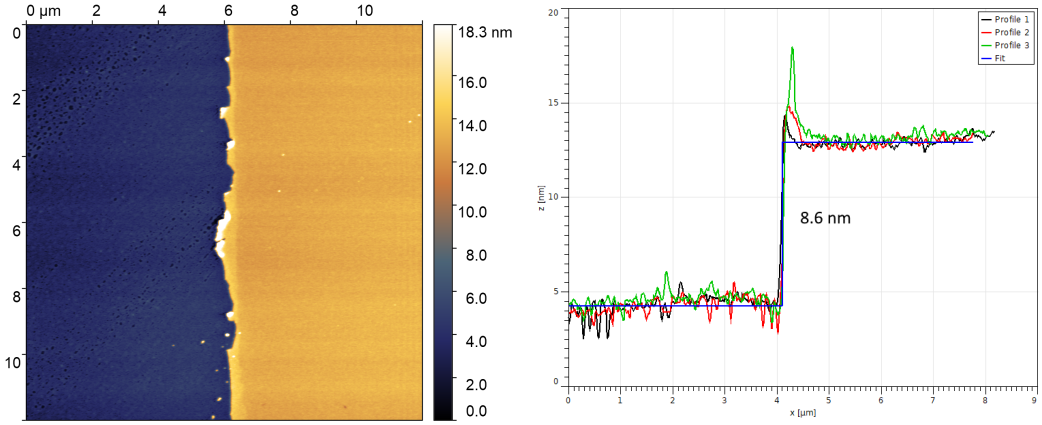

(a) Topography of DLC step

(b) Lineouts

Figure 2.10: Measurement of DLC step on a silicon substrate with AFM. Left shows the topography and right shows extracted profiles for thickness determination.

used. At LMU we have at hand an atomic force microscope (AFM[3]) and a whitelight interference- (WLI) and confocal microscope[4]. With the AFM a lateral range of 40 µm x 40 µm at a z resolution of 0.1 nm can be measured. The maximum range in z is limited to 1 µm. The measurement is rather slow, as a full resolution measurement takes about 40 min. Figure 2.10 shows an example of a AFM measurement of a DLC step on a silicon wafer.
With the whitelight interference microscope steps can be measured with an accuracy of 1 nm and a maximum range of ≈ 10 µm. While the resolution is lower compared to the AFM, the range is much increased, giving the possibility to measure thicker targets. Also the measurement speed is faster, as one measurement of the field of view takes about 3-5 min[5]. Confocal microscopy covers the same range as WLI, but is beneficial, if steep angles and complicated profiles (for example conically shaped targets) are measured.
The thickness of thin transparent films with known refractive index can also be measured via spectral reflectance measurement. This method is further described in section 4.6.4. This technique enables the direct measurement of freestanding transparent foils without the need of a step profile on a witness sample. The thickness range of spectral reflectometry is 50 nm to 20 µm.

[3]FRT
[4]Sensofar Plu neox
[5]The field of view is determined by the magnification of the microscope objective. The z resolution is not affected by the magnification

2.2.3 Comparison of the production techniques

With the presented production techniques a large variety of targets can be produced. While thermal vacuum evaporation offers access to most materials, the highest speed at which targets can be produced is given by plastic film production. Uniformity and reproducibility are the most challenging demands for target mass production. In reference [88] the uniformity of plastic films within 1 target holder is denoted with 10 % at a thickness of 100 nm. With improvements of the production techniques, this value can also be increased. Which production technique is most suitable for a specific laser system relies on several parameters. Depending on the laser contrast, it can be beneficial to use higher Z materials (i.e. gold), as the plasma preexpansion is suppressed for these materials. On the other hand, high proton content targets can be beneficial to increase the number of accelerated protons.

2.2.4 Target delivery and positioning system

For high repetition rate laser ion acceleration experiments, a target delivery and positioning system, which is capable of replacing targets in short time (few seconds or less) is mandatory. A prototype for target delivery and position system with a repetition rate of 0.5 Hz was constructed for the laser ion acceleration at LEX photonics [27]. Target delivery was realized in form of a target wheel, hosting 18 target holders, which in turn can support 99 targets. Thus the total amount of individual targets which can be stored in the target wheel is 1782. Core design of the target wheel is a massive aluminum disk with spare holes to support the target holder plates. This disk is machined with high precision and leaves a variation of 30 µm between two target holders. In figure 2.11 a model of the target wheel can be seen. Each target holder supports a thin film, which is spanned over the 99 holes in the holder. The target wheel offers high flexibility, as in principle 18 different target materials and or thicknesses can be used with one load.
The target positions are measured with a commercial chromatic confocal detector[6]. The accurate positioning is done with a hexapod. More details about this system can be found in reference [27]. The variation of the target height on each target holder lies within around 50 µm. This position variation is introduced when transferring the thin films onto the target holder, as the freestanding targets slightly lower into the holes during the floating process. The overall precision of the target plane between two targets thus lies within 80 µm. This error however is static and does not change, when the wheel is moved.

[6] micro epsilon

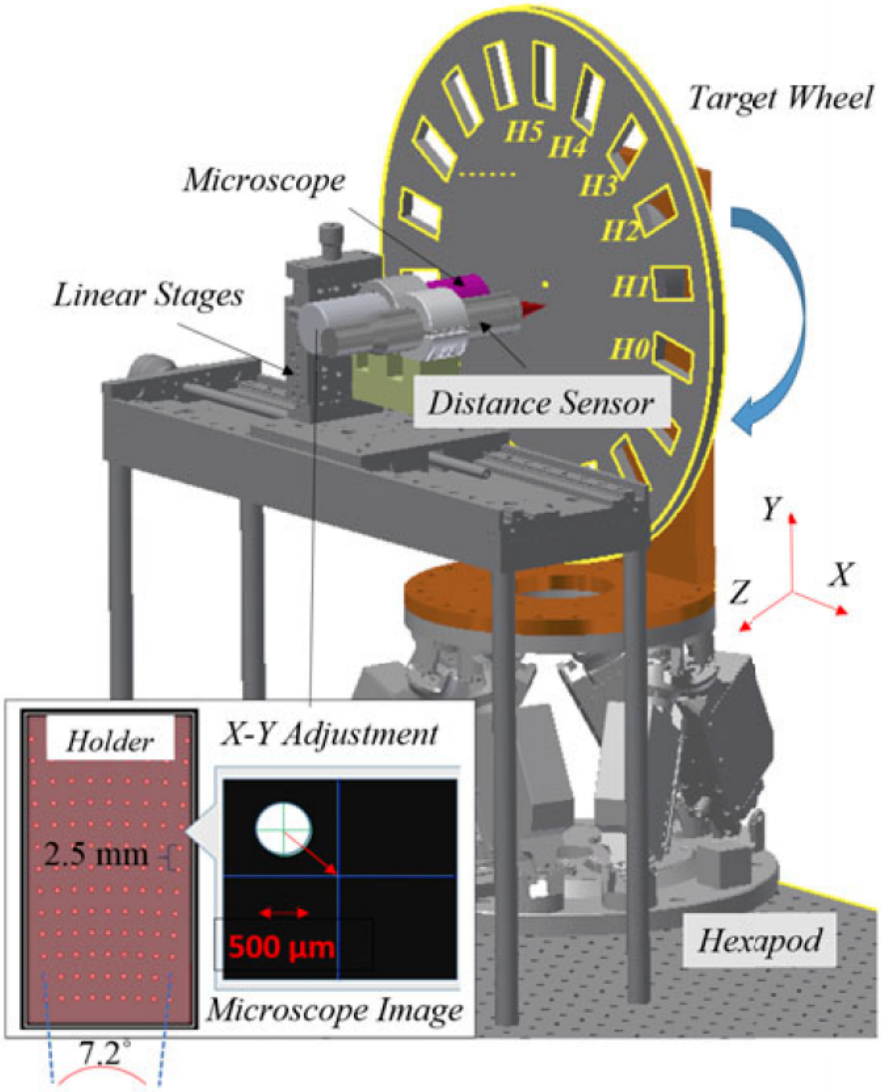

Figure 2.11: Target wheel for high repetition rate laser ion acceleration experiments. Picture taken from [27]

2.3 Summary and conclusion

High power laser systems and connected experiments require a large variety of infrastructural components. Generating high intensity laser pulses alone is challenging, however for a successful realization of high intensity laser plasma experiments more is necessary than just generation of intense laser pulses. The laser needs to be transported to the experiments in vacuum via a laser beam delivery and also the experiments itself are complex setups. At the example of laser ion acceleration we showed the demand on accurate laser characterization, target delivery and positioning as well as target production and characterization. Target production at LMU is capable of producing a large variety of targets concerning thickness range and materials. The technological demands on target production have grown in the last years, as the target throughput has increased with high repetition rate experiments. On a typical experimental day in LEX more than one full target wheel was shot ($>$ 2000 targets) which highlights the demand for mass production of targets and automatized characterization. In the further sections, we will focus on special topics as the technological challenges for high power laser systems and connected experiments, namely the transport of the laser pulse to the experiment via laser damage threshold measurements and online laser and target characterization at the experiment with an advanced vacuum microscope.

Chapter 3

PW optics: Laser induced damage threshold Measurements

In this chapter we discuss PW class laser optics and laser damage tests on them. For the laser damage tests, the ATALS300 laser was used, as well as for other experiments performed at LEX-photonics [27]. Mirrors for ATLAS laser beam delivery in LEX-photonics and CALA were the central topic of the laser damage measurement campaign. Further expensive and potentially big scale optics like pulse compression gratings were as well investigated with regards to their behavior under high-fluence irradiation in high vacuum environment.

3.1 Motivation

Development of ultra high power laser systems strongly relies on accurate information of laser damage threshold of critical components, as it dictates the final size of the required optical elements and thus scales the prize of the laser more than anything else. In CPA systems, components like pulse compression gratings for compression of the stretched beam, and transport mirrors for guiding the laser pulse to the experiments are the most critical components, since they are complicated to fabricate and fragile. To retain the high quality of the laser pulses, these components are typically operated in high-vacuum ($\approx 10^{-6}$ mbar). The laser damage threshold fluence is pulse length dependent and decreases significantly with shorter pulse length [97]. Ultimately laser damage threshold dictates the size of the optics and reflects a tremendous burden on fabrication and budget. Laser damage, especially

in the femtosecond regime, is a complex process, which involves various nonlinear ionization processes and relaxation mechanisms. Although the physics behind these mechanisms have been well studied, it is not possible to reliably predict laser damage threshold and consequently the optics lifetime for arbitrary combinations of laser parameters, optical coating properties, and ambient conditions. Laser damage threshold thus needs to be measured. The required test stands are not yet routinely commercially available, tests under controlled vacuum conditions not at all. Therefore we set up a vacuum laser damage threshold setup, in which we tested samples of candidates for laser beam delivery mirrors and pulse compression gratings for ATLAS3000 at CALA.

3.2 Theoretical understanding of laser induced damage

In this section we analyze the theoretical aspects involved in creating damage with high intense laser pulses in matter. We will describe mechanisms responsible for single pulse optical breakdown and expand existing models for multiple pulse damage mechanisms. The main aspect will be on short pulse ($\tau < 10$ ps) laser interactions, as this is the pulse regime where most high power laser facilities are operating.

3.2.1 Laser parameters and definition of laser damage

Before discussing physical mechanisms, the terminology of laser damage should be explained. **L**aser-**i**nduced **D**amage **T**hreshold (LiDT) is typically defined as the highest laser fluence or intensity a material or device can withstand before breaking down. More precisely in ISO21254-1:2011 [24] laser damage is defined as: *any permanent laser-radiation-induced change in the characteristics of the surface of the specimen which can be observed by an inspection technique and at a sensitivity related to the intended operation of the product concerned.* We introduced the fluence, which denotes the energy over an illuminated area:

$$F_L = \frac{E_{pulse}}{A}$$

Where E_{pulse} denotes the laser pulse energy and A the illuminated area. For a Gaussian laser beam the area is commonly defined as the area covered by a circle with diameter of the beam waist ω. Quantification of laser damage in fluence may have historical reasons, as the very first laser damage reports

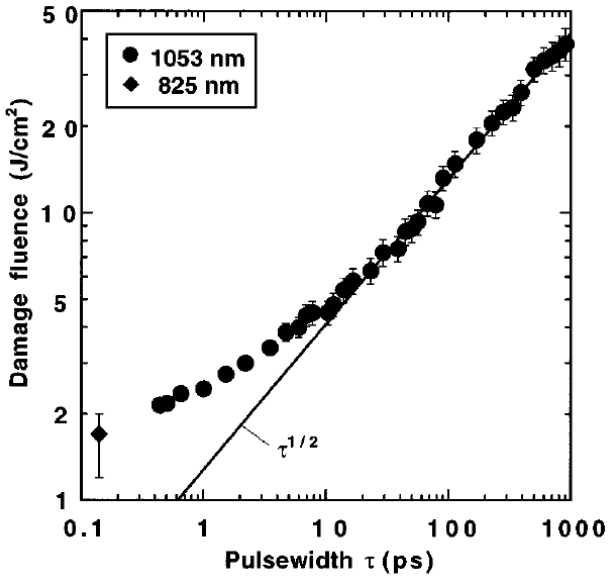

Figure 3.1: Pulse length dependence of LiDT of fused silica and $\tau^{1/2}$ scaling. Picture taken from [96]

denoted the thresholds also in fluence [6], but further for practical reasons[1]. A quantification in intensity would ostensibly appear more convenient, as the dominating mechanisms for laser induced damage are intensity driven [62]. However neither intensity, nor fluence contain enough information about the temporal pulse shape, as the laser damage threshold is dependent on the laser pulse length [82, 97, 74]. Given a temporal Gaussian pulse shape and a known pulse duration, stating fluence or intensity bears the risk of arbitrariness, as a single number represents only an average or maximum value of a potentially complicated distribution function. In this thesis, according to the literature, we will state laser damage threshold in fluence. More precisely we will define LiDT in peak fluence ($max[F_l(x, y)]$), which is preferable for mirror classification in laser systems, which use non Gaussian beam profiles (i.e. flat top beams). In figure 3.1 the dependence of the damage threshold on the pulse length can be seen, where a nonlinear dependency of the LiDT on the pulse length is visualized. Also the $\tau^{1/2}$-scaling [97, 74] is visible. For laser pulses longer than 10 ps the damage threshold follows a $\tau^{1/2}$ dependency of fluence [82]. This is an empirical law for laser damage threshold determination and scaling and has been proven in numerous experimental studies [6, 103]. The $\tau^{1/2}$ scaling is based on the assumption that laser damage is created due to absorption in a thin layer of transparent material on an

[1]For high intensity laser it is more common to measure pulse energy than intensity

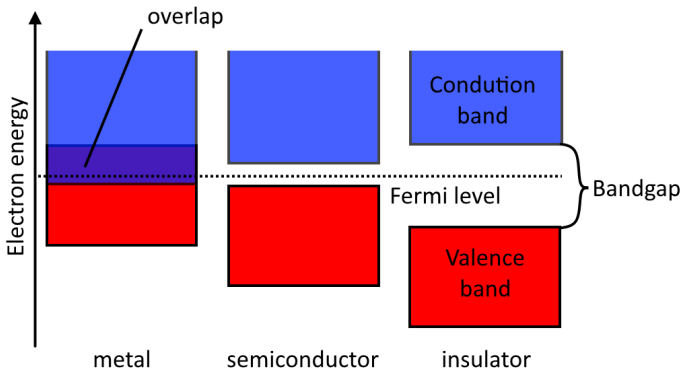

Figure 3.2: Comparison of the band structure of an isolator, semiconductor and metal

interface and the one dimensional heat dissipation into the surface therein [92].
With pulses shorter than 10 ps this scaling is not applicable anymore, which has first been observed by [21] and further investigated by [96]. In this regime, thermal effect become insignificant and laser damage is purely dependent on nonlinear ionization processes, which will be discussed in the following sections.

3.2.2 Laser induced damage in dielectric materials

As already stated, laser damage is dependent on the laser pulse length. Therefore laser damage can be classified in different regimes:

Thermal breakdown: For cw-lasers and long laser pulses ($\approx$ 100 ns) the damaging mechanisms are caused by heating and thus thermal stress or local melting of the optical surface. Defects in the material cause absorption of laser power and are transformed to heat. If the absorbed laser power is higher then the heat dissipation, thermal stress is induced and damage is created.

Ionization and thermal effects: For shorter laser pulses ($\approx$ 100 ns to 10 ps) defects in the material cause charge carrier generation and with the seed of this carriers, avalanche ionization and thermal stress cause damages. More details on the ionization mechanisms are given later in the text. This regime

was empirically found to scale with the square root of the pulse length ($\tau^{1/2}$)

Nonlinear absorption mechanisms: For ultra short laser pulses ($\tau < 10$ ps), damage is created via nonlinear photo ionizations and avalanche ionization mechanisms. Defects in this regime lower the laser damage threshold, however the limits of the laser damage threshold in this regime is not dependent on defects, but on material properties[2] [21].
A simplified model of the electronic structure of dielectric materials shows a valence band and a conduction band. At room temperature only the valence band is populated with electrons. The conduction band is several eV higher than the valence band, which is higher than the photon energy of optical photons (800 nm $> \lambda >$ 400 nm $\rightarrow$ 1.55 eV $< E_{photon} <$ 3.1 eV). The energy difference between the two bands is called band gap. An overview can be seen in figure 3.2. Electrons in the valence band are in the Coulomb potential of the atom and thus not freely movable. The absorption of photons of lower energy than the band gap is only possible via nonlinear interactions. Once the electrons are in the conduction band, they can efficiently absorb photons, because of the quasi continuum energy structure.
One established metric for laser damage threshold is when the free charge carrier number (number of electrons in the conduction band) reaches a critical density n_{cr} [62]:

$$n_{cr} = \frac{\epsilon_0 m_e}{e^2}\omega_0^2 = \frac{4\pi^2 c^2 \epsilon_0 m_e}{e^2 \lambda_0^2}$$

Where ϵ_0 is the dielectric constant, m_e the electron mass, e the electron charge, ω_0 and λ_0 the angular frequency and the wavelength of the laser respectively. For a 800 nm laser we calculate a critical density $n_{cr} = 1.74 \cdot 10^{21}$ cm^{-3}. If the carrier density in the conduction band reaches the critical density, strong absorption of laser energy occurs and damage is imminent [62]. The electron density N of the conduction band can be approximated by a simple rate equation [62]:

$$\frac{dN(t)}{dt} = \beta_m [I(t)]^m + \alpha N(t) \xi I(t) - \frac{N(t)}{T} \tag{3.1}$$

Where m is the number of photons required to excite the electron above the band gap (6 photons for a 800 nm laser and fused silica $E_g = 9$ eV). N is the electron density, $I(t)$ is the pulse intensity, α is the avalanche coefficient, β_m is the multiphoton absorption (MPA) coefficient of order m, T is an effective

[2]The electronic bandgap has the strongest influence on laser damage threshold

relaxation time.
Equation 3.1 was solved numerically for a Gaussian pulse of 25 fs FWHM pulse length and fused silica as substrate material, with the parameters taken from [62]. With a peak fluence of 2.7 $\frac{\mathrm{J}}{\mathrm{cm}^2}$ the critical density is reached, which is slightly higher than literature values [99, 12], but significantly higher than the measured single shot LiDT for fused silica in this thesis ($1.0\pm0.1\frac{\mathrm{J}}{\mathrm{cm}^2}$). The deviation from theoretical and literature results can be explained by higher absorption of laser energy due to impurities of for example OH^- groups in the substrates. In this section we analyzed UV grade fused silica substrates from Thorlabs. By analysis of equation 3.1 three effects for change in the charge carrier density are visible: Nonlinear photo ionization, impact and avalanche ionization and decay of electrons into lower energy states.

Nonlinear photoionization

The first term $\beta_m[I(t)]^m$ describes the nonlinear photoionization. There are two models for nonlinear ionization with photons, which have less energy than the band gap of the material. They are called *multiphoton ionization (MPI)*, a process, in which absorption of multiple photons lift electrons from the valence band to the conduction band and *tunneling ionization*, in which the electric field bends the coulomb potential in order to lower the ionization threshold. The processes and which process is dominant for given laser parameter is given by the Keldysh theory [76, 45]. Moreover Keldysh introduced a parameter, which was later called Keldysh parameter γ. γ indicates, which ionization mechanism is dominant. The Keldysh parameter is defined as follows [85]:

$$\gamma = \frac{\omega}{e}\sqrt{\frac{m_e c n \epsilon_0 E_g}{I}}$$

where is E_g the ionization energy of the material, ϵ_0 the dielectric constant, m_e the electron mass, c the speed of light in vacuum, ω_L the angular frequency of the laser light, e the electron charge, n the refractive index of the material and I the intensity of the laser light. For Keldysh parameters greater than 1.5 multiphoton ionization is dominant and for values smaller than 1.5 tunneling ionization is the dominating ionization process. An overview can be seen in figure 3.3. γ is linearly dependent on ω_L and thus with increasing photon energy, MPI becomes more dominant. This can be explained by 2 effects: With higher ω_L the laser field is oscillating faster and the time for an electron to tunnel through is reduced. This reduces the probability of this effect. Also for higher photon energies, less photons are necessary to bring electrons into the conduction band. This can also be measured. The laser damage

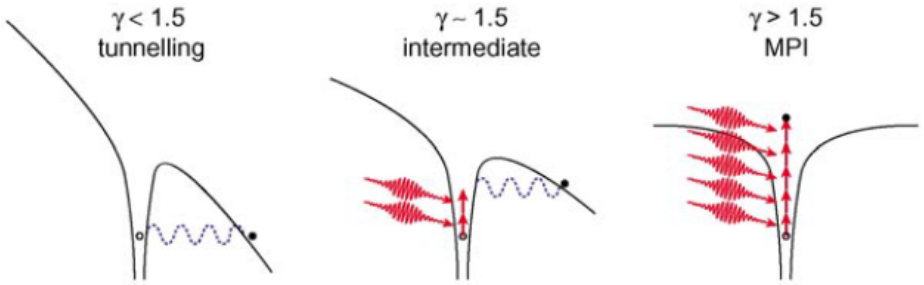

Figure 3.3: Multiphoton and tunneling ionization dependent on the Keldysh parameter. Picture taken from [85]

threshold changes step like, if transitions from 2 to 3 photon- or 3 to 4 photon process are reached [10]. In the case of laser damage in fused silica (bandgap $E_I = 9\text{eV}$ [67]) the ionization process starts with MPI until intensities of approximately $I \approx 3 \cdot 10^{13} \frac{\text{W}}{\text{cm}^2}$ are reached. Then the ionization mechanism transitions to tunneling ionization. Thus a constant multiphoton absorption coefficient β_m is questionable, however in [62] it was claimed, that ionization with the full Keldysh theory gave similar results.

Impact and avalanche ionization

The second term $\alpha N(t)\xi I(t)$ describes the impact and avalanche ionization. Once electrons are in the conduction band, they absorb photons via the free carrier absorption. These electrons can ionize further electrons via impact ionization, increasing the number of electrons in the conduction band. Presence of more electrons and the associated stronger absorption leads to increased rate of impact ionizations. This process leads to an exponential rise of the electron density in the conduction band, thus called avalanche ionization. An illustration of this process is given in figure 3.4. Avalanche ionization grows stronger with increasing pulse length. Regarding a constant laser pulse energy, and rising pulse length (which leads to lower intensity), the integrated term $\alpha N(t)\xi I(t)$ stays constant, while the MPI decreases non-linearly, due to the lower intensity. Avalanche ionization thus becomes the most dominant effect for an increase in charge carrier density for laser pulses longer than $\tau > 5$ ps.

Electronic decay

The third term $\frac{N(t)}{T}$ describes the decay of electrons from the conduction band into the valence band with the decay time T. Typical decay times are

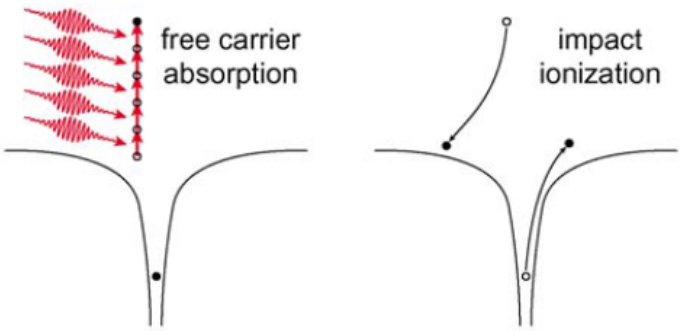

Figure 3.4: Free carrier and impact ionization. Picture taken from [85]

100-1000 fs (220 fs for fused silica) [62]. Electrons dissipate their energy via electron-phonon coupling or by emission of a (UV) photon. Both effects are material dependent, for example by the crystal structure or the electronic bandgap. Decay into the valence band generates heat, which is dissipated into the ion lattice.

3.2.3 Laser damage in conducting materials

In contrast to dielectric materials, metals and other conducting materials the conduction band is populated with electrons at room temperature (compare figure 3.2). The free electron density of metals is in the order of 10^{23}cm^{-3} and thus higher than the critical plasma density for optical wavelengths ($10^{21} - 10^{22}\text{cm}^{-3}$). Light cannot propagate into the material and is shielded over a distance called skin depth. The skin depth is dependent on the material electron density and the laser wavelength. For a 800 nm laser and gold we derive 15 nm[3]. In this layer, fraction of the pulse energy is absorbed. In metals, the conduction band is not completely filled and a photon can lift a electron from a lower electronic state into an excited state. This is called intraband absorption. The decay of the excited electron causes a rise in the electron temperature and has a time scale of a few femtoseconds [41]. The absorption is dependent on the configuration of the conduction band and thus material dependent. Silver for instance has an absorption at 800 nm of less than 1 %.
A widely accepted and developed model to describe the coupling between electron temperature and lattice temperature is the two temperature model [13]. In the two temperature model the absorbed fraction of the laser pulse energy is converted into hot electrons. This is commonly referred to as stage

[3]skin length: $d_{skin} = \lambda_0(2\pi\sqrt{\frac{n_e}{n_c} - 1})^{-1}$

one. Due to electron-electron collisions a thermal distribution evolves. The heated electrons now have a temperature much higher than the temperature of the lattice. Energy transport and thermal diffusion occurs via phononic scattering (stage two). The final state is when the electron temperature equals the lattice temperature. Whenever the lattice temperature reaches a critical point (i.e the melting temperature of the material) irreversible damage will occur, due to melting or mechanical stress in the layer. The two temperature model is described by the two following equations [41, 13]:

$$C_e(T_e)\frac{\partial T_e}{\partial t} = \nabla[k_e(T_e)\nabla T_e] - G(T_e - T_i) + S(z,t) \tag{3.2}$$

$$C_i(T_i)\frac{\partial T_i}{\partial t} = G(T_e - T_i) \tag{3.3}$$

The equations above consider the change of the electron and ion lattice thermal energy inside a infinitesimal small volume. T_e and T_i are the electron and lattice temperatures. C_e and C_i are the heat capacities of the electrons and the ion lattice. G is the electron lattice coupling coefficient. S represents the laser source (in W/cm^3). $k_e(T_e)$ is the free electron heat conductivity. The first term describes the change of the electron thermal energy (heat) and thus also the temperature[4]. Absorption of laser energy increases the electron temperature, while coupling to the lattice reduces the electron temperature. $\nabla[k_e(T_e)\nabla T_e]$ describes the thermal heat dissipation along the temperature gradient. The ion temperature is only changed by transfer of electron heat to the ion lattice. Damage is created if the ion temperature T_i reaches the melting temperature of the material T_m

In metals nonlinear ionization terms play a minor role and the electron and ion temperatures are determined by the absorbed laser energy. If the laser pulse is shorter than a critical pulse length, the laser damage threshold is not dependent on the pulse length [41, 13]. For gold this critical time was modeled and experimentally verified as $\tau_{cr} = 10$ ps [41]. This can be understood with the coupling of electrons with the lattice. If we consider formula 3.2 and neglect temperature gradient, the electron temperature rises fast during laser illumination and declines slowly by lattice dissipation. This behaviour is indicated in figure 3.5. In this figure the electron and ion temperatures have been modeled by usage of 3.2 and a laser pulse at 800 nm and 100 fs pulse length. For short laser pulses ($\tau < 1/g$) no significant energy is dissipated from electron heat to ion heat during the pulse interaction. The lattice is heated after the laser pulse has already deposited its absorbed energy into

[4] $C_e(T_e)$ and $C_e(T_e)$ are in principle dependent on the temperature. However for simplicity we assume them constant, which is valid for temperatures above 400 K [41].

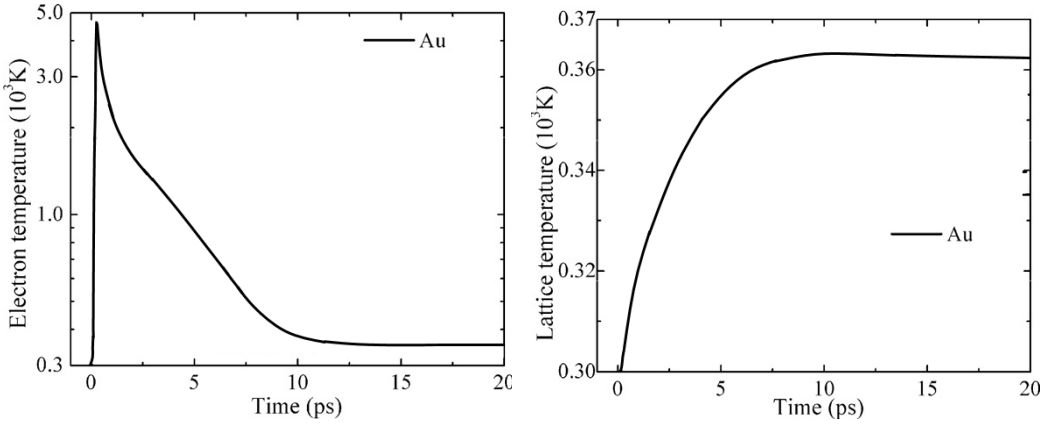

(a) Electron temperature (b) Ion temperature

Figure 3.5: Electron and ion temperature of gold during illumination with an 800 nm 100 fs laser pulse at a fluence of 100 $\frac{\text{mJ}}{\text{cm}^2}$. Pictures adapted from [11]

the electron system. If the laser pulse is longer ($\tau > 1/g$) then energy is transfered from the electronic system during the pulse interaction and the lattice can dissipate the heat. Thus more fluence is needed to reach the melting temperature and the damage threshold rises. This makes metal mirrors particularly interesting for femtosecond lasers, because the damage threshold practically becomes comparable to the LiDT of dielectric materials.
The damage threshold can also depend on the layer thickness and the connecting substrate, if the thickness of the metal layer is below the range of the electronic transport. The critical layer thickness, which was attributed to the range of electronic transport was experimentally determined for gold to be 180 nm [48] [106, 13], which is much larger than the skin depth. If the metal layer is thinner than the critical layer thickness, the damage threshold is lower than for bulk material, because heat transfer to the support layer can cause thermal stress.

3.2.4 Multiple pulse damage

While single pulse damage (ablation) is mostly interesting for material machining and for academical interest [28], most users are interested in the lifetime of an optic. Thus it is important to analyze the damage behavior when a substrate is illuminated with multiple pulses. It has been shown in numerous experiments that the damage threshold of multiple pulse illumination of samples is lower than for single pulse illumination [99, 62, 61, 97]. One

explanation for a lower damage threshold for multi pulse illumination can be explained by gradual degradation of already exiting defects. Impurities in the material cause a locally increased laser absorption and thus causing an imbalanced heat distribution. If the power input is higher than the heat dissipation of the material, thermal stress is induced and damage grows at this location. Similar behavior can be attributed to lattice defects, which can cause a population of the conduction band at room temperature. Impact and avalanche ionization and subsequently the decay of electrons back to valence band can cause a growth of an already exiting defect. This is relevant for all pulse durations, however it is more pronounced for longer pulse durations (100 ps and longer) [7]
Besides the defect absorption, it is interesting that a damage threshold reduction can also be observed for pure, defect free materials when illuminated with multiple laser pulses.
For short pulses, the heating of material is faster than the thermal transport. This means, that the material is heated faster, than the electrons and phonons can dissipate the heat. This explains the sharp boundaries in short pulse ablation. Also the effected region is limited by the range of the electric field in the material. Thus in case of dielectric mirrors, the top layer is the first to get damaged. The lower laser damage threshold can thus not sufficiently be explained by degradation of defects, but by a change of the material properties. During illumination with short pulses below the ablation threshold, long living interband states can be populated (so called "self trapped excitons" or STE), which can result in, for example color center formation [40]. The lifetime of such exited states can range from minutes to several month at room temperature [36]. These trapped states have a lower ionization threshold and thereby lower the threshold for free charge carrier generation. Equation 3.1 can be expanded by integration of STE generation [61]:

$$\begin{aligned}\frac{dN_{CB}(t)}{dt} =& \alpha N_{CB}(t)I(t) + \beta_m I(t)^m + \sigma_{STE} N_{STE}(t) I(t)^n \\ & - \frac{N_{CB}(t)}{T_{STE}} \left(1 - \frac{N_{STE}(t)}{N_{STE,max}}\right) - \frac{N_{CB}(t)}{T_{VB}} \qquad (3.4)\\ \frac{dN_{STE}(t)}{dt} =& -\sigma_{STE} N_{STE}(t) I(t)^n + \frac{N_{CB}(t)}{T_{STE}} \left(1 - \frac{N_{STE}(t)}{N_{STE,max}}\right) \qquad (3.5)\end{aligned}$$

Where σ_{STE} is the cross section of an interaction with a STE, N_{STE} is the STE population density, n is the number of photons necessary for generation of an conduction band electron from a STE state, T_{STE} the decay time of an electron from the conduction band into a STE state and $N_{STE,max}$

is the maximum number of possible STE states. Equation 3.4 is an extension of the rate equation of the generated electrons in the conduction band via nonlinear ionization (3.1) with a source term of free electrons from STE states ($\sigma_{STE} N_{STE}(t) I(t)^n$). Equation 3.5 describes the population change of STE with T_{STE} denoting the decay time from conduction band into a STE state. The first term $-\sigma_{STE} N_{STE}(t) I(t)^m$ reduces the number of STEs due to ionization into the conduction band, while the second term $\frac{N_{CB}(t)}{T_{STE}} \left(1 - \frac{N_{STE}(t)}{N_{STE,max}}\right)$ describes the generation of STEs by decay of electrons from the conduction band. If $N_{STE} = N_{STE,max}$ no more STEs can be created, which explains the observed saturation of laser induced damage for large pulse numbers ($< 10^3$) to a constant fluence. Decay of STEs into the valence band can be neglected in both equations, because the decay time of STE typically exceeds 10s of minutes [83] which is much larger than the time between two laser pulses in Ti:Sa laser systems[5]. With the long decay time, also the independence of laser damage threshold on the repetition rate (in the range of a few Hz up to 1 kHz) can be explained [61].
Numerical simulation of a laser pulse with square temporal profile and Fluence F lead to a simple decay function for the laser damage fluence depending on pulse number [2]:

$$F_{\mathrm{th}}(N) = F_{\mathrm{th}}(\infty) + [F_{\mathrm{th}}(1) - F_{\mathrm{th}}(\infty)] \cdot \exp[-k(N-1)] \tag{3.6}$$

$F_{\mathrm{th}}(N)$ describes the function of damage fluence depending on pulse length and pulse number. $F_{\mathrm{th}}(1)$ is the single shot laser damage or ablation threshold. $F_{\mathrm{th}}(\infty)$ denotes the saturated damage fluence of the optic for infinite pulses. The empirical parameter k describes the strength of the incubation effect. The saturation of the laser damage fluence was explained by a saturation of STE states in the material. Thus for large k values, the saturation occurs faster.
We applied the model to the experimental evaluated data of this thesis and it can be said, that this model works well for a fused silica substrate, but in its simple form is not applicable for a mirror substrate. In figure 3.6 a comparison of the model applied to a LiDT measurement of fused silica and a mirror substrate can be seen. While there is a well overlap for the fused silica sample, no satisfying datafit for the real mirror substrate was possible. Consistent in both measurement is the biggest change in laser damage threshold is observable in the first 1000 laser pulses.

[5]There are also large laser systems with repetition rate of for example 1 shot every 40 min (Texas Petawatt) and other glass laser systems. However the trend is going to higher repetition rate systems.

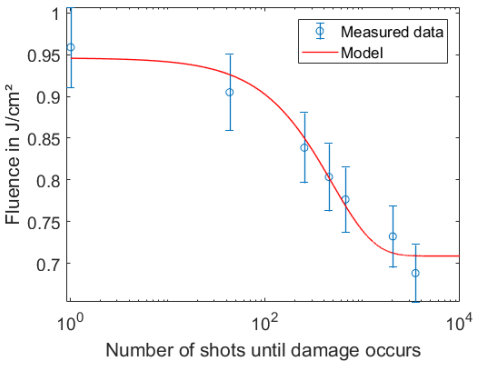

(a) Damage threshold of fused silica substrate

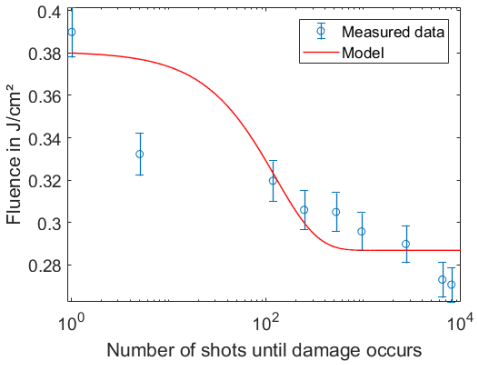

(b) Damage threshold of a mirror substrate

Figure 3.6: Laser damage threshold measurements and fitted model 3.6

3.3 Experimental evaluation of laser induced damage threshold

Though the physical processes that lead to permanent damage can be qualitatively understood on physical grounds described above, real world optics and mirrors in particular are very complicated objects. They are assembled from multiple layers of dielectric compounds with alternating refractive index in the optical thickness of a quarter wavelength. To increase the spectral bandwidth of such mirrors, the dielectric stack is often placed upon a reflective metal layer. Many parameters like layer density, coating technique and defects or impurities in each layer play a role in the final damage threshold. Thus small changes in production technique can have a strong effect on laser damage threshold[6]. The optimization over the past has therefore been accompanied by measurements of the damage thresholds.
We designed a setup for measuring the laser damage threshold of optics with sizes ranging from 1 to 4 inch diameter in vacuum. For laser damage threshold measurements, the precise knowledge of the fluence on the substrate and the number of pulses which are necessary to destroy the surface are required to calculate the laser damage threshold and predict the fluence for which the optic's lifetime becomes unlimited. The setup allows to continuously filter the laser energy, monitor the pulse energy of each shot, recognize damage online (during measurement), and precisely measure the laser intensity dis-

[6]We experienced this especially in section 3.5 where optimization of the coating technique led to a drastic increase in laser damage threshold

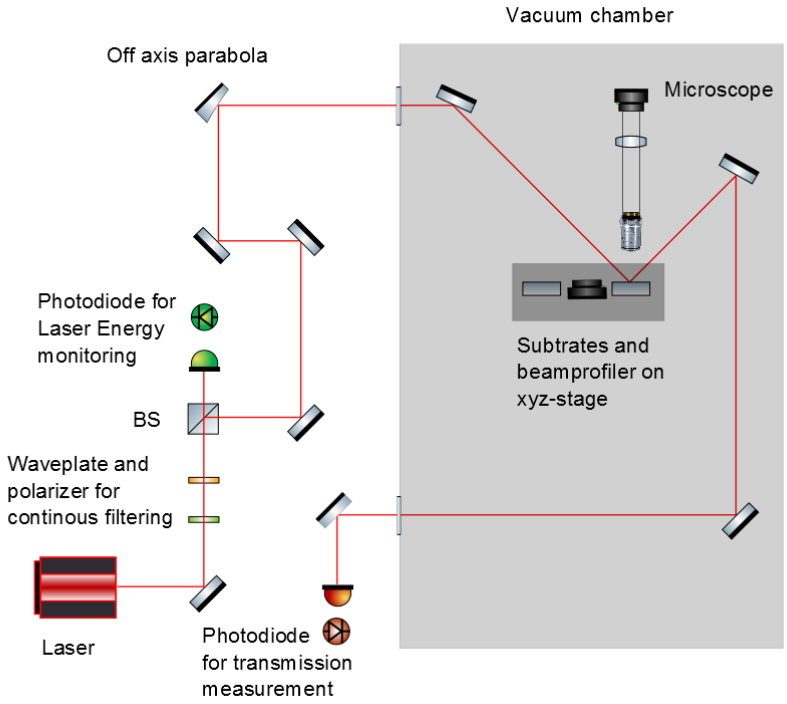

Figure 3.7: Laser damage threshold setup

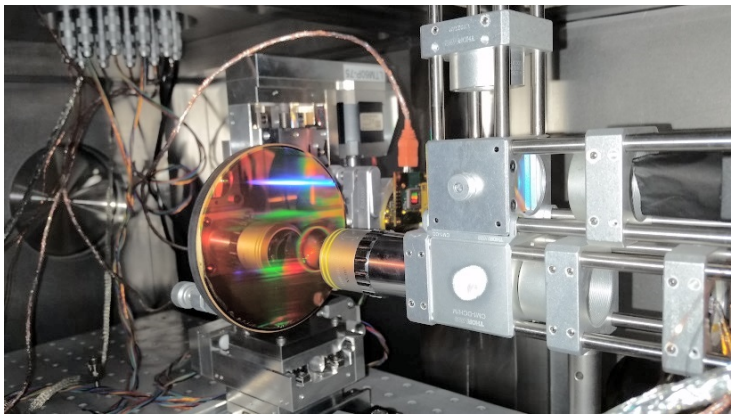

Figure 3.8: Laser damage threshold setup. View into the measurement chamber. A 4 inch grating substrate is mounted on one of the measurement ports

tribution on target for fluence calculation. The setup is housed in a vacuum chamber which allows evacuation down to $4 \cdot 10^{-7}$ mbar. The energy filtering is realized by a combination of a half waveplate and a polarizer. The polarizer has a maximum extinction ratio of 1:4000 giving the setup of a fluence control over more than 3 orders of magnitude. Software control of the waveplate rotation allows a full automatized measurement. To measure the energy of each shot, a part of the laser is sent to a calibrated photodiode. By sending the laser through a beamsplitter, the diode tracks the energy of each laser pulse. The photodiode is absolutely calibrated against a calorimeter, prior to each measurement campaign.
The laser[7] is focused on the sample by an off axis parabolic mirror with a focal length of 1500 mm. The target is positioned before focus to increase the area of illumination. By varying the distance to the parabolic mirror the area of the laser spot can be continuously changed and thus the fluence range can be adjusted. To measure the fluence distribution, the attenuated laser is sent on a camera chip at the same distance and the same angle of incidence as the substrate which is ensured by a vacuum microscope. Typical spot diameters are 150 µm (FWHM) diameter.
The vacuum microscope also serves to investigate the surface of the substrate during the measurement. An additional photodiode is placed close to the substrate to measure scattered laser light of the surface of the samples, which serves as an additional measurement for surface damage. A comparison of the two techniques can be seen in figure 3.9. At this example a clear rise in scattered light can be detected, as soon as surface damage is created. Both methods show similar detection capabilities. At lower fluence ranges the contrast of the scatter diode drops however. The same is true for naturally scattering surfaces like gratings. Ultimately the combination of both methods are used for determining the laser damage threshold as explained in the following sections.

3.3.1 Residual gas analysis of vacuum chamber

For measurements in vacuum an analysis of the residual gas is mandatory, because improper handling of vacuum components and non vacuum compatible objects placed in vacuum can lead to outgassing and thus to reduction of the final gas pressure and also to an undesired composition of the residual gas. High power laser systems are especially sensitive for hydrocarbon contaminations, as these molecules can lead to a build up of a carbon layer

[7] the beam waist was initially 25 mm. After filtering by a reverse apodizing filter the flattop beam was converted to a Gaussian beam with beam waist of 12 mm FWHM

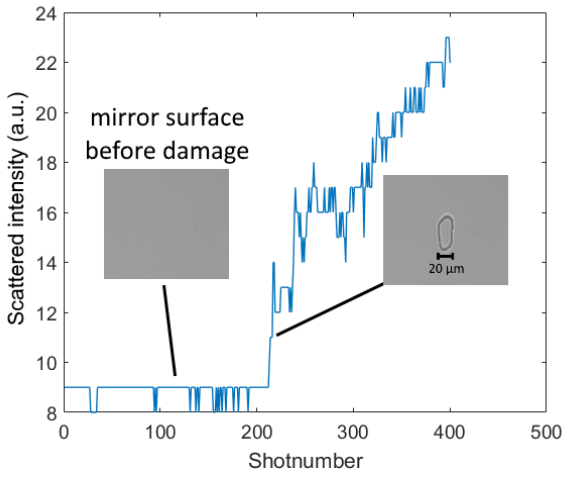

Figure 3.9: Comparison of scatter signal and online microscope detection before and after damage creation. A steep rise of scattered light can be detected when damage is created. Microscope images show a magnified region of interest.

on mirror substrates and other optical elements [81, 37]. For this reason the residual gas in the experimental chamber was regularly measured and analyzed. For the measurement we used a Balzer 4000 residual gas analyzer. In figure 3.10 a typical diagram can be seen. Signals of the mass spectrometer graph are marked with different colors, to indicate the origin of the signal. Hydrogen dominates the background gas, being higher by a factor of ≈ 8 than all other peaks. Air constituents like Nitrogen, Oxygen, water, Argon and CO_2 are also visible. Non air constituents are marked with brown color. They origin from hydrocarbon contaminations in the vacuum chamber. Hydrocarbons are emitted in vacuum from bearing greases, plastic insulations, dirt from insufficiently clean objects placed in the vacuum chamber and other comparable sources. The total amount of hydrocarbons from the diagram calculates approximately to 5% of the total residual gas. This is however a strong overestimation of a factor of 3-10. Hydrocarbons consist of big molecules (molecular mass of up to 200 u), and they are fragmented in the ionization process. While it is very difficult to analyze the true hydrocarbon content, the estimation by integrating the hydrocarbon peeks and comparison to the total amount, results in an upper limit. The measurement shown in 3.10 represents a moderately clean vacuum system, where efforts have been made to reduce the hydrocarbon content, but they could not be eliminated. This however reflects the true conditions of the optics use in the laser plasma experimental chamber, where hydrocarbons from greases and

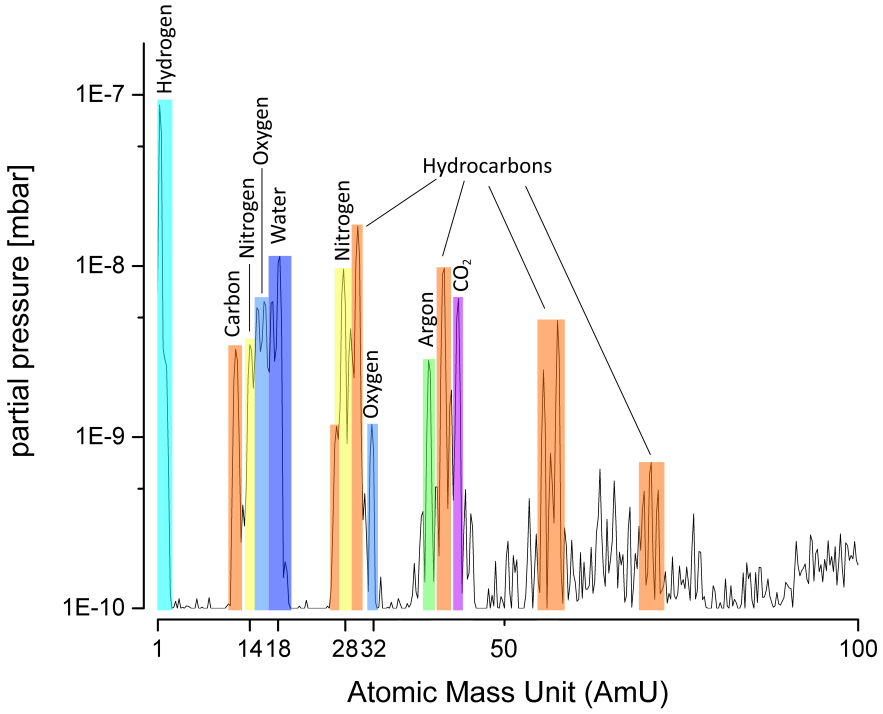

Figure 3.10: Residual gas analysis of the measurement chamber at a pressure of $5 \cdot 10^{-7}$ mbar. The different residual gases are marked. Hydrocarbons have several appearances, due to fragmentation during the ionization process in the mass spectrometry measurement

plastic insulation are present.
We measured the laser damage threshold of most of the mirrors in this thesis with comparable or slightly cleaner conditions, to see the effect of potential carbonization on mirror surface during high power laser illumination [81, 37]. For mirror samples no contamination of the optics during LiDT measurements could be observed. Thus the effect of the residual gas in the vacuum chamber on laser damage threshold measurements can be neglected.

3.3.2 Measurement Procedure

The photodiode which monitors the energy, is calibrated prior to each experimental campaign. This is done by placing a pyroelectric energy meter[8] close to the interaction point of the laser spot. A typical dependency of the

[8]Gentec Energymeter

laser energy versus the voltage of the photodiode is depicted in figure 3.11. For the laser spot size determination a vacuum compatible camera[9] is used. The camera is moved to the interaction point, which is verified by imaging the camera chip surface in the microscope. The z resolution of the microscope is 2 µm and the field of view is 68 x 54 µm. While the laser spot is adjusted to the center of the field of view of the microscope beforehand, the z-resolution defines the accuracy of the laser spot size measurement. With a total focal length of 1500 mm and an FWHM beam of 12 mm the radius of the laser spot changes slowly with variation of z-distance. Thus the error in laser spot size is negligible. The camera and two substrates are mounted on a xyz-stage. The laser is then attenuated and sent on the chip. A typical intensity distribution is shown in figure 3.12.
With the calibrated photodiode the energy of each laser pulse can be recorded. The size of the laser spot can be calculated by the ccd image of the attenuated laser. With these two values the fluence can be calculated. Details on the evaluation are presented in section 3.3.3. The measurement routine is motivated by the ISO standard for N on 1 measurement [24]. The routine for measuring the substrates starts with a high laser fluence, with which already few laser pulses will cause damage. The fluence is then decreased, the substrate is moved to a fresh area and the measurement is started again. To start the measurements, a clean area of the substrate is moved to the interaction area of the laser spot. The microscope observes the surface and saves an image after each shot. When a damage occurs, the laser is blocked, to keep the debris minimal on the surrounding surface. Then the substrate is moved to a fresh location, which is separated from the damaged one by at least 1 mm, and the illumination, with now decreased laser energy is started again. This procedure is repeated until no visible modification, analyzed online with the vacuum microscope, is measurable anymore after a predefined number of pulses (in our case 3000 pulses[10]). At the same fluence three more spots are measured, to ensure the stability of this substrate at the measured fluence with the defined number of pulses.

3.3.3 Evaluation

In accordance to the literature, laser damage thresholds in this thesis are measured and quantized in fluence. Fluence can be specified in beam normal or on substrate plane. Beam normal refers to the area enclosed by the normal

[9] IDS UI-1260LE-M pixel size 4.5 µm

[10] The ATLAS300 laser tended to drift in energy when used for several hours. This was difficult to compensate and longer measurements would have decreased the accuracy of the fluence per spot illumination

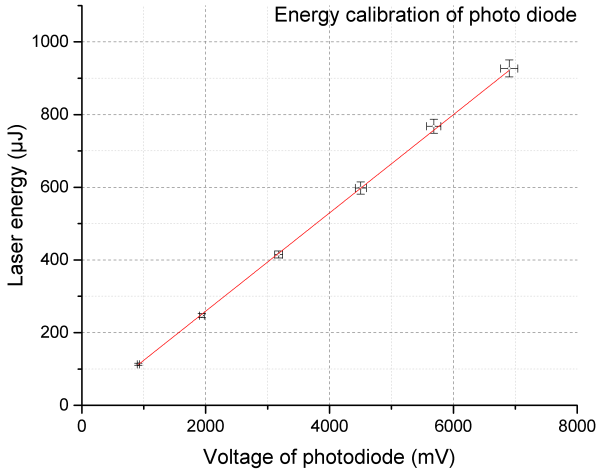

Figure 3.11: Photodiode voltage vs laser pulse energy. The line represents a linear fit.

beam, whereas the substrate plane fluence refers to the projected area on the substrate surface (compare figure 3.13). In this thesis all fluences are denoted in substrate plane. We measure target plane fluence, because by this, we eliminate uncertainties of the angle of incidence during measurement[11]. Motivated by experimental observations we denote laser damage thresholds in terms of peak fluence. In figure 3.12 laser damage of a substrate and the corresponding fluence map are compared. The outline of the laser damage is marked in both cases (single shot and multi shot laser damage) in the fluence map. For a single shot damage (in this case the fluence was higher than the ablation threshold for the material), material ablation starts already with 85 % of the peakfluence. If the laser fluence map however is compared to the area of a multi shot laser damage, we can see, that the corresponding fluence values in the fluence map are only 1-2 % lower than the peakfluence value. The peakfluence is derived numerically from the intensity profile of the laser spot, which was recorded by a ccd chip in target plane prior to each measurement. After background subtraction, the intensity profile is integrated. Each count of the intensity profile is then divided by the integrated value and the pixelsize[12]. By this we get a normalized fluence map. Multiplication of this normalized map with the laser energy derived from the calibrated photodi-

[11]The measurements have still been taken as close to the designed angle of incidence as possible

[12]in our case the pixelsize was 4.5 μm

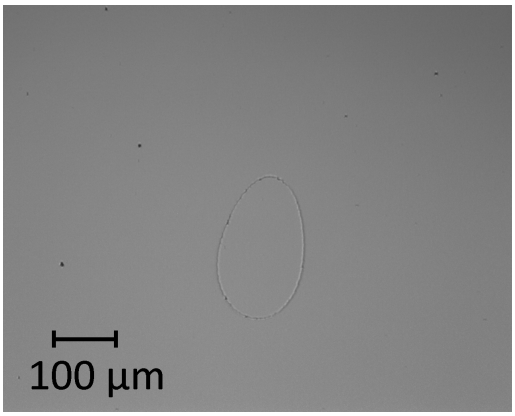

(a) Microscope image single shot damage

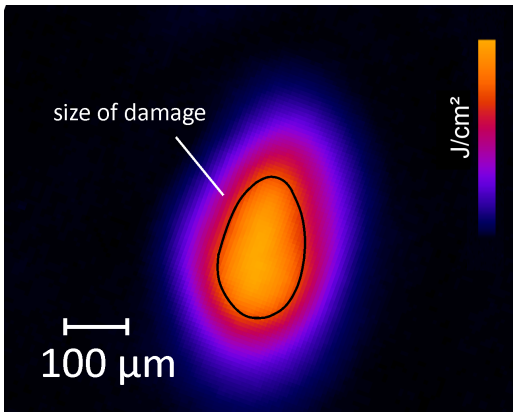

(b) beamprofile of laser. The black drawing indicates the outline of the damage left

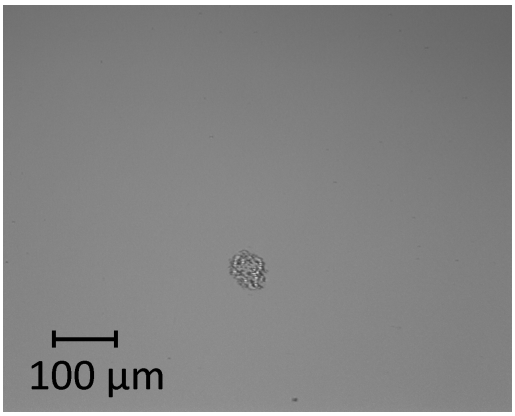

(c) Microscope image multi shot damage

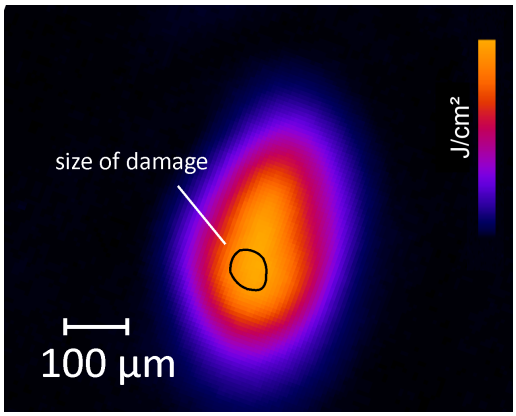

(d) beamprofile of laser. The black drawing indicates the outline of the damage left

Figure 3.12: Area of the laserspot and bright field microscopic picture of laser damage. The image of the laser spot has been magnified to fit the same magnification

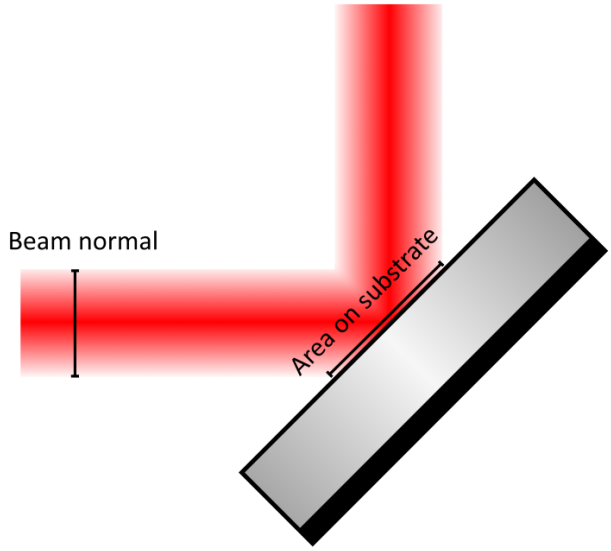

Figure 3.13: Laser fluence in beam normal and on substrate. In this thesis we measured fluence in substrate plane

ode results in the absolute fluence map, the maximum of which we attribute to the LiDT fluence. To evaluate after how many shots the substrate shows damage, two methods are available. On the one hand a microscope observes the surface of the substrate after each shot. Even very small defects[13] can be observed by this method. Additionally, a photodiode, which measures the scattered light is also available. For mirrors, the scattered light photo diode is a powerful measurement as already small defects on the mirror substrate results in a strong increase of scattered light. The sensitivity is in this case comparable with the microscope. To ensure consistent results, both measurements are always considered. If the damage is defined by the scatter diode, the microscope image complements and vice versa.
The calculated fluence and the number of pulses after which damage is observed is shown in figure 3.14. This example shows the behavior of laser damage when reducing the fluence. Reductions of the fluence of less than 10 $\frac{\mathrm{mJ}}{\mathrm{cm}^2}$ can result in an increase of pulses from 1000 to 3000. The shape of the curve indicates, that the number of pulses, that are required to damage a sample, grows exponentially towards lower fluence. Because of this behavior we concluded that the highest measured stable point at 3000 laser pulses is defined as 3000-on-1 laser damage threshold.

[13] depending on the contrast of the damages. For strong contrast damages like scatter centers, the resolution can be up to 2 μm. For lower contrast damages like slow blackening of the surfaces the resolution drops to typical values of 10 μm

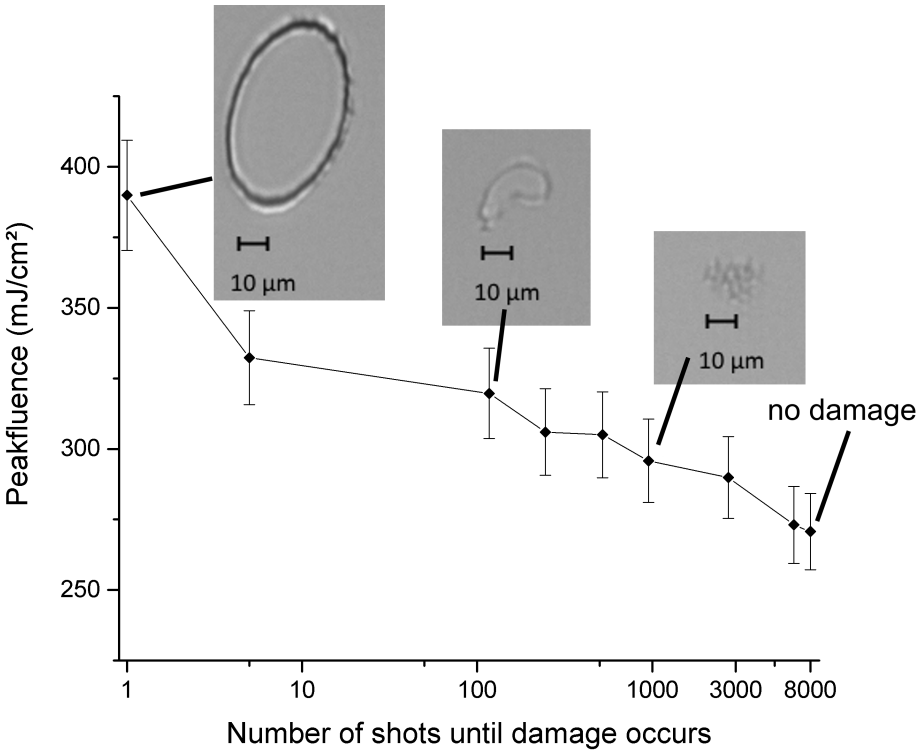

Figure 3.14: Laser damage diagram dependent on fluence and the number of shots until damage occurs. The microscope image indicates the resolution of the detected damage. Maximum pulse number in this measurement was 8000 pulses.

Substrate Code	LiDT few pulses	LiDT 3000 pulses
AIII	220	160
BI	284	225
CI	256	185
EI	200	100
FI	390	270
GI	153	110

Figure 3.15: Laser damage threshold of commonly used optics. Fluence in $\frac{\mathrm{mJ}}{\mathrm{cm}^2}$

3.4 Experimental results

In this section we present measurements of laser optics started in 2012 motivated by the first considerations for CALA and the laser beam delivery therein. Within the tender process it became obvious that not all companies were able to specify the LiDT for the conditions that we requested, i.e. under vacuum and for 20 fs pulses. We restricted tests to high power laser mirror samples, which were provided by companies, who could declare their capability to produce mirrors in the full size required for the CALA laser beam delivery[14]. Amongst the 4 companies of whom we tested mirrors that were specifically designed for high power, short pulse laser applications, the estimated LiDT-values differ from 160 to 270 $\frac{\mathrm{mJ}}{\mathrm{cm}^2}$. As in CALA the fluences are anticipated to stay below 100 $\frac{\mathrm{mJ}}{\mathrm{cm}^2}$, we defined the lower acceptable boundary of LiDT to 200 $\frac{\mathrm{mJ}}{\mathrm{cm}^2}$ for the 3000-on-1 LiDT. This includes a safety margin of 100% and was demanded from all optics suppliers for CALA.
The samples GI and EI were not optimized for laser damage threshold. GI was an unprotected silver mirror, which was a representative witness sample for a full scale off axis parabolic mirror and EI was a standard dielectric mirror substrate not specially designed for high power applications. By the comparison of the LiDTs of GI (metal mirror 110 $\frac{\mathrm{mJ}}{\mathrm{cm}^2}$) with EI (dielectric mirror not optimized for high power short pulse laser 100 $\frac{\mathrm{mJ}}{\mathrm{cm}^2}$) the considerably high LiDT values of metal mirrors in the femtosecond regime described in section 3.2.3 can be seen. Usage of metal mirrors in femtosecond lasers at low fluence levels is thus advisable, due to the low costs and the broad spectral reflectivity.

[14] 420 mm x 300 mm x 80 mm (compare 6.2)

Company	LiDT few pulses	LiDT 3000 pulses
LBD_AI3	550	450
LBD_AII2	460	420
LBD_BI3	420	400
LBD_CI2	460	400
LBD_EI1	420	330
LBD_FI1	420	350

Figure 3.16: Laser damage thresholds of the applied mirrors. Fluence in $\frac{\text{mJ}}{\text{cm}^2}$

3.4.1 Applicants for LBD mirror supply

After publication of the tender in the ted [101] (tender electronically daily) of the European Union, 5 companies have applied with a total amount of 6 different substrates for the damage threshold tests. 4 companies stated that they could deliver such mirrors in the given time and fulfilling the further specified constraints. All of the substrates were measured and the results can be seen in table 3.16. All of the substrates managed to have higher damage threshold than the demanded 200 $\frac{\text{mJ}}{\text{cm}^2}$.

3.4.2 Influence of vacuum on laser damage threshold

While the majority of laser damage threshold testings (also for fs laser substrates) are done in air, only few publications present their measurement in vacuum environment. Duy N. Nguyen et al [68] have compared a vacuum testing environment to air with laser damage tests on a single quarterwave layer of Hafnium dioxide on a quartz substrate. The result was, that compared to air environment, the laser damage threshold in vacuum environment drops significantly to less than 15% of the corresponding air value, when illuminated with $10^4 - 10^5$ laser pulses (compare figure 3.17). This is a severe effect and for this reason and also because the mirrors for the laser beam delivery are situated in vacuum we decided to measure laser damage threshold in vacuum atmosphere.
To analyze the effect on air or vacuum atmosphere we tested real mirror samples in 3 different atmospheres: Air, Nitrogen and vacuum ($5 \cdot 10^{-7}$mbar). The results can be seen in figure 3.17. If we compare the results in our setup with the results from Nguyen et al, we can see that even though the laser damage threshold in the two environments have the highest difference in very large pulse numbers ($10^4 - 10^5$ and higher) we can see the onset of a difference already at 1000 pulses and at 3000 pulses a significant difference is detectable. In our measurements, we could not detect a difference in laser

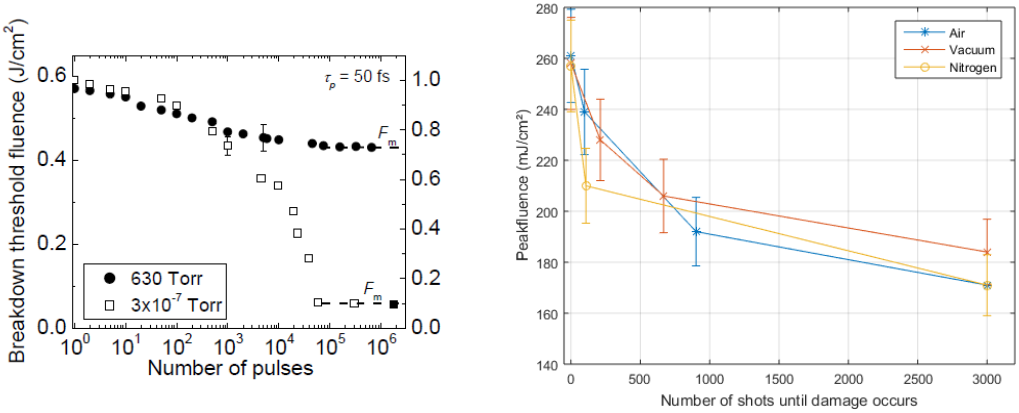

Figure 3.17: Comparison of LiDT in air and vacuum environment. Left picture taken from [68]. Right picture shows a measurement of a dielectric mirror with the setup in this thesis in air, nitrogen (both at atmospheric pressure) and vacuum (10^{-7}mbar).

damage threshold for these pulse numbers. Due to a 5 Hz laser system we are limited in maximum pulse illuminations. In figure 3.14 a measurement with 8000 pulses was performed, but here also no damage behavior for larger pulse numbers in vacuum as described in [68] could be observed. There can be various reasons for the adverse observations by Nguyen and our measurements, like different laser setups: Nguyen measured with 1 kHz whereas we measure with 5 Hz. Also dissimilar substrates were used: We used mirror substrates, while Nguyen et al measured with a single HfO_2 layer on a quartz substrate. Briefly it is difficult to state the reasons for the two opposing observations of the damage threshold behavior in vacuum.
Even though the effect of vacuum atmosphere to the laser damage behavior was not detectable in our setup, all mirrors were measured under vacuum atmosphere as this certified the vacuum compatibility[15] of the mirror samples and ensured closest resemblance with anticipated conditions of future use.

[15]We did indeed encounter effects like coating removal on some mirrors, which were used in the LEX beamline. This was not fully clarified, but we want to make sure, that the samples we measure do not encounter the same problem

3.5 Damage threshold measurements of pulse compression gratings in vacuum

To avoid nonlinear optical effects[16] and dispersion accumulation, compression of laser pulses in high power CPA-systems are realized in vacuum. The optical setup for this purpose is called compressor. Typically the compressor facilitates a negative dispersion realized with gratings or prisms [100]. In ATLAS300 and ATLAS3000 the compressor is comprised of 4 gold coated gratings with rule density of 1480 lines per mm. Due to the design of the pulse compressor, the last grating is always illuminated with short pulse fluence. This grating has to withstand the same fluence as the mirrors in the beamline. Due to the complex surface structure, gratings must be manufactured at highest precision, leading in consequence to significant costs and limited availability (only very few companies and institutes are able to produce gratings featuring a full aperture of 280 mm, in our case even just 2). Considering the cost and the importance of this element for the performance of the entire laser system, special care has to be given to this component.

For the CALA pulse compressor two companies applied for participation of the public tender, which will be called due to disclosure reasons competitor A and B, or in case of LiDT diagrams, grating A and B. Competitor B uses holographic inscription technique [84] for the production of their gratings. In this technique two laser beams interfere with each other at a certain angle. The resulting interferogram is a sinusoidal intensity pattern. The distance between two maximas is defined by the angle between the two laser beams. The interferogram illuminates a photoresist and after development, the 3d grating structure is inscribed on the remaining photoresist. This layer is then coated with a Gold layer. Competitor A uses a scanning beam interference lithography technique. By this technique, an interference pattern is moved step by step over the substrate with a stage of nanometer precision and illuminates the photo resist step by step. After curing, the structure is then etched into the substrate (in normal case fused silica) and then coated with a gold layer. Comparing the two companies and the production techniques, the biggest difference is that one grating has a photo resist underneath the gold layer (competitor B), whereas the other grating has the structure etched into the substrate (competitor A).

Figure 3.19 (a) presents LiDT measurements of two grating witness samples can be seen. The damage threshold of grating A is at 200 $\frac{\mathrm{mJ}}{\mathrm{cm}^2}$ for 3000

[16] Effects like selffocussing and filamentation

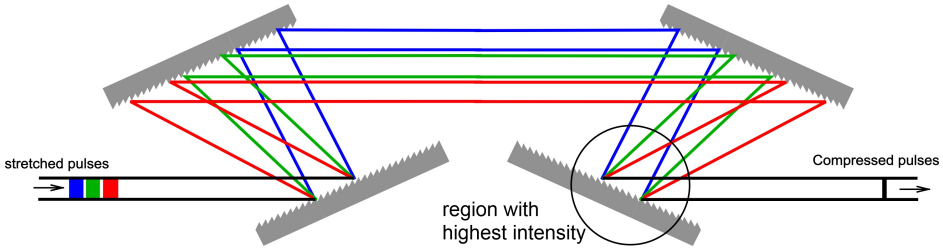

Figure 3.18: Typical setup of a grating type pulse compressor

pulses whereas the damage threshold for the grating B is at 8 $\frac{\text{mJ}}{\text{cm}^2}$. The latter case was surprisingly low and also the damage behavior was unusual. At pulse numbers beyond 500 pulses the surface started to show a blackening of the grating surface. An example of this behavior can be seen in figure 3.20. A detailed discussion of this effect is given in the next section. The unexpected low damage threshold of the grating B led to a retuning of production parameters[17]. Measurements for such an updated grating can be seen in figure 3.19 (b). The performance of this grating is highly improved, as we could measure a laser damage threshold of 250 $\frac{\text{mJ}}{\text{cm}^2}$ at 3000 pulses. Also no surface blackening during illumination could be observed.

3.5.1 Surface contamination during measurements

To analyze the unusual damage behavior of the grating sample in figure 3.19 (a), we investigated the damaged spots under the various fluences more closely. With the online brightfield microscope, we cannot distinguish coating removal from a build up of an absorbing layer like carbonization of hydrocarbon contamination [81] on the grating, as both of them cause a reduced brightness in the microscopic image. Both effects are undesirable, however a carbon contamination can be removed [31]. To identify the kind of surface alteration, the grating substrate was analyzed with a whitelight interferometer(WLI)[18]. With a WLI topographies can be measured. A coating removal will result in a lower topography than the surrounding layer, while a carbon contamination results in a higher topography.
In figure 3.21 an overview of 3 different fluence illuminations and damage topologies can be seen. On the left hand side, brightfield microscopic pictures, taken online during the measurement are shown. On the right hand

[17]Unfortunately they did not provide any details of the changes they made in the production line. However competitor B is now building up an own test facility to avoid such effects in the future and increase quality control

[18]Sensofar plu neox optical 3D profiler

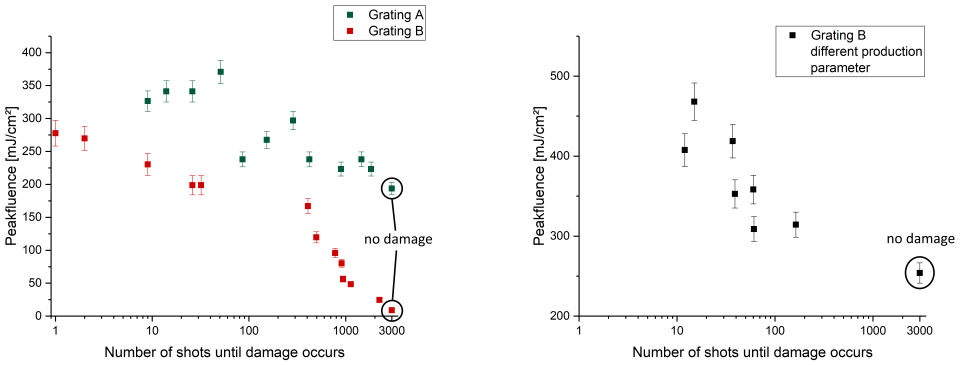

(a) LiDT diagram of gratings for CALA candidates

(b) Second grating of competitor B with adjusted production parameter

Figure 3.19: LiDT diagrams of CALA pulse compression gratings. Left the initial substrates for application. A large difference of laser damage is visible between the two samples. Right sample of competitor B with adjusted production parameters. Note the huge difference of laser damage behaviour between grating B left and right.

side the corresponding topographies are presented. The topographies are derived offline after measurement with a whitelight interferometer. The images are sorted from high fluence to low fluence, where the first row (image (a) and (b)) shows single shot damage. Here we can see, that the material is clearly ablated. The center spot is approximately 200 nm deeper than the surrounding layer. In (c) and (d) damage morphologies are shown in a fluence range slightly higher than the anticipated operation in CALA. Small craters in the center indicate damage, while the surrounding area has an accumulated contamination layer[19]. The contamination layer is approximately 60 nm thick. The last pair of pictures show a damage morphology corresponding to a lower fluence than the anticipated operation in CALA. Considering the topography, we clearly see a build up layer on the grating surface. The thickness of this layer is estimated to be 60-80 nm thick. The grating structure cannot be seen as with 1480 lines/mm the rule spacing is smaller than the resolution limit of the microscopes used.
The unusual damage behavior of this grating sample can be attributed to the build up of a contamination layer, during illumination with laser light of a fluence range of 200 $\frac{\text{mJ}}{\text{cm}^2}$ and lower. The influence of the vacuum system on

[19]The blackened region was identified as contamination, because the average layer height was higher than the non illuminated grating surface. The origin of the contamination layer however remain unclear

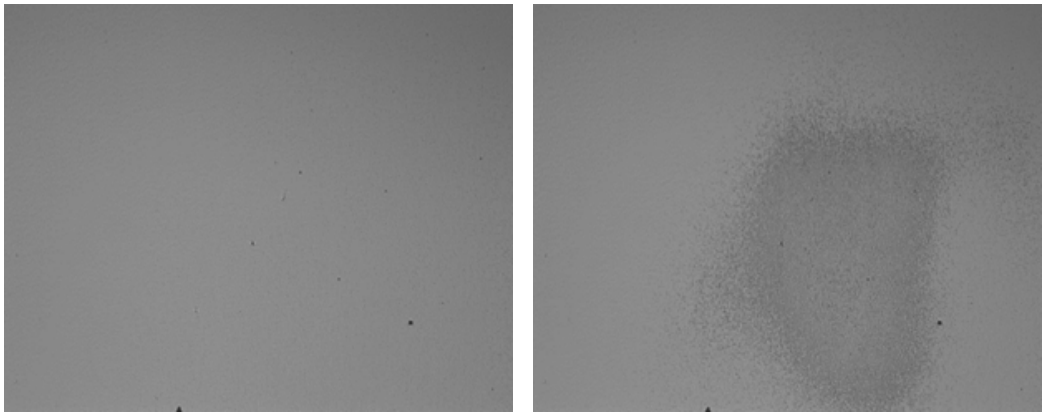

(a) Clean grating before measurement (b) Grating after 1500 laser pulses

Figure 3.20: Surface contamination of grating sample B during measurement in vacuum and fluence of less than 50 $\frac{\text{mJ}}{\text{cm}^2}$

the contamination can be excluded, as grating A was measured in the same vacuum environment and reference measurements at air with grating B also showed a build up of a contamination layer. While the detailed reasons for this behavior remain unclear, direct comparison with another grating sample, which underwent a different manufacturing process, suggests that the grating composition has a strong impact. The grating B had a photoresist layer underneath the gold layer, while a comparable other grating sample A (compare figures 3.19) had the grating structure etched into the silicon dioxide surface, which was then covered with a gold layer. As mentioned before, competitor B adapted the manufacturing process and this grating showed no contamination accumulation, when repeating the laser damage threshold measurements. Thus slight changes of production parameters can lead to a very large change of LiDT and underlines the importance of laser damage threshold measurements of every optical element in high power laser systems. Unfortunately, as end users we had no means to identify the determining factor.

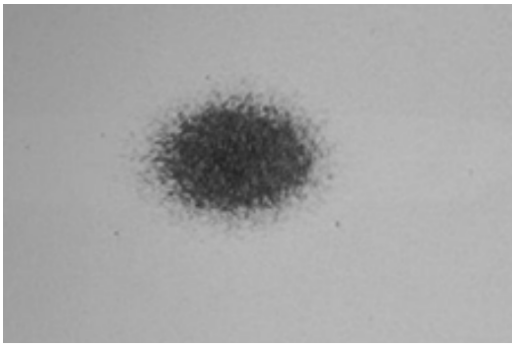

(a) Bright field image of single shot damage high fluence (400 $\frac{\text{mJ}}{\text{cm}^2}$)

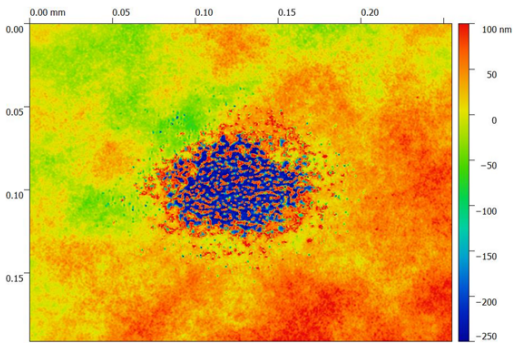

(b) Corresponding topography

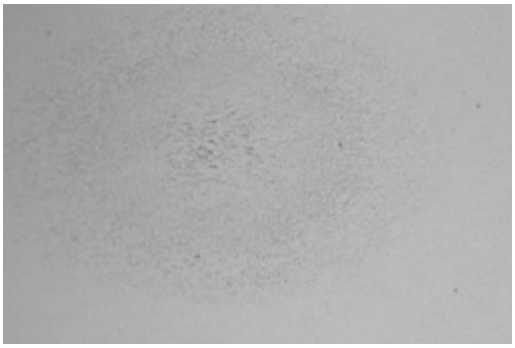

(c) Bright field image of multi shot damage intermediate fluence (100-200 $\frac{\text{mJ}}{\text{cm}^2}$)

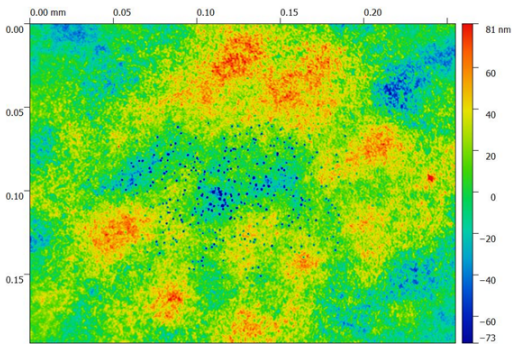

(d) Corresponding topography

(e) Bright field image of multi shot damage low fluence (<50 $\frac{\text{mJ}}{\text{cm}^2}$)

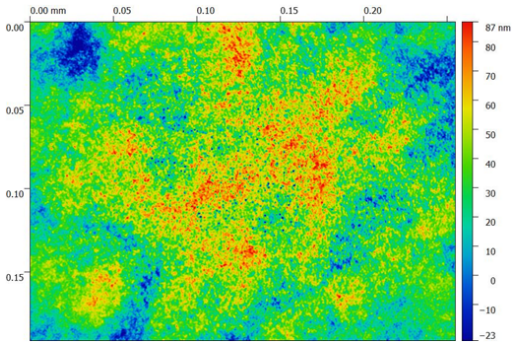

(f) Corresponding topography

Figure 3.21: Online brightfield image and offline measured topographies of grating sample B

3.6 Summary and conclusion

In this chapter we summarized physical background of laser damage mechanisms in the short pulse regime and showed the experimental realization of an accurate laser damage threshold measurement of high power short pulse laser optics in vacuum. With this experimental setup we were able to establish market overview in terms of laser damage threshold for common laser optics and demonstrated a significant variation among them. The introduced setup was a crucial part for selection of full scale mirrors for the CALA laser beam delivery as well as for full scale pulse compression gratings for the ATLAS 3000 laser. The latter case showed unusual behavior and led to further investigations. The conclusion for the pulse compression grating studies was, that these sensitive components need special care not only in regards of the laser damage threshold, as they are the most sensitive and also the most expensive optic in the laser chain, but also in non destructive, yet permanent surface alterations. We could observe contamination on the surface of a grating sample, which served as a witness sample for the full scale CALA optic at fluences well below the actual operation parameters. This example showed drastically the importance of careful laser damage threshold measurement in the actual operation environments. After these measurements the manufacturer retuned their production parameter, in order to improve the laser damage characteristics. The second version of this grating showed no contamination and also laser damage threshold was drastically improved (compare figure 3.19). Without careful testing in our lab, we would have bought and implemented gratings for ATLAS3000, which would have been unsuitable and let to a reduction of laser energy after a few hundred pulses and catastrophic damage of the gratings after a few thousand pulses. Furthermore the manufacturer got aware of the significant change of laser damage behavior with just slight adaption of production parameters and therefore decided to set up an in-house laser damage test site motivated by the measurements in this thesis. These results thus underline the importance of laser damage threshold measurement capability for design and realization of high power laser facilities.

Chapter 4

PW-lasers: Optical metrology

4.1 Introduction

In this chapter we discuss the optical metrology that was established to control the laser plasma interactions. Beginning with simple camera observations in vacuum, such as transmitted laser light through target, over to the characterization of the laser and the targets in vacuum with optical microscopy. The development of in-vacuum measurements is a step forward to commonly used relaying out of vacuum. This allows for a compact setup and adds more freedom in positioning of experimental diagnostics such as cameras or spectrometers for diagnostics of the plasma and particle beam parameters. With a large laser beam size and extensive diagnostics in a laser plasma experiment, a compact, well-behaved and ready-to-go focus-diagnostics is highly demanded. Laser ion acceleration is strongly dependent on delivering the high laser-intensity on few nm- to µm-thin targets. The targets vary from micrometer-thick nontransparent metal foils [86] down to few nm-thin foils [112, 54, 5]. High power short pulse lasers will be focused on such targets and ultra high intensities, well beyond $10^{18} \frac{\mathrm{W}}{\mathrm{cm}^2}$ will be generated. To generate these intensities fast focusing optics (i.e. off axis parabolic mirrors) are used to focus the collimated laser beam which (after its temporal compression) is delivered at its maximum diameter to the experimental chamber via the laser beam delivery mirror cabinet. For detailed diagnostics of the focus properties, and to define its position in the so-called target-chamber-center (TCC) in the experimental chamber, a focus diagnostics microscope is employed. In general this is realized with a microscope looking at the focus position, collinear with the laser axis. Optimization of focus and careful positioning of targets to the focus position is required in order to achieve the highest intensities at the target surface. The novelty in this work was to bring the

microscope fully into the experimental vacuum chamber avoiding a relaying the image out to a setup at air close to the vacuum chamber through a window, which usually takes significant effort and space for the beam-path, along with considerations of the optical properties of the individual setup. The benefits are the realization of a very compact design, which was quickly and seemlessly implemented in a series of experiments at different laser-systems. By addition of optical paths into the microscope design, more measurements could be realized: It was possible to add a wavefront sensor into the device, which paved the way for an integrated wavefront optimization routine with a simultaneous measurement of the focal spot. The addition of spectrometric measurements enabled a in-situ thickness determination directly before the laser-shot. A superior three dimensional target positioning could be realized with implementation of a whitelight interference measurement. The absolute distance measurement enabled by this technique can also be used for automized target alignment.

4.2 Vacuum compatible camera development

There are only very few commercial cameras available for vacuum use. Most of them are either very bulky or require external cooling and are usually very heavy (1 kg and more [110, 39]). Also the cost of such specially designed cameras is very high (10k EUR). Due to the harsh operation environment[1] expensive equipment with long lead times are undesired in laser plasma experiments. For alignment of the LBD (compare section 2.1.3) in CALA there was no other option than to use vacuum compatible equipment. Also for practical uses, building a completely vacuum compatible microscope tends to be very useful as lined out before. For these reasons we decided to develop our own compact vacuum compatible cameras based on commercially available scientific cameras[2].
Two main points are of concern, when putting electrical devices into vacuum: Heat production and outgassing. Both have been tested on so called board-level cameras of IDS-imaging. Cameras of this company have been used for several years already in laser plasma experiments. Furthermore these cameras are distributed to resellers as standard scientific cameras.

[1] The cameras we place in vacuum are also placed close to the laser plasma interaction. Thus they are exposed to EMP and particle radiation. The lifetime is usually limited in such environment and the ability to quickly replace units desirable

[2] `https://de.ids-imaging.com/home.html`

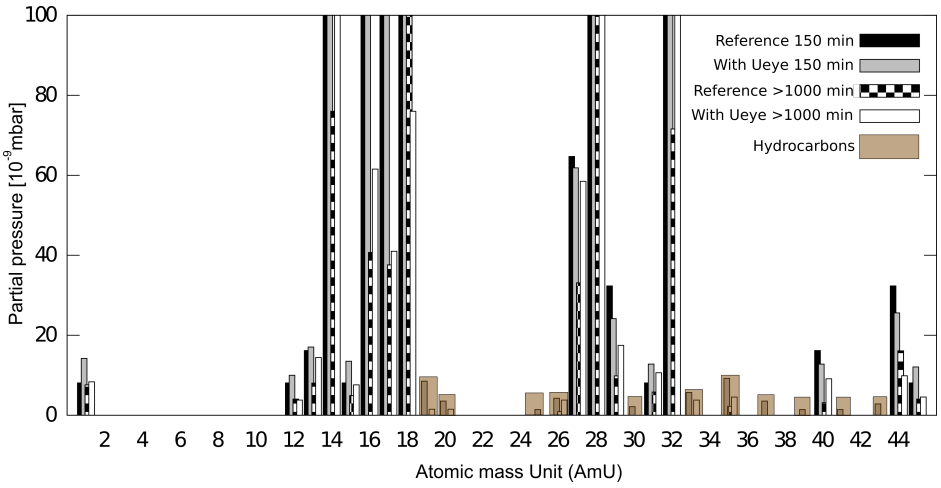

Figure 4.1: Residual gas analysis of a Ueye camera dependent on pump times. Picture adapted from [47].

4.2.1 Outgassing tests

Outgassing tests have been performed in framework of the bachelor thesis of Maximillian Koegler [47], who was supervised by the author and are shortly summarized here: Figure 4.1 shows a measurement of the residual gas depending on pumping time. To see the effect of outgassing of the cameras, measurements are compared with a camera in the vacuum chamber and a reference measurement with an empty chamber. A general increase of the partial pressures up to 50 AmU can be seen. The peaks at 14, 16, 18, 28, 32 40 and 44 AmU can be identified as Nitrogen (single atom), Oxygen (single atom), water, Nitrogen (molecule), Oxygen (molecule), Argon and carbon dioxide (molecule). These are the normal elements of air and considered as not harmful to optics in vacuum. An increase of the number of these elements can be explained with the bigger surface the camera brings to the vacuum environment compared to an empty chamber.
The other values (marked with brown color) cannot be assigned to normal air constituents. They are considered as hydrocarbons and fractions of them. The amount of hydrocarbons in the residual gas with the camera in the chamber are increased compared to the reference measurement. This can have two origins: Either the camera has non vacuum compatible components built in, which emit a constant flow of volatile hydrocarbons, or there are contaminations present on the surface of the camera. Thin surface contaminations however have a small volume and the emittance of hydrocarbons are decreased over time. If we take a closer look at the measurements in 4.1 we can see, that indeed the amount of hydrocarbons is reduced for longer pumping

times, which indicates that hydrocarbons originate from surface contaminations. A further decrease in outgassing can be expected for longer pumping times. Careful cleaning and soft baking at temperatures below 100 degrees can help to speed up this process.
In general it can be said, that the influence on the vacuum system is at an acceptable low level and not worse than other components like stages and other optomechanical components.

4.2.2 Passive cooling for vacuum use

In vacuum, heat can only be transported by heat conduction of contacting material or by heat radiation. The power of heat radiation is well described by the Stefan Boltzmann law for a black body $P_{Heat} = \sigma \cdot A \cdot T^4$, where P_{Heat} is the power of the heat radiation, σ the Stefan Boltzmann constant, A the surface and T the temperature. Heat radiation scales with T^4 and is thus not very efficient for low temperatures. The equilibrium temperature is met, when the heat radiation is equal to the power consumption of the camera[3]. Taking into account the values of our camera (2.9 W, 65° C maximum operation temperature) we get a surface of 40 cm^2 for a perfect black body radiator. With surface roughening of the cooling bodies and also the heat capacity, which buffers the temperature rise, these cameras can be cooled by passive radiation. Hot cameras tend to have higher dark current which limits the signal to noise ratio. Figure 4.2 shows that the noise is still acceptable at temperatures up to 65° C, but quickly rises for higher temperatures[4]. Temperatures higher than 70° C can lead to permanent damage of the camera.

For a proper cooling body design a detailed knowledge of hot parts is necessary. The IR image of the cameras during operation has identified the two large integrated circuits (IC) where most of the image processing takes place as the hottest parts. To cool the identified hot components, a copper cooler was designed, to thermally contact the surface of the hot ICs, without touching of the rest of the components, to avoid short circuits.
Various tests have been performed to evaluate the necessary surface to cool the camera to acceptable temperatures (compare figure 4.4). A numerical simulation was used to model the radiated power and the power brought into the system while calculating the changes in the temperature of the system dependent on the heat capacity in discrete temporal steps. The final

[3]The Ueye camera UI-5241LE-M has a power consumption of 2.2-2.9 W

[4]In this graph two exemplary images are taken at two different temperatures. The cameras have been blocked, so they recorded no light. The signal in the image is only due to dark current.

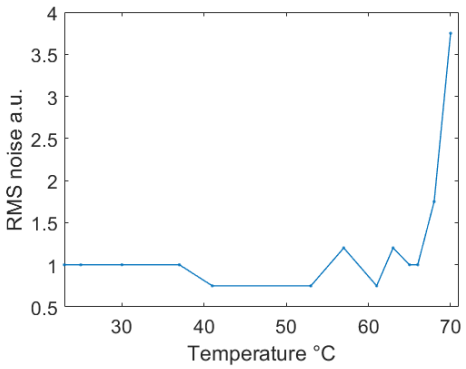

(a) Noise dependent on temperature

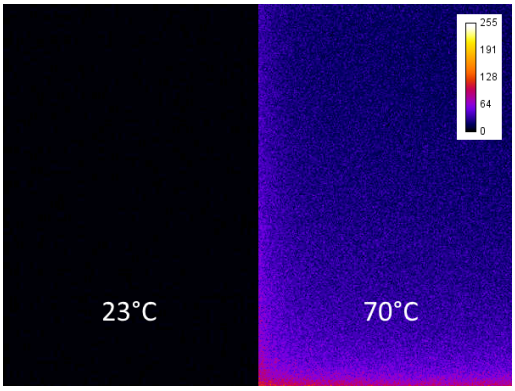

(b) Comparison of dark frames at 23° and 70° C captured with light tight shielding of the camera

Figure 4.2: Noise ratio at different temperatures of the CCD chip with test pictures at 23° C and 70° C. The measured noise value is obtained by the ratio of the standard deviation and the mean value and is normalized to the value at 23° C. Picture adapted from [47].

design with the special designed copper cooling body is shown in figure 4.5. The cooling bodies have been coated with copper sulfate to increase the heat radiation.

4.3 Electromagnetic pulse shielding of cameras in vacuum

Laser plasma experiments present a harsh environment for all electronic devices. Not only are the experiments done in vacuum, but also the laser plasma interaction generates a strong and broadband electromagnetic pulse (EMP) [60, 78]. The generation of this pulse has several origins: The first one is the target itself. When it gets ionized and the electrons are removed, a large return current from the surrounding matter generates an EMP pulse in a broad frequency range (kHz-THz). Meanwhile the accelerated particles hit the vacuum chamber wall and thus create a current in the electrical ground[5]. The EMP can lead to momentary malfunctions of electronic devices, e.g. cameras fail to capture an image during the shot or computers need to reboot. Even permanent failures of nearby PCs were reported. A simple approach to protect electronic devices in general and cameras in particular, is to put

[5]The chamber is normally grounded due to safety reasons

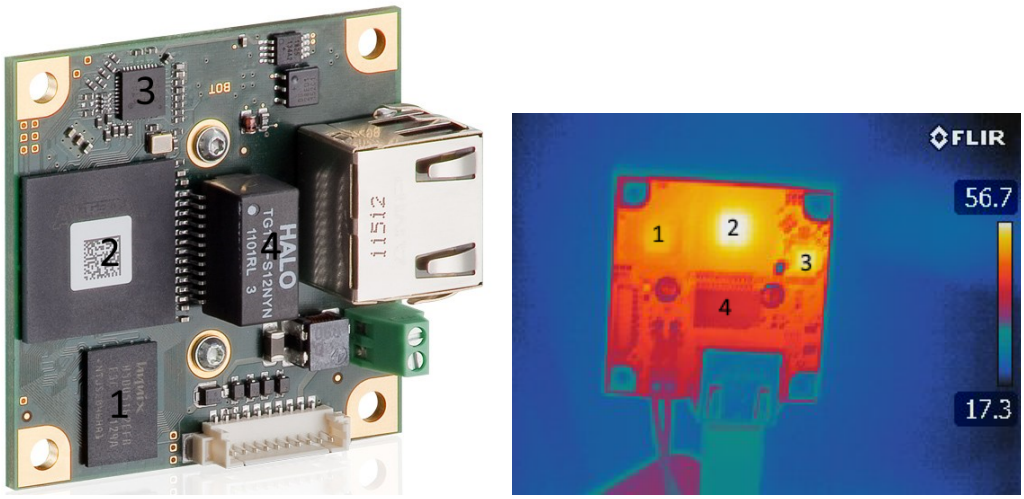

(a) Ueye camera (b) Ueye camera IR vision

Figure 4.3: IR image during operation compared with a photo of the camera. The numbers indicate the components on each picture. The IR image revealed the highest heat producing parts (1, 2 and 3), which needed direct contact to the cooling body. Left picture adapted from [38]

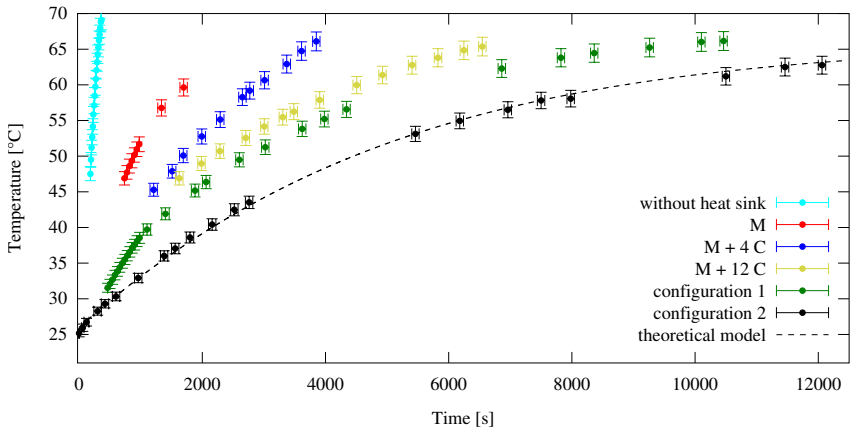

Figure 4.4: Temperature of the camera depending on the amount of cooling bodies. Picture taken from [47].

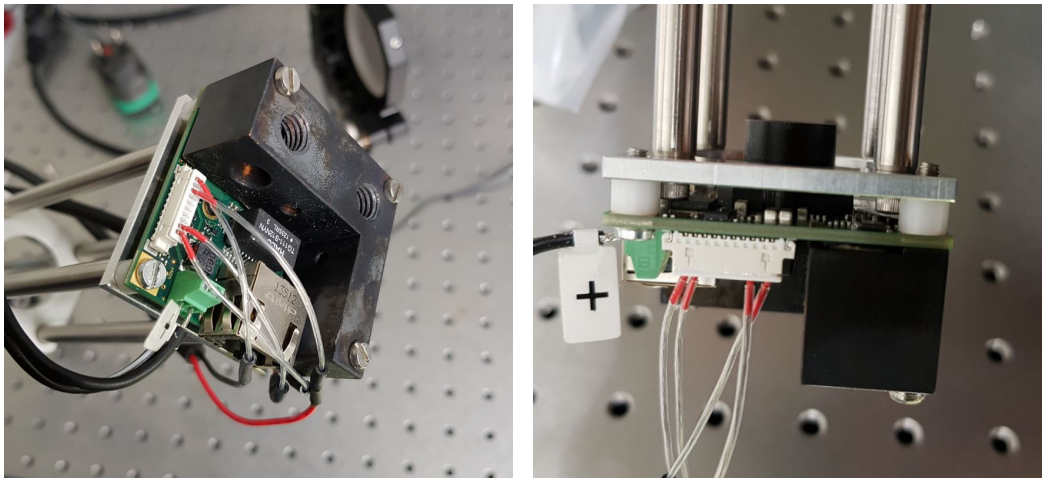

Figure 4.5: Camera with cooling body and adapter plate to fit into Thorlabs cage system.

them in a Faraday cage. The free hole size is determined by the highest frequencies and thus the shortest wavelengths generated. The spectrum of a typical laser plasma emp has its maximum in the Ghz range but ranges up to Thz radiation [78]. Thus the free gap size needs to be smaller than several 10s of µm.
For cameras the most challenging part is the optical window. To ensure a seamless Faraday cage these windows need to be electrically conductive. Windows with a coating of Indium-tin-oxide (ITO)[6] offer these properties and was the component of choice in our developments.
Figure 4.6 shows an example of a EMP safe camera housing with a board-level camera modified for vacuum usage placed inside. The housing was made of a commercially available aluminum container, which was designed for electronic shielding and offers a seamless enclosure. Modifications for a shielded cable feed through and a camera optical window had to be made. In figure 4.7 an example of the camera usage during a laser plasma interaction can be seen. In this figure the transmitted laser light trough a target was recorded[7].
The presented methods and developments support operation of cameras in vacuum and in harsh EMP environment. The experiences of these developments supported the realization of an advanced focus diagnostic solution,

[6]ITO is a transparent electrical conducting coating, often used as an electrode in solar cells.

[7]The measurement of the transmitted light allows a simple analysis of the target plasma density during laser pulse interaction. While overcritical targets ($n_{pl} > n_{cr}$) have zero transmission, undercritical ($n_{pl} < n_{cr}$) show transmission of the laser light

Figure 4.6: Passive cooled camera in an aluminum box for EMP protection. Note that also the cable needs to be shielded. Left picture shows the inside arrangement (earlier development stage) and right picture shows the final emp shielded camera with filter mount and integrated cable shielding into the camera housing. These cameras where successfully used in LEX photonics. Pictures taken from [105].

which is described in the next section.

4.4 Focus and target diagnostics in LION

Laser ion acceleration experiments work at ultra high intensities. In order to achieve such high intensities, a laser pulse is focused sharply with a reflective optic (off axis parabolic mirror, OAP). Due to the normally small F-numbers of such optics[8] the Rayleigh length is very small (few 10s µm) and the focus diameters are even smaller (few µm) and thus the region of high intensity is limited in all three dimensions. As an example of an F=3 OAP the focal spot size for a Gaussian beam is 2.6 µm FWHM with a Rayleigh length of 36.7 µm. The position of highest intensity (in three dimensions) is referred to as target chamber center (TCC). To define the TCC we need a device with resolution high enough to resolve 2.6 µm in lateral direction and 36.7 µm in laser propagation. A microscope with a numerical aperture (NA) equal or larger than 0.4[9] has proven to be the perfect tool for this task.
Traditionally a setup of such a focus diagnostic consisted of an infinity cor-

[8] In CALA we will used OAPs with F-numbers from 3 to 4.3
[9] e.g. the NIR version of the Mitutoyo long working distance 20x objective

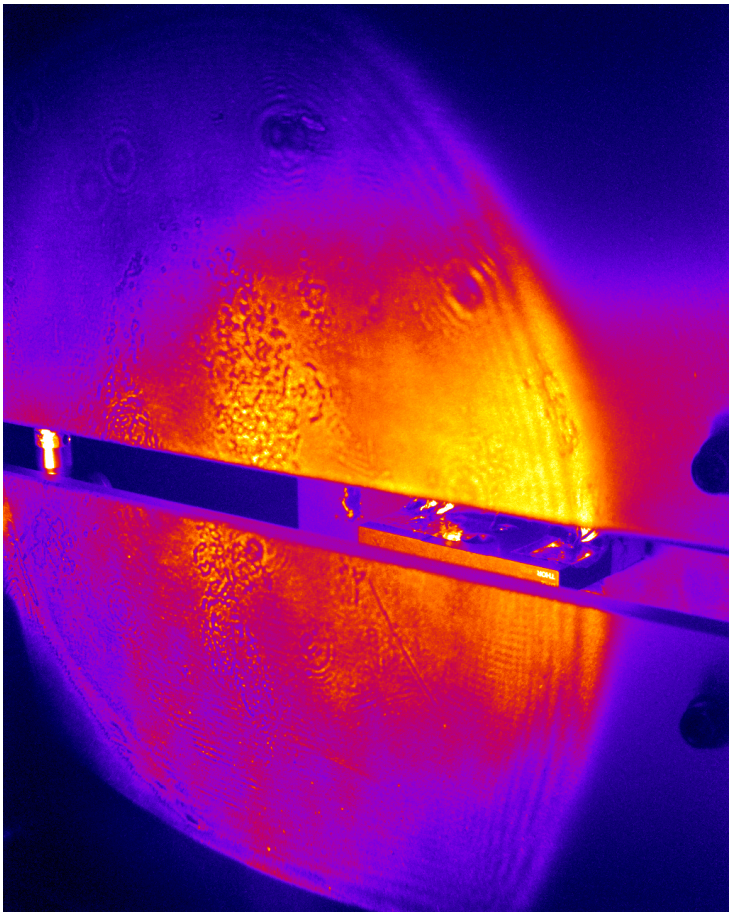

Figure 4.7: Exemplary picture of transmitted laser pulse through target on a scatter screen. Whether or not a target becomes transparent during interaction is dependent on target thickness and contrast of the laser pulse. During interaction, strong electromagnetic fields are hazardous for electronic devices, thus such pictures can only be recorded with well shielded CCD cameras.

rected long working distance microscope objective[10] situated in working distance to the TCC and normalized to the laser axis. This objective was placed on a linear stage in order to move it in and out of the beam direction. Mirrors were used to relay the beam after the objective out of the vacuum chamber. A tube lens finally created the magnified image on the ccd chip outside the vacuum system. The benefit of this setup was, that it was rather simple and one could use any camera. Further considerations for vacuum usage were not necessary. These setups are still common in many laser ion experiments [90]. However there are severe limitations and drawbacks of such a setup, which ultimately motivated the development of a vacuum compatible microscope in this thesis. Relaying the image out of the vacuum system requires an optical port, through which the image needs to be transported. This restricts the design of vacuum systems and also the optical port and the beam transport can take influence on the image quality[11]. Additionally the transport out of the vacuum system can take quite an optical path, which can result in vignetting. Vignetting is an effect which limits the field of view of an image. With the formula:

$$D_1 = 2f_1 \cdot NA \tag{4.1}$$

$$L_{max} = \frac{(D_2 - D_1) \cdot f_2}{D} \tag{4.2}$$

The maximum distance between the microscope objective and the tube lens in order to avoid vignetting can be estimated [69]. L_{max} represents the maximum distance between the two optics, f_2 is the focal length of the tube lens (in our case 200 mm) and f_1 is the focal length of the microscope objective (for a 20x magnification this is 10 mm). NA denotes the numerical aperture of the microscope objective (in our case 0.40). D is the image diameter and should be at least the diameter of the CCD chip (7.04 mm). D_1 and D_2 are the values of the diameter of the exit pupil of the microscope objective and the tube lens respectively. With a tube lens diameter of 50 mm[12] we get a maximum separation of objective and tube lens of about 1200 mm. This is a rather short value and shows, that a focus diagnostic with relay optics is only achievable at comparably small vacuum chambers.
To avoid vignetting and other unwanted effects, the camera has to be closer

[10] long working distance objectives are used to ensure on the one hand geometrical freedom close to the target and on the other hand to limit the fluence on the optic surface.

[11] Due to the stress on the vacuum vessel optical glass tends to bend slightly, which can take influence on the image quality. To avoid bending optical ports are made of thick glass pieces (several cm) which in contrast can lead to a spectral displacement if not traveled through orthogonality

[12] This is a common optic size and was used in most focus diagnostics with relay imaging

to the objective. The recent modifications of boardlevel scientific cameras for in vacuum usage (described in section 4.2) enabled a compact design of a fully vacuum immersed microscope. This approach, not only could circumvent the problems of a vacuum/air setup, but also allowed the compact design a more complex setup with additional measurement features for target analysis and enhanced laser diagnostics. The setup of the microscope is highly modal, thus every microscope can be configured to its purpose and with the use of Thorlabs standard components[13] a fast and cheap setup with the possibility to upgrade each microscope with additional features has been enabled and demonstrated.

4.5 Microscope setup

Figure 4.8 shows a schematic sketch of our standard microscope. In this setup we use an infinity corrected long working distance microscope objective[14]. The final image is created by a second lens, the so called tube lens. The distance between microscope objective and tube length is variable, which allows us to insert beamsplitters into the beampath. For the front side[15] target illumination, a LED is collimated by a lens with 30 mm focal length and projected onto the target surface. The LED wavelength is 780 nm to match the laser wavelength. With the collinear illumination, targets can be illuminated at 0 degree incidence. This is especially useful for nontransparent targets as for example metal foils. Two independent images are created with two tube lenses of different focal lengths. A 200 mm lens (L1) creates an image on camera 1 in the natural magnification of the microscope objective[16] (20x). Images in this camera are referred to in the following text as high mag images. The second lens (L2) features a shorter focal length (30 mm), and thus the image created on camera 2 has a lower magnification (3x), which on the other hand provides an increased field of view. Images in this camera are referred to as low mag for simplicity in the following text. The field of view of the high mag with a 1/1.8 inch class image sensor is 340 µm x 270 µm, whereas the low mag features a field of view of 2200 µm x 1800 µm. The two cameras are independent from another, which means, that we can change camera settings like illumination time and gain independently. With formula

[13] They were still modified for vacuum use. For example we removed the black anodization layer, which can store a large amount of adsorbed water and exchanged all greases with vacuum compatible substitutions

[14] Mitutoyo M Plan APO NIR 20x with NA 0.40

[15] front side in this context means the target surface facing the microscope

[16] The microscope objective we use here was optimized for a $f = 200$ mm tube lens

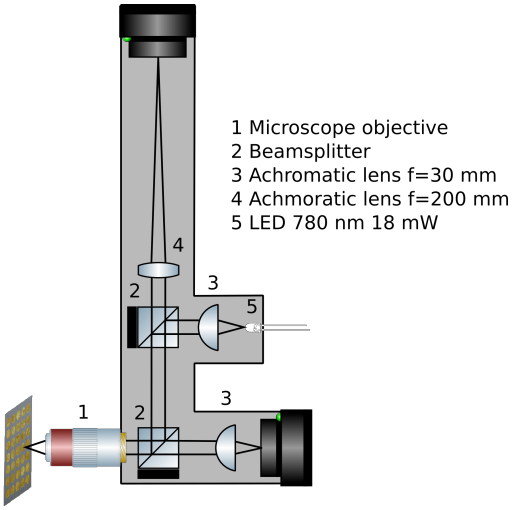

Figure 4.8: Setup of a vacuum immersed microscope with two simultaneous magnifications.

4.2 we estimate a maximum distance of the microscope objective and the tube lens for the 30 mm lens of about 73 mm before vignetting occurs, which emphasizes, that the higher field of view is only possible with a compact, in vacuum design of the microscope. The low mag has proven to be very useful for target alignment. Also laser alignment is greatly simplified by the large field of view, which allows significant tip/tilt changes of the OAP without loosing sight of the focus, due to the limited field of view of a typical high-mag microscope. In figure 4.9 an example of the two magnifications can be seen, when observing a typical target holder with holes of 550 µm diameter supporting a 100 nm freestanding plastic foil. While in the low mag the entire hole is visible, the field of view of the high mag is smaller than the diameter of the hole, which would make positioning relative to the hole borders, with the field of view of high mag alone, cumbersome. The low mag greatly simplifies orientation. It also played a key role in centering each target holder hole during the target positioning routine in the automized referencing program of the nanofoil target positioning system (n-FTPS) [27].

4.6 Target positioning and characterization

In section 2.2.4 we demonstrated the importance of a target positioning system for high repetition rate laser ion acceleration experiments. In such positioning systems, the deviation from the ideal target position of each target, is measured beforehand and compensated, when moved to the interaction

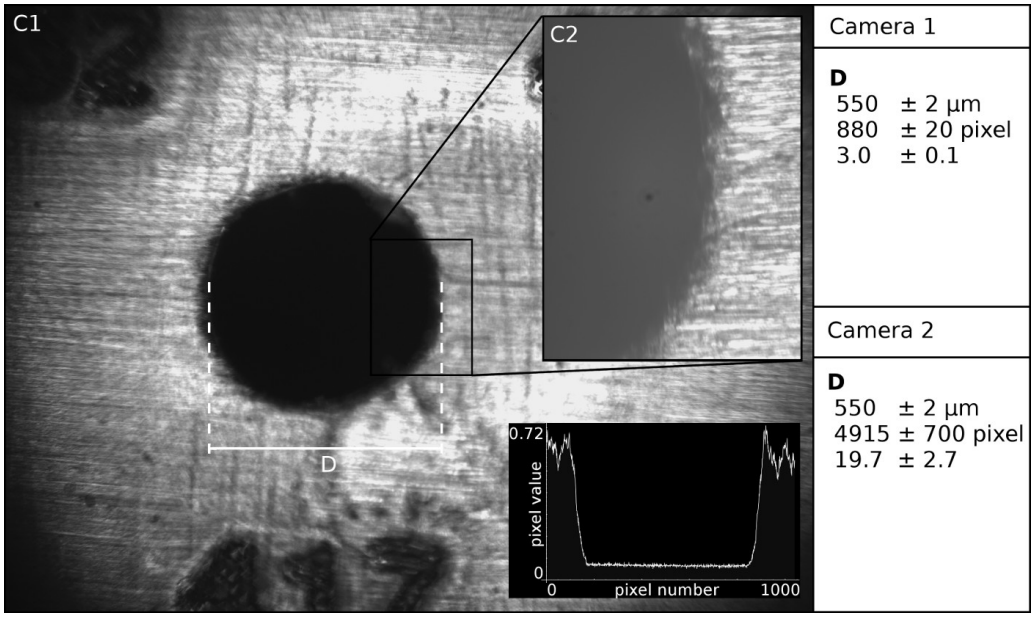

Figure 4.9: Camera images of the two simultaneous magnifications of a typical target holder for laser ion acceleration experiments. C1 shows the image in the 3 times magnification and C2 shows the image of the 20 times magnification camera. For a field of view comparison, the field of view of C2 is showed as a rectangle in C1. The lineout indicates the number of pixels, which are necessary for a display of the whole target hole diameter. Picture taken from [47].

point of the laser. In order to measure the position-deviation, a chromatic optical distance sensor [23] is used. A drawback of this kind of measurement is, that two separate devices are used for the longitudinal (z, laser propagation direction) and lateral (x,y) measurements of target position with respect to the TCC. The distance sensor must be carefully referenced to the TCC. Both devices need to be moved in perfect relative coordinates with respect to each other, switching back and forth between microscope and distance sensor measurements. This procedure is of course prone to misalignment and the relative coordinates needs to be checked regularly. The compact microscope setup can in principle accommodate such a distance sensor, but also can draw from additional features that go much beyond the chromatic distance measurement capability.

4.6.1 Whitelight interference microscopy

Optical interferometry is a precise and flexible tool for the measurement of target position and target diagnostics. Interference is an effect caused by the wave properties of light. The use of interferometry for distance measurements, topographic mapping and 3D imaging of systems is a widely used technique in for example mechanical engineering [16], biology [26], medicine [109] and microelectronics [9]. Interference microscopy techniques are able to produce precise measurements with sub-micrometer resolution, even in materials with complex structures and different refractive indices, such as the targets used for laser acceleration. In contrast to monochromatic interference, where only spacial information about the wavefront is measured, the whitelight interference can detect spacial information of the wavefront (time domain optical coherence tomography, TDOCT) as well as spectral information of the measured waveform (Fourier domain optical coherence tomography, FDOCT).
The following sections summarize the results of the master thesis of Victor G. Gisbert, who was supervised by the author.

4.6.2 Theoretical background

Interference occurs if two optical waves are super positioned for example on the detector in a Michelson interferometer [63] (compare figure 4.10). Interference experiments are usually done with coherent light sources (lasers), which offer a large coherence length. Whitelight interferometry however uses a spectral broad light source (for example a LED), which offers an extremely short coherence length. If we assume a light source with Gaussian spectral

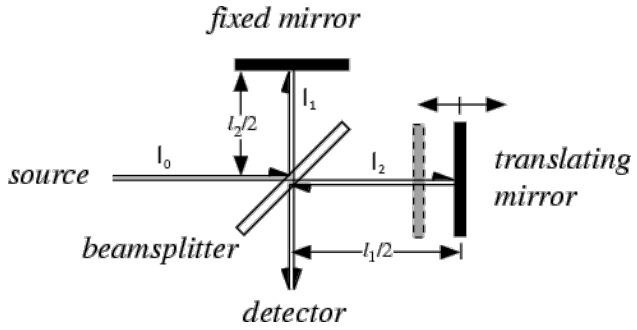

Figure 4.10: Typical Michelson interferometer setup. One mirror can be translated to introduce a optical path difference (OPD). Picture modified from [80].

intensity distribution

$$I(\nu) = I_0 \cdot \exp\left(-\left(\frac{\nu - \nu_0}{\Delta\nu}\right)^2\right) \tag{4.3}$$

we can derive the coherence length by the Fourier transformation of the spectral intensity distribution. Thus we get

$$L_c = \frac{c}{\pi \Delta\nu n} = \frac{2\ln(2)}{\pi n}\frac{\lambda_0^2}{\Delta\lambda}$$

for the coherence length L_c [1], which is inverse proportional to the spectral broadness $\Delta\lambda$. λ_0 denotes the center wavelength of the light source and n the refractive index. For a LED light source with assumed Gaussian spectrum with center wavelength $\lambda_0 = 780$ nm and a FWHM of $\Delta\lambda = 30$ nm the coherence length is $L_c \approx 9$ µm.
The total intensity on the detector depending on the optical path difference is [1]:

$$I(x) = I_0\left(1 + \cos\left(4\pi\frac{x}{\lambda_0}\right)\exp\left(-4\left(\frac{x}{L_c}\right)^2\right)\right) \tag{4.4}$$

In figure 4.11 the intensity depending on the OPD is demonstrated by the example of the Gaussian light source of the LED. By using a low coherence source, the position of the target surface can be precisely determined by moving the reference mirror and measuring the resulting phase and modulated amplitude of the intensity.

Because of the spectral broadness of the light source, we can also analyze

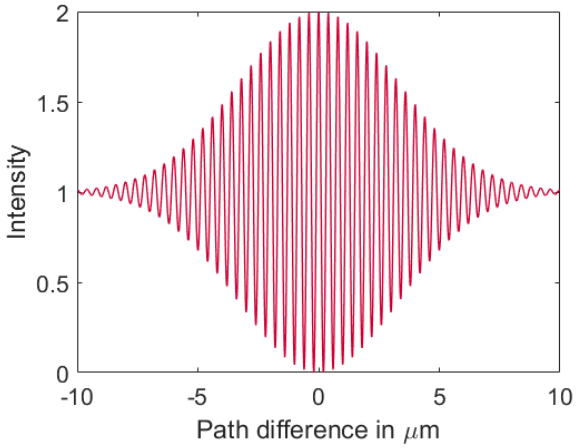

Figure 4.11: Total intensity depending on the OPD using a Gaussian light source with center wavelength 780 nm and FWHM of 30 nm.

the intensity with respect of the wavelength. The Intensity dependent on the wavelength and OPD is given by:

$$I_T(x) = I_0 \left(1 - v(x) \cos\left(4\pi \frac{x - x_0}{\lambda}\right)\right) \tag{4.5}$$

Where $I_0 = I_1 + I_2$ is the total intensity of the reflected light. We introduce $v = 2\sqrt{(I_1 \cdot I_2)}/(I_1 + I_2)$ as the fringe visibility. The fringe visibility is dependent on the coherence length of the light source and is proportional to:

$$v(x) \propto \exp\left(\left(-\frac{x}{L_c}\right)^2\right) \tag{4.6}$$

In figure 4.12 an example of a modulation by a OPD of 20 and 100 µm is shown. It might be surprising, that a modulation of the intensity is still visible, while the OPD is larger than the coherence length of the light source. However due to the spectral resolution of the spectrometer, a reduction of the spectral width is achieved, which increases the effective coherence length. A comparison of the theoretical calculations with the measured values of the same light source and the same displacements show good agreement. In conclusion, the spectral interference serves well to initially position the target in a coarse-grained fashion due to the increased coherence length obtained by the reduction of effective spectral width. Thereafter, the fine adjustment resolution can benefit from the spectrally integrated image which features a very short coherence length.

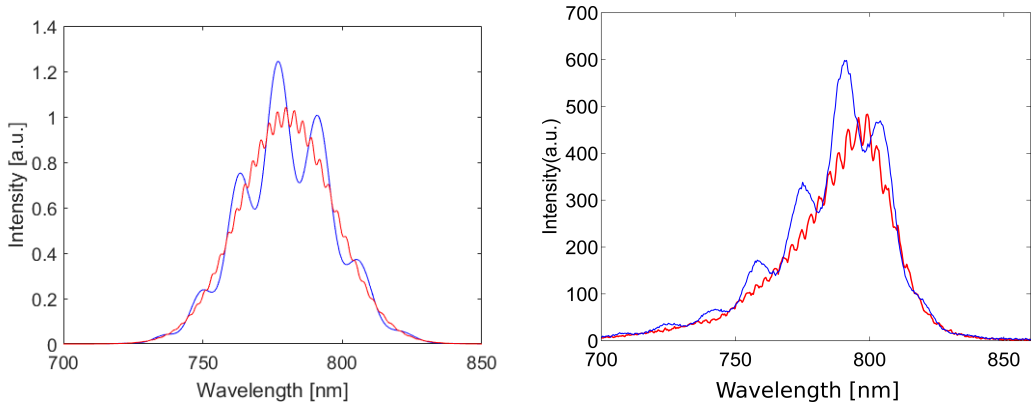

(a) Theoretical spectrum of WLI (b) Measured spectrum of WLI

Figure 4.12: Comparison of measured and theoretical interference spectrum for two mirror positions with different OPD, -20 µm (blue) and +100 µm (red). Note the change of frequency and contrast in the oscillation with larger displacement. The coherence length is much larger in the spectrometer, because the effective spectral width is much smaller (in the order of the resolution). Right picture taken from [30].

4.6.3 Experimental realization of WLI and first tests

In order to integrate whitelight interferometry to the existing setup of the microscope, the optical design had to be slightly modified and extended. A reference mirror had to be introduced, as well as a compensator for accumulated phase difference in the two interferometer arms. In figure 4.14 the setup of a Linnik type whitelight Michelson interferometer is shown. With this setup time domain optical coherence tomography (TD-OCT), where the spatially resolved intensity is investigated (detection with a camera), as well as Fourier domain optical coherence tomography (FD-OCT), where the spectrally resolved intensity (detection with an optical spectrometer) can be realized simultaneously.

Fourier domain optical coherence tomography

Fourier domain optical coherence tomography (FD-OCT) is useful, if the displacement of one interferometer arm (in our case the target from focal position or tcc) has to be measured. For example, if we want to measure the displacement of each target in the target wheel. In order to get the displacement of a target from focal position, targets are positioned into tcc position

with mechanical precision[17]. Then the modulated spectrum is measured and analyzed[18]. In figure 4.12 an example of the modulation of the spectrum due to displacement is given. The fringe contrast with actual targets instead of a mirror however is reduced due to the lower reflectivity and the non perfect surface. The range of application of this technique has been tested and a maximum of displacement of ±100 µm can be achieved with the led spectrum. In figure 4.13 an example of a target translation and the measured displacement from zero position can be seen. In this measurement a 100 nm foil has been moved with a calibrated micrometer stage and the modulation in the spectrum was measured and analyzed. The results where plotted versus the expected position. As can be seen, they show good agreement and also the range of this technique can be seen. The range is limited by the fringe visibility and thus the possibility to extract the OPD. Polystyrene and Formvar targets with thicknesses of 100 nm, 85 nm and 35 nm have been tested successfully with this method, with no influence of the used target material detectable. The major difference between these targets is the reflectivity, and in consequence the signal intensity detected in the spectrometer. Very thin targets i.e. a 35 nm Polystyrene foils have a total reflectivity of less than 4% and at this thickness [46]. However the interference produced by the target in the spectrometer can still be detected and measured.

Time domain optical coherence tomography

Time domain optical coherence tomography (TD-OCT) is the most commonly used interference microscopy method. As seen in figure 4.11 changing the position of the sample over the coherence length will produce a oscillatory behavior of the intensity. By this method a very precise positioning is possible. The precision is only dependent on the spectrum of the employed light source. A positioning with an accuracy of the order of the center wavelength is possible, exceeding the native z-resolution of the microscope objective:

$$R = 0.61\frac{\lambda_0}{\mathrm{NA}} = 1.2\ \mu\mathrm{m},$$

where a center wavelength $\lambda_0 = 780$ nm and a numerical aperture NA $= 0.4$ was assumed. Using the high z-resolution, 3D mapping of the surface of a sample can be measured in a z-scan with the microscope. While inherently

[17]The targetwheel was designed to have a mechanical deviation of each target holder smaller than 100 µm. However there is also an effect of the target holder itself, as targets tend to have different positions in the holes.

[18]Details on the different analysis methods can be found in the master thesis of Victor Garcia [30]

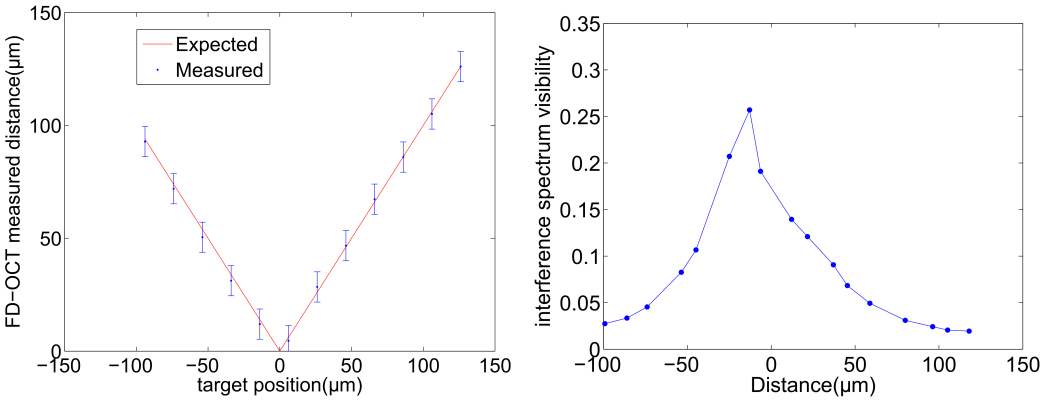

(a) Measurement of displacement (b) Fringe visibility

Figure 4.13: Left comparison of the measured distances and the micrometer stage position. The line corresponds to the expected measurement and the dots to the measured position. Error-bars include the error produced in FD-OCT and the systematic error of the micrometer stage. Right visibility of the interference in the spectrum. Note that the maximum is 15 µm away from zero position. Pictures taken from [30].

the z-resolution is enhanced, this technique also gives advantages for detecting targets in focus. Targets are thin fragile films and during production, transport and setup in the final experiment, unavoidable changes and losses occur. With improving target production techniques [88] defects and stains are reduced, which improves the overall quality of the targets. However a perfectly clean surface is very difficult to detect in bright field microscopy, thus increases the difficulty to detect the position of a target, or even the existence of it at the expected position. Due to the fact, that WLI is caused by the interference with the reflected wavefront of the target surface, TD-OCT does not suffer from these problems and is able to detect perfectly clean surfaces. In figure 4.15 a comparison of bright field images and WLI images are presented, illustrating the advantages in target detection. Especially for the case of a 35 nm clean target, it is almost impossible to detect the foil in focus position. In figure 4.16 images of deformed and broken targets are compared with bright field- and WLI-microscopy. While the defects are also visible in the bright field images, the TD-OCT images show more informations about the nature of the defects. While this might not be the most interesting part, it is worth to note, that with this technique an automatized quality control of the targets can be achieved. The fringes can be analyzed by software, and for example, if a target shows a non flat surface or are tilted by a too high angle, it can be attributed to the target properties. The influence of stained

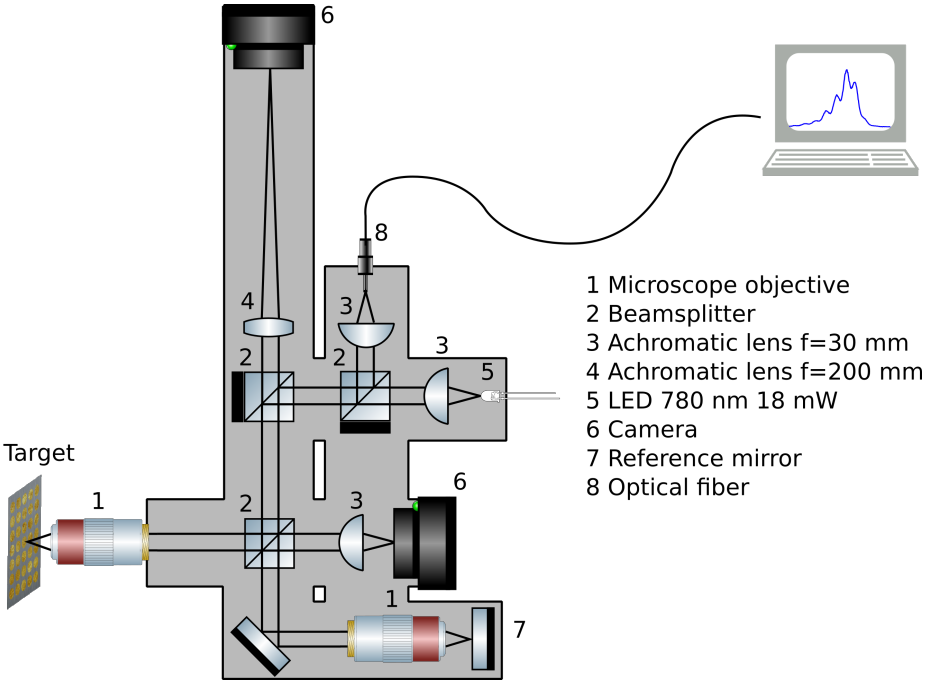

Figure 4.14: Setup of microscope with WLI interference.

targets to the laser ion acceleration can thus be minimized by the advanced quality control.

Reconstruction of surfaces topography

With the TD-OCT technique it is also possible to reconstruct the topography of a three dimensional shape. In this technique the sample is moved in discrete steps in z dimension and images of the surface are recorded. The maximum of the fringe contrast represents the area of the sample, which is in focus. By combination of the single images and the extracted position data of each frame, it is possible to reconstruct a topography of the surface [17]. Figure 4.17 shows an example of this technique by profiling a deformed target. The target shows a complex structure in the interference image. Applications for this technique in laser ion acceleration are shaped targets, since production, transport and pump down introduces stress to the target. A final check in-vacuum before shooting it, allows verification of target integrity.

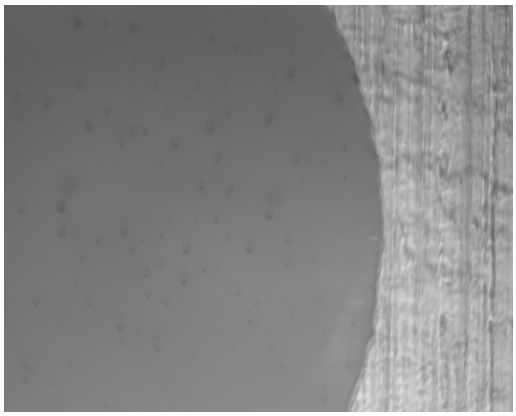

(a) Bright field image of 100 nm formvar target.

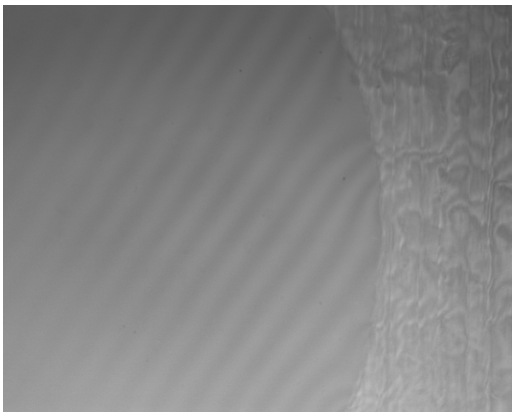

(b) WLI image of 100 nm target. Note that the target holder also shows interference, indicating a non flat surface.

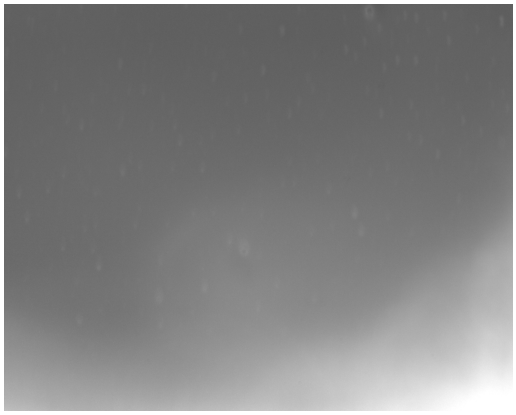

(c) Bright field image of 35 nm formvar target. The contrast is very low, which makes it difficult to position the target in focus.

(d) WLI image of 35 nm target. The contrast in focal position is superior compared to the bright field image, which makes it easy to position this target in focal position.

Figure 4.15: Comparison of bright field images with WLI images at the example of thin formvar foils. The contrast of brightfield images decreases significantly, if the target thickness is lower than 100 nm. Pictures taken from [30].

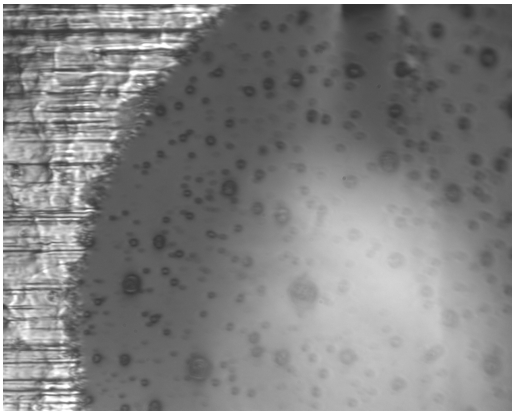

(a) Deformed target bright field

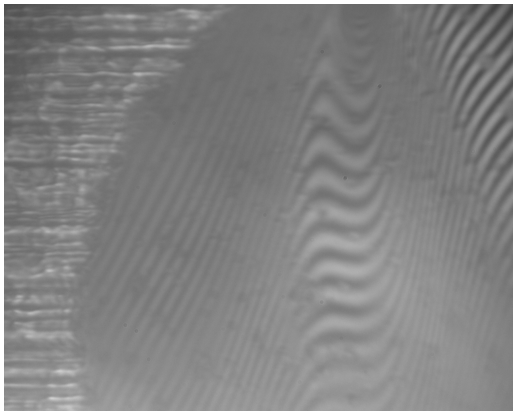

(b) Deformed target WLI

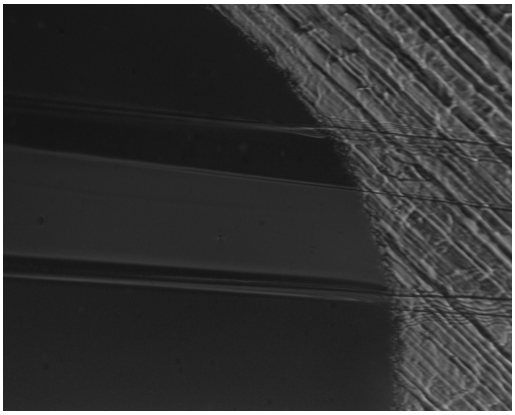

(c) Folded target bright field

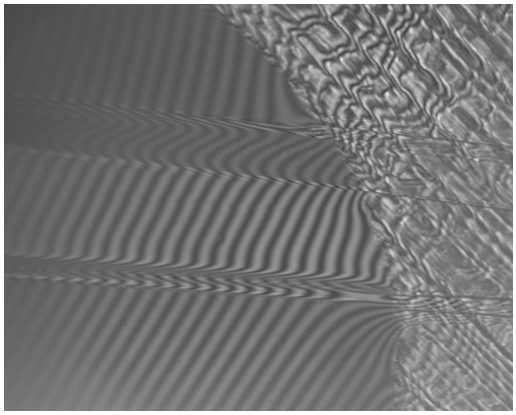

(d) Folded target WLI

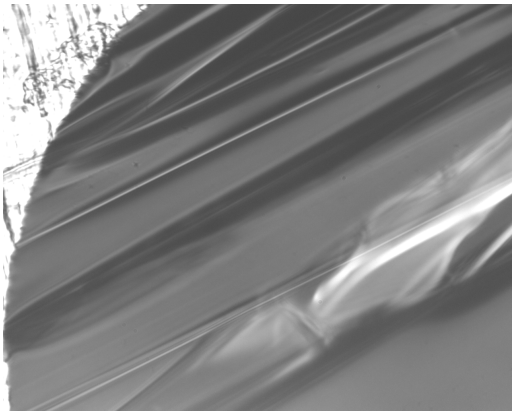

(e) Broken target bright field

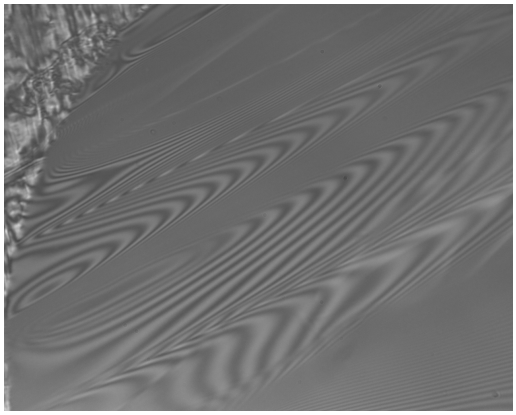

(f) Broken target WLI

Figure 4.16: Comparison of deformed and broken targets seen with bright field microscopy and WLI. The contrast to detect defects in targets is higher for WLI. Also this technique gives access to automatic characterization of surface quality. Pictures taken from [30].

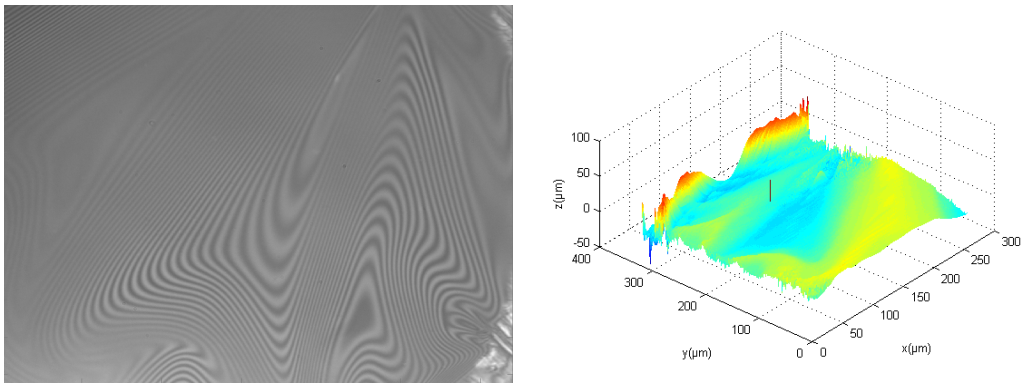

(a) TD-OCT of a target

(b) Calculated topography

Figure 4.17: Illustrative example of a 3D mapping with a target with non flat surface. The topography was calculated with several pictures of a z scan. Left is one exemplary picture of this scan. Right shows the resulting topography. This technique can be used for 3D analysis of shaped targets with non flat surfaces and testing, if they survived the pumping process. Pictures taken from [30].

4.6.4 Spectral reflectance measurements

In addition to the ability of measuring target position and surface topography, the inclusion of a spectrometer in the system adds the possibility to measure the target thickness by analysis of the reflectivity of each wavelength [46]. Similar to the considerations in section 4.6.2 a transparent target can be seen as two reflecting surfaces with a displacement of its thickness. Thus the reflection from the rear side of the target will interfere with the reflection of the front side of the target. The reflected waveform from an interface of two media of different refractive indices will acquire a phase change of π if the refractive index n_1 of the first medium is smaller than that of the following medium n_2. Thus the reflection from the front part of the target will acquire a phase change of π, while the reflection on the rear surface will acquire a phase proportional to the optical path length. If the optical path length divided by the wavelength is multiple of 2π, destructive interference between the rear and the front surface will be observed, leading to the following equation for the reflectivity:

$$R \propto \left(1 + C \cdot \cos\left(\frac{4\pi n x}{\lambda} - \pi\right)\right)$$

Where R is the reflectivity, C the contrast of the reflection, n the refractive index, x the thickness and λ the wavelength. In this equation normal

incidence was considered and thus angle effects have been neglected. The reflectivity of an interface of two refractive indices is described by the Fresnel equations [34]:

$$R = \frac{(n-1)^2}{(n+1)^2}$$

By considering that the transmitted light of the front surface $T = 1 - R$ is only reflected once by the rear surface (neglecting multiple reflections inside the target as well as absorption effects), we can write the equation for the reflectivity of a thin transparent film as [46]:

$$R_{Target}(\lambda) = R\left(1 + (1-R)^2 - 2(1-R)\cos\left(\frac{4\pi nx}{\lambda}\right)\right) \tag{4.7}$$

The shape of the function 4.7 for different thicknesses of a freestanding formvar foil ($n = 1.445$) is shown in figure 4.18, showing that thicknesses of 50 nm and more are easily detectable with an optical spectrum. Thinner films (20 nm and lower) are more difficult to measure and would require a broader spectrum. With this technique and an optical spectrum of 400-1100 nm, which is supported by the optics in the microscope, we are able to measure reliably thin transparent films of thicknesses from 50 nm and thicker.

Thickness determination of thin formvar films

To measure the thickness of a freestanding transparent film, the reflected spectrum of the thin film is measured. As a calibration step, the reflected light of a silver mirror with known spectral reflectivity was used to normalize the spectral response of the used optics in the microscope. The used light source in this experiment was a broad band halogen lamp light source[19]. Figure 4.19 shows the result of the spectral reflectivity of a 280 nm thick formvar foil and the corresponding fit of the model 4.7 yielding also 280 nm. In figure 4.20 a comparison of a commercial spectral reflectometer[20], which was used for thickness determination for plastic targets in the LION experiment LEX-photonics with the thickness determination of the presented microscope. The table shows a good agreement for a large range of target thicknesses, which where commonly used for LION experiments in LEX-photonics.

[19]DH-2000-Bal Ocean Optics
[20]Sensofar PluNeox

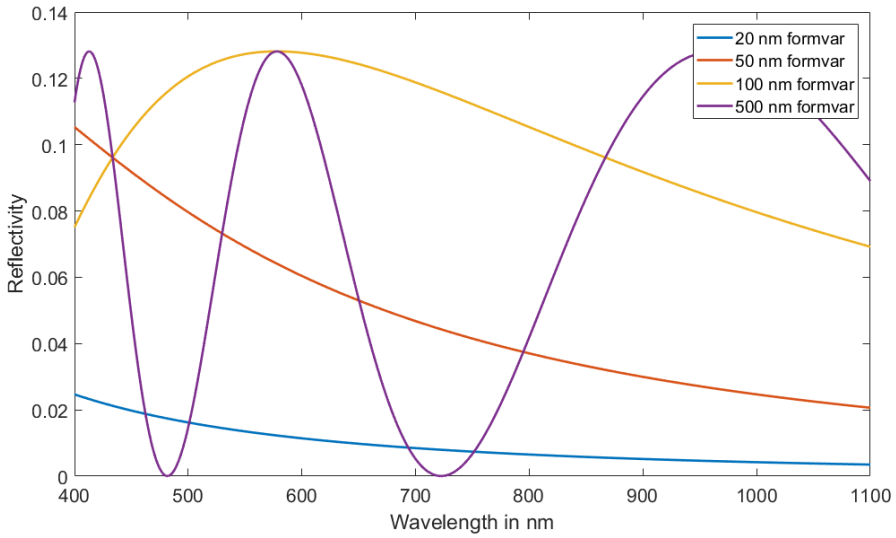

Figure 4.18: Reflectivity of various thin formvar foils dependent on the wavelength. 400-1100 nm is the typical accessible wavelength range for spectrometer and optics.

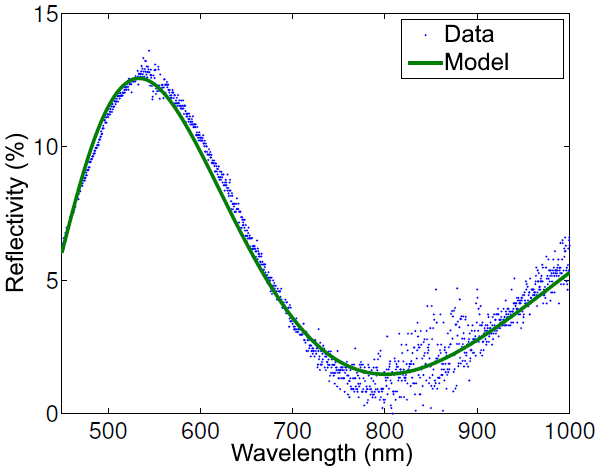

Figure 4.19: Measured reflectivity of a 280 nm formvar target with the microscope by using the spectrometer. The line corresponds to a fit of the data points with the formula 4.7. The noise in the infrared region is due to the low intensity of the light source in this region. Picture taken from [30].

Online [nm]	137	215	303	364	432	637	800	922
Offline [nm]	134	237	299	356	435	634	876	907
Difference [%]	2.2	9.7	1.3	2.2	0.7	0.5	9.1	1.5

Figure 4.20: Measured target foil thicknesses with the microscope (Online) compared to a commercial device which uses the same technique (Offline). Values taken from [35]. Note that the big variations in 800 nm and 922 nm can be attributed to an inhomogeneity of the production technique, which is worse for thicker films, than for thinner films.

4.7 Laser characterization

Besides target positioning and analysis, the characterization of the laser focal spot is the second main task of the microscope in laser ion acceleration experiments. On the one hand, a precise measurement of the focus position is necessary and on the other hand a full characterization of its spatial intensity distribution is necessary for later evaluation and interpretation of results obtained in laser plasma experiments. The microscope is used for optimal alignment of the laser focusing optic (off axis parabolic mirror) where slight misalignments can lead to drastic reductions of the laser intensity by introduction of aberrations. With a perfectly aligned focusing optic, the limiting factor of diffraction limited focusing are deviations in the wavefront, which arise from imperfect optical surfaces. To address the wavefront aberrations we demonstrate measurements of the wavefront with a Shack Hartman sensor integrated in the microscope setup, which paves the way for an optimization of the focal point with adaptive optics.
Also, an example of an extended dynamic range focal spot imaging is shown, which reveals the optimization potential of the laser and gives important insights for later interpretation of data, as it gives a more realistic impression of the experimentally achieved peak laser intensities. The following sections summarize the results of the master thesis of Sebastian Herr [35], who was supervised by the author.

4.7.1 Wavefront measurement

For a diffraction limited focal spot a flat wavefront of the laser in the near field is necessary. During the generation of the laser pulse, amplification and transport distortions are introduced, which in general lead to a non-flat wavefront. For this reason, adaptive optics are commonly used to compensate these distortions in high power laser systems [25, 3]. Besides the improvement

of the final laser focus in the experiment, one goal is also to limit the fluence[21] on the diffraction gratings in the compressor, as the gratings in a high power laser system are usually the most fragile components. In ATLAS300 the compensation of the wavefront was done before compressor, with this second goal in mind, i.e., to reduce local maxima in the intensity distribution at the compressor gratings. However, distortions from the gratings itself and the mirrors of the laser beam delivery remain uncompensated. In CALA for ATLAS3000, an additional vacuum compatible deformable mirror will be introduced into the laser beam delivery, which allows for an optimization of the wavefront after the temporal pulse compression[22]. This deformable mirror however needs an input signal for the optimization process. This is realized with a wavefront sensor. There are different working principles of wavefront sensors, certainly the most common one is the Shack-Hartmann sensor [89]. The principle of a Shack-Hartmann sensor is depicted in figure 4.21. Shack-Hartmann sensors consist of a micro lens array, which is placed in front of an image sensor at the distance of the focal length of the individual lenses. Each micro lens focuses a part of the wavefront onto the image sensor. Local tilt in the wavefront will result in an distortion from the center point of an ideal focus. By measurement of the distortions, the local tilt of the wavefront can be calculated.
Wavefront correction with the deformable mirror using the wavefront sensor as an input signal is usually realized with a feedback loop. In figure 4.22 the principle is illustrated. The uncompensated laser is sent onto the wavefront sensor to measure the first order distortion. Corrections are then applied and the remaining distortions are measured again. This process is repeated until a desired accuracy of the wavefront is reached.

Integration into the microscope

To include all distortions to the wavefront, ideally the wavefront has to be measured at TCC. For this reason we integrated the wavefront sensor into the focus diagnostic microscope. This has several benefits: First, the microscope offers a telescoping which is needed for the wavefront sensor to operate. Second, less space is required than for an integration of an external sensor. Third we can measure the final focal spot simultaneously, while optimizing the wavefront. Fourth, the design and implementation requires to have a

[21] The fluence on an optic can be higher than the average fluence of a flat top beam, if the wavefront is non-uniform. Local tilts in the wavefront can lead to field increase and thus to locally higher fluence.

[22] Which means, that the distortion introduced by the gratings in the compressor and the beamline mirrors before the DFM can be compensated

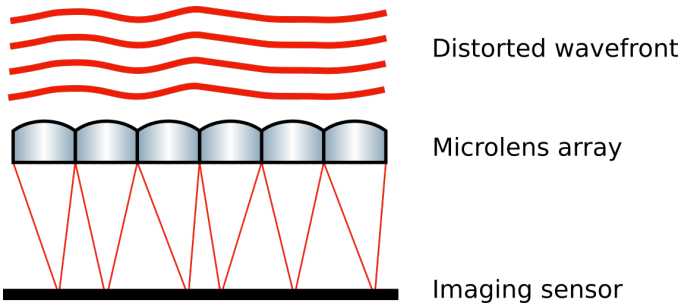

Figure 4.21: Working principle of a Shack-Hartmann sensor. The wavefront is separated by the microlenses and focused onto an imaging sensor. Local tilt results in a lateral deviation of the focal spot from center position.

WFS in every experimental chamber, which offers a huge cost advantage to commercial systems.
For integration into the microscope, a beamsplitter was added between the optical path of the high mag and the illumination port (compare figure 4.23). This is a good compromise between compactness and influence of non perfect optical elements inside the microscope to the wavefront. For calibration a nearly diffraction limited laser beam[23] was focused with an identical microscope objective and recollimated with the microscope.

Wavefront reconstruction

For a wavefront reconstruction with a Shack-Hartmann sensor, the slope of the wavefront of each lenslet is measured calculating the distortion of the focal spot from the centroid position times the distance between 2 lenslets [66]:

$$\delta z = d \cdot \Theta_{x/y,n} = d \cdot \frac{\delta x_n / \delta y_n}{f} \tag{4.8}$$

With the slope values of each lenslet we can define a two dimensional slope grid of the wavefront. Usually this grid is now fitted with a set of zernike polynomials for a smooth reconstruction of the wavefront. There are several algorithms available for wavefront retrieval (i.e. modal or zonal reconstruction [93]), however a detailed description is beyond the scope of this thesis. Instead we will focus on the theoretical achievable resolution.

[23] The laser beam of a Zygo interferometer for characterization of large optics like mirrors was used

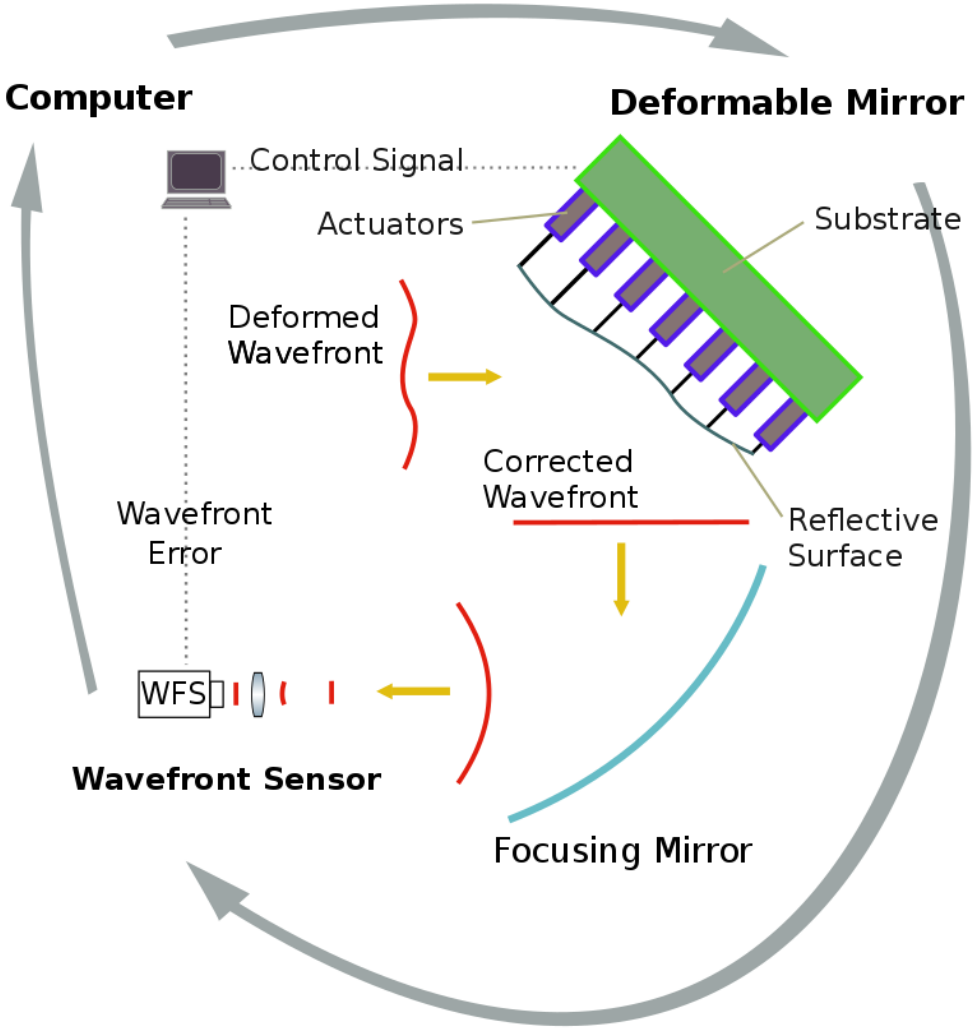

Figure 4.22: Principle of a feedback loop with an adaptive mirror and a wavefront sensor. Picture taken from [35].

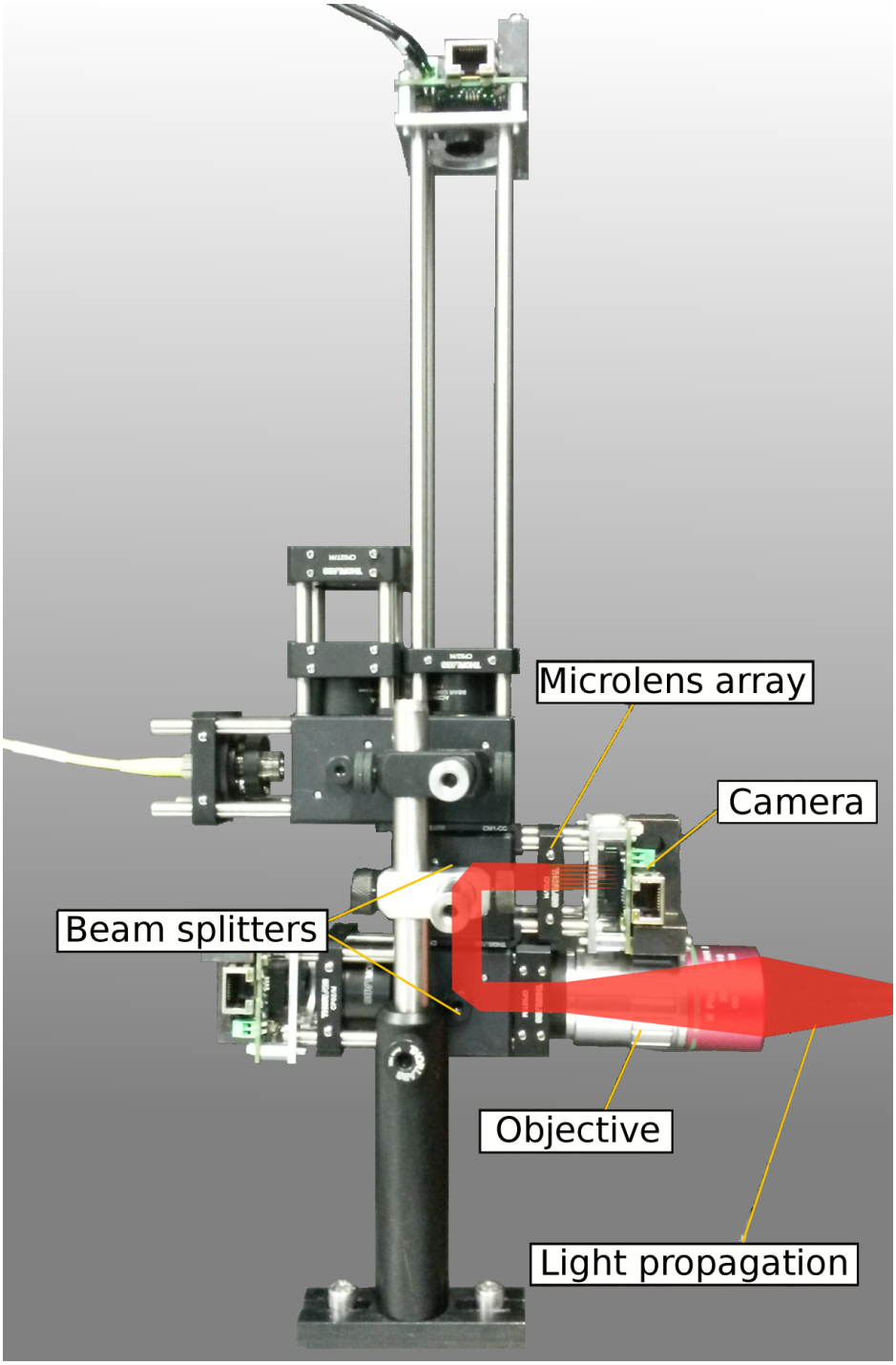

Figure 4.23: Integration of the wavefront sensor into the microscope. Picture adapted from [35].

Resolution of the wavefront sensor

The resolution of a Shack-Hartmann WFS is determined by the used microlens array. The lateral resolution (sampling rate of the wavefront) is defined by the number of lenslets (and the fill factor) covert by the full aperture. Thus the maximum sampling rate for the WFS used in this thesis is 33 over a full diameter of 10 mm maximum diameter, which results in a lateral resolution of 300 µm.
The resolution of the wavefront local slope is defined by the focal length of the lenslet and the accuracy of the displacement measurement (4.8). Due to the fact, that focal spots created by the lenslets are larger than the pixels of the camera chip, a subsampling of each focal spot can be achieved. Thus the position of each focal spot can be calculated by determination of the centroid by a median function:

$$X_c = \frac{\sum_i x_i \cdot p_i}{\sum_i p_i} \tag{4.9}$$

Where x_i is the position of ith pixel and p_i is the pixelvalue. X_c represents a numerical retrieved centroid coordinate with a simple linear weighting. The smallest detectable deviation is an increase or decrease of 1 in a single pixel value:

$$\begin{aligned}\Delta X_c &= X_{c1} - X_{c2} \\ &= \frac{\sum_i x_i \cdot p_i}{\sum_i p_i} - \frac{\sum_i x_i \cdot p_i + x_p \cdot 1}{\sum_i p_i + 1}\end{aligned}$$

where x_p is the pixel coordinate that undergoes the value change. The resolution is now dependent on the dynamic range of the used camera chip. We estimate the maximum p as 255 which is the case for a 8-bit camera chip. For a full range Gaussian intensity distribution with a FWHM of 60 µm we get an integrated intensity of 5540 and a moment of 65535. With a change in p next to the maximum, we get minimal detectable distance of $\Delta X_c = 3.1 \cdot 10^{-3} \approx 16.4$ nm. Using equation 4.8 we get a resolution of:

$$\delta z_{min} = d \cdot \Theta_{min} = 300\ \mu\text{m} \cdot 0.8 \cdot 10^{-6} \approx 0.24\ \text{nm}$$

the minimal detectable phase is then:

$$\Delta\phi_{min} = \frac{2\pi}{\lambda}\delta z_{min} \approx \frac{\lambda_c}{3300}$$

Where λ_c is the dimensionless unit of the wavelength. The true resolution however is dependent on the centroid algorithm and also the dynamic range

of the camera. Here we assumed a 8 bit dynamic range with a signal to noise ratio better than 1:256. This is true for most scientific cameras and also for the use of the camera used in this thesis[24]. Operation of the camera with 10 bit pixel depth can increase the resolution.
The wavefront measured with the microscope is telescoped, which needs to be taken into account, when considering the final resolution on the full aperture wavefront. In CALA we anticipate a F 2.5 OAP at a beam diameter of 280 mm, which results in a focal length of 700 mm[25]. With a focal length of 10 mm of the microscope objective we need to multiply the minimal resolution of the wavefront sensor with a factor $T = 70$. Thus the slope resolution of the full aperture is:

$$\delta z_{fullaperture} = T \cdot \delta z_{telescoped} = 16.8 \text{ nm}$$

with a phase resolution of:

$$\Delta\phi_{fullaperture} = T \cdot \Delta\phi_{telescoped} \approx \frac{\lambda_c}{50}$$

4.7.2 Laser focus diagnostic and dynamic range extension

ATLAS300 and also other high power lasers for laser plasma experiments operate with a nearly uniform flattop beam profile, to ensure efficient energy transport and to even the fluence on optical elements. The intensity distribution of a flattop beam profile in focus will have a sinc^2 distribution with its airy disc radius $r_{airy} \approx 1.22\lambda \cdot F$, where $F = A/f$ is the F-number of the system. Figure 4.24 compares a typical focus recorded with the microscope in the LION experiment in LEX photonics and a theoretical focus calculated from the sinc^2 distribution taking into account the same focusing geometry. While the area of both foci covered by the FWHM ratio is only slightly larger for the measured focus (1.7 times bigger) the difference in the lower intensity part is more pronounced. Compared to the theoretical focus, significant energy is scattered around the focus, which reduces the enclosed energy in the central part.
This effect is even more visible, if the dynamic range of the camera is increased. To analyze the focus with a higher dynamic range, we used a technique, which is based on multi image processing: A laser focus is initially

[24]The sensor used in the camera UI-5251LE-M has a signal to noise ratio of 39 to 41 which exceed the estimated range of 1:256

[25]Also longer focal length OAPs are discussed, however the microscope will then be adapted with a lower magnifying objective, which ultimately results in roughly the same telescoping factor

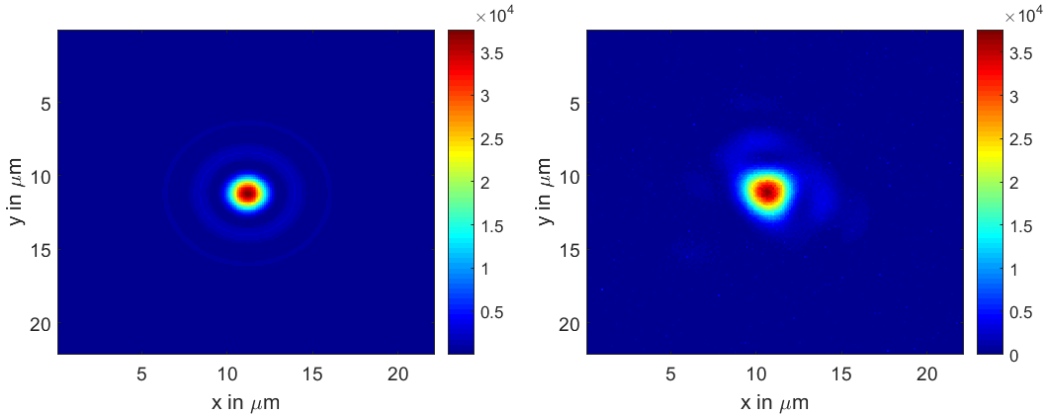

(a) Theoretical focus (b) Real focus

Figure 4.24: Comparison of a real focus measured with the microscope in the LION experiment in LEX photonics and a theoretical focus obtained with the same optics and a flat top beam profile via Fourier transformation.

recorded with the highest dynamic range, allowed per default by the image sensor of the camera, meaning, that the peak intensity of the focus is just below the saturation threshold of the camera. Then, another image is recorded with higher intensity, where parts of the laser focus are saturated on purpose. Thereby the intensity of lower intensity parts of the focus are increased and now visible in the recorded image. This process is repeated until the desired increase of dynamic range is reached, and before the damage threshold of the camera is reached. As a general rule, a fluence of a factor 10^4 times higher than the saturation limit with a femtosecond laser on a camera chip, will not generate permanent damages. Therefore, the initial dynamic range of the camera can be increased by the same factor. Figure 4.25 shows a line out of a focus recorded with such a technique.

4.8 Summary and conclusion

In this chapter we have described various developments for optical observations in vacuum in laser plasma experiments. Motivated by the eminent drawbacks of established semi-vacuum solutions for optical metrology in this experimental environment, the initial step was the development of affordable, vacuum compatible and emp resistant cameras. Based thereupon, a highly modal microscope dedicated to the special experimental requirements has been developed, featuring several additional metrologies that are unavailable

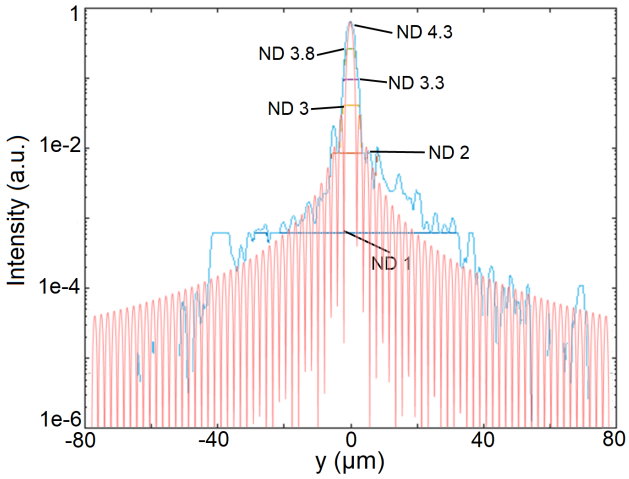

Figure 4.25: Line out of intensity distribution of a focal spot recorded with the HDR technique (blue) compared with a theoretical expected intensity distribution (red). The horizontal lines represent the different filter levels, which reduced the intensity of the laser. Picture adapted from [94].

by other means.
For an advanced target positioning, whitelight interference microscopy could be implemented into the microscope, without any loss of other diagnostic capabilities. With WLI an absolute position measurement with a range of 200 µm and a position accuracy with sub-µm level could be demonstrated. In addition to the positioning, with WLI we showed the possibility of 3D mapping in vacuum and higher contrast for ultra thin target detection, as well as advantages in characterization in terms of defects in the target, which opens the possibility for automized target quality evaluation. By spectral analysis of the reflected light of thin transparent targets, an online thickness measurement could be established, which rounds out the complete online target diagnostic with single, easy-to-use pre-characterized tool.
With the integration of a Shack-Hartmann sensor, an advanced laser characterization, in terms of the wavefront reconstruction could be demonstrated. The reconstructed wavefront will serve as an input signal for a deformable mirror in CALA, which will not only for the LION experiment, but also for the Laser-driven Undulator X-Ray Source (LUX), Electron and Thomson Test Facility (ETTF) and High Field Physics (HF) experiments optimize the wavefront for diffraction limited laser focusing. HDR imaging of a typical focus in the LION experiment in LEX photonics showed its necessity, as the peak intensity measured by HDR is typically by factors of 2-5 smaller than measured with limited dynamic range and assumption of gaussian in-

tensity distributions, which with todays high power laser systems represents an insufficient method.

4.9 Final configuration for LION@CALA

Besides the high versatility, the final configuration of the microscope was decided, by careful considerations of benefits and drawbacks of the single features. A 3D model of the final configuration for LION@CALA can be seen in figure 4.26, with the following features:

1. High magnification for focus alignment
2. Low magnification for larger field of view
3. Illumination of targets with an IR-LED
4. Spectral measurement of the laser beam via an optical fiber
5. Thickness determination of thin films via spectral reflectometry
6. Wavefront measurement with a Shack-Hartmann sensor

In the microscope setup for LION@CALA no WLI feature is planned, because it is the most complicated and due to the high sensitivity, the most demanding feature. Using WLI in the prototype has found no major difference in the target positioning on a sub-µm level compared to conventional positioning techniques. Furthermore, typical free-standing target-foils were found to be flat on length-scales exceeding the focal spot diameter by far. Overall these findings justify to avoid the additional cost and effort for WLI in the standard device. However at more specialized applications, like shaped targets in LION experiments WLI can offer significant advantages compared to conventional target diagnostics in the future.

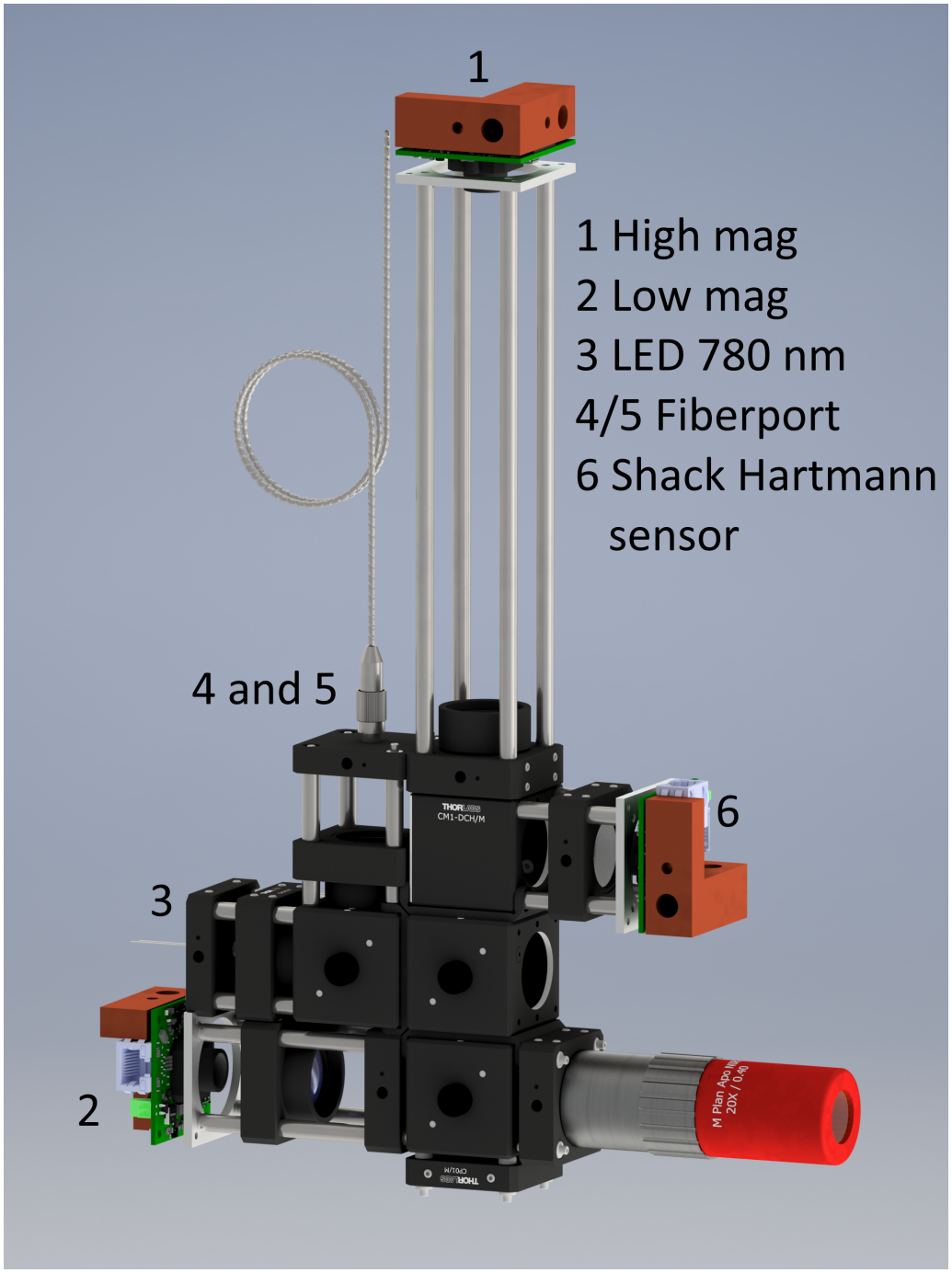

Figure 4.26: 3D model of the microscope for LION at CALA.

Chapter 5

Summary

In the framework of this thesis technological developments for laser ion acceleration experiments and the connected infrastructure have been investigated. For the design and realization of CALA, laser damage threshold studies have been performed. For this purpose, a dedicated vacuum chamber has been set up. With this setup laser damage threshold measurements of a wide range of substrate sizes (1-4 inch) can be measured in high vacuum environment, which represents optics usage in high power laser systems. By observation of the substrate surface with a vacuum microscope, we are able to monitor the laser damage behaviour online during the measurement. By characterization of the fluence distribution in substrate plane, uncertainties during conversion of fluence measured in laser plane to target plane are eliminated. A robust routine for LiDT measurements is now available and will allow evaluation of new coating designs and other optics-solutions that will arise over the next years.

In this thesis we presented an overview of laser damage threshold of companies, which are able to produce mirrors of sufficient size to support a 280 mm high power short pulse laser beam. In figure 5.1 an overview of the measured laser damage threshold is presented. The first row indicates different companies producing the mirror samples. In the second row, the lowest measured fluence to create a single shot damage on the substrate (ablation threshold) is denoted and the last row describes the highest fluence, under which the sample can withstand at least 3000 laser pulses (laser damage threshold). While there are fluctuations of up to 100 $\frac{\mathrm{mJ}}{\mathrm{cm}^2}$, this table can be seen as a current expectable laser damage threshold range for femtosecond laser mirrors of large size (able to support 280 mm beam) and other parameters like high reflectivity (R $\geq$ 98.8 % @ 740-860 nm) and cost per mirror ($\leq$ 30 k EUR).

Laser damage threshold measurements have also been performed for pulse compression gratings. In contrast to mirrors, the number of suppliers for

Company	LiDT single shot	LiDT 3000 pulses
I	550	450
I_2	460	420
II	420	400
III	460	400
IV	420	330
V	420	350

Figure 5.1: Laser damage thresholds of witness samples for full scale mirrors for the CALA laser beam delivery. Peak fluence in $\frac{\mathrm{mJ}}{\mathrm{cm}^2}$

gratings of the demanded size (support of a 280 mm beam) and performance ($R \geq 90$ % in the first diffraction order) is limited. In fact only two companies are able to produce gratings for the ATLAS 3000 laser. LiDT tests on witness samples of full scale gratings revealed the fragility of these components. In case of one witness sample, it showed completely unexpected behaviour. An accumulation of a contamination layer on the grating surface could be observed during illumination with laser fluences in the range of 10 to 200 $\frac{\mathrm{mJ}}{\mathrm{cm}^2}$, which ultimately led to a higher absorption of the laser pulse and thus lower damage threshold. No operation with this grating would have been possible with the anticipated fluence of the ATLAS 3000 laser (100 $\frac{\mathrm{mJ}}{\mathrm{cm}^2}$). A communication with the producing company finally led to retuning of production parameters, which eliminated the contamination sensitivity and also showed a satisfactory laser damage threshold (250 $\frac{\mathrm{mJ}}{\mathrm{cm}^2}$). This visualizes on the one hand the importance of laser damage threshold measurements of every component in the laser chain, as without the measurements in this thesis, gratings which are unsuitable for operation in ATLAS 3000 possibly would have been ordered. On the other hand laser damage threshold measurements can be a valuable feedback parameter for further developments on optical components.

Laser ion acceleration experimental methodology could be much improved by the development of a novel and advanced vacuum immersed microscope for target and laser focus diagnostic. With the in vacuum solution, the cumbersomeness and drawbacks (i.e. vignetting) of semi vacuum solutions, which were standard up to then and constitute still limiting factors in todays laser plasma experiments, could be avoided. With the compact design, further diagnostics became possible and the simple focus diagnostic for laser plasma experiments turned into a powerful tool for extensive laser and target diagnostic.
The microscope presented in this thesis has already evolved into a standard

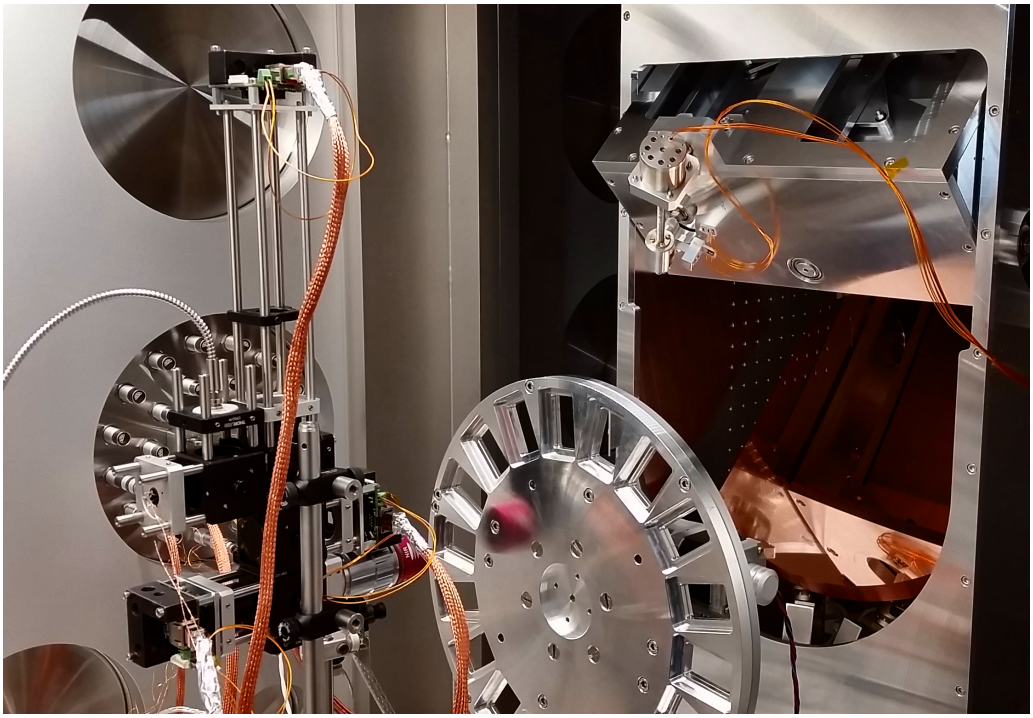

Figure 5.2: Microscope mounted in the experimental chamber of LION@CALA

diagnostic for laser plasma experiments in LEX photonics and due to its compactness could be transported and implemented in an experimental campaign at the Texas Petawatt laser in 2016. In CALA, this microscope is planned as the standard diagnostic for every experiment using the ATLAS 3000 laser. Moreover a custom developed wavefront sensor, which could be integrated in the microscope will provide feedback to a deformable mirror to optimize the wavefront of the laser, while simultaneously the focal spot can be measured and analyzed. In figure 5.2 a picture of the LION experimental chamber in CALA with the implemented microscope is shown. The microscope is ready to use and waiting for the experiment to start.

Chapter 6

Outlook

6.1 Online damage monitoring and advanced beam monitoring

Even though the mirrors for the laser beam delivery will be operated well below the laser damage threshold, laser damages can still occur, due to i.e. mistakes in laser usage. With an online observation of mirror integrity the degree of the laser damage could be limited and a propagation of the damage due to local field enhancements can be prevented. The event of laser damage can be precisely determined by the scatter behaviour of the mirror surface. In figure 6.1 an example of scattered laser light during a LiDT measurement can be seen. The mirror was illuminated as described in section 3.3.2. During illumination a partial overlap of laser illumination and camera integration is visible. Due to the rolling shutter of the camera, only the lower part of the image records the scattered laser light. As this example demonstrates, the scattered intensity is highly increased if damage is created. This shows, that observation of the mirror surface with a camera can be used for damage detection.
In the laser beam delivery in CALA every mirror holder is motorized and equipped with a camera, which is observing the mirror surface (compare figure 6.2). This camera is used for alignment of the LBD. If this camera is equipped with a nd filter, it can monitor the surface of the mirror during full power operation. Not only would this allow a control over drift of alignment during operation. This could also enable detection of small damages on the mirror surface, as demonstrated before. By automized analysis of the camera images, laser usage can be prohibited, if for example a certain threshold of scattered light is reached. This could limit damage propagation by field enhancements in diffraction maxima. Also by analysis of the scattered light

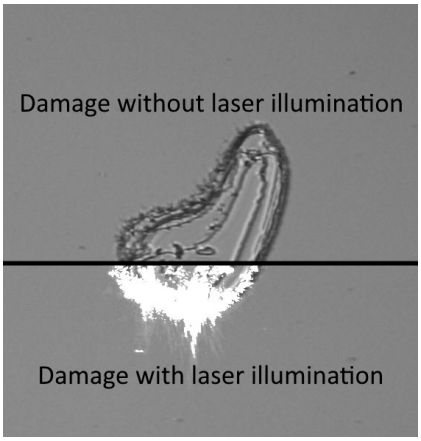

Figure 6.1: Comparison of damaged spot with and without laser illumination. During laser illumination light is strongly scattered by the damage. Light scattering of the surrounding intact surface is orders of magnitude smaller.

of the mirror surface or the grating surfaces, slow alterations of the surface by i.e. accumulation of a contamination layer can be detected.

6.2 Position measurement with confocal microscopy

For position measurement a technique called confocal microscopy [15] can be applied. Confocal microscopy is a point to point imaging technique, where a point light source (i.e. a laser) is focused onto the sample and the reflected light is imaged. If the sample is at the focal length of the microscope objective, this reflected light is then imaged as the smallest possible point in the image sensor, while a deviation from focal area results in a larger spot. The principle is illustrated in figure 6.3. With only simple modifications, the microscope presented in this thesis can be extended to also measure confocal displacement. With introducing a beamsplitter at the illumination port, a fiber with collimation optic can be placed, which delivers a collimated laser beam for illumination. The same fiber port at the microscopy setup, which was used to measure the optical spectrum in the FD-OCT can be used to transport the laser into the vacuum chamber. To have both options, the fiber at the air side simply has to be changed to the different devices.
To measure the displacement of the target, the size of the laser spot on the target surface is measured. The spot size is minimal, if the target is in the focal plane of the objective. With displacement in z this spot grows linearly

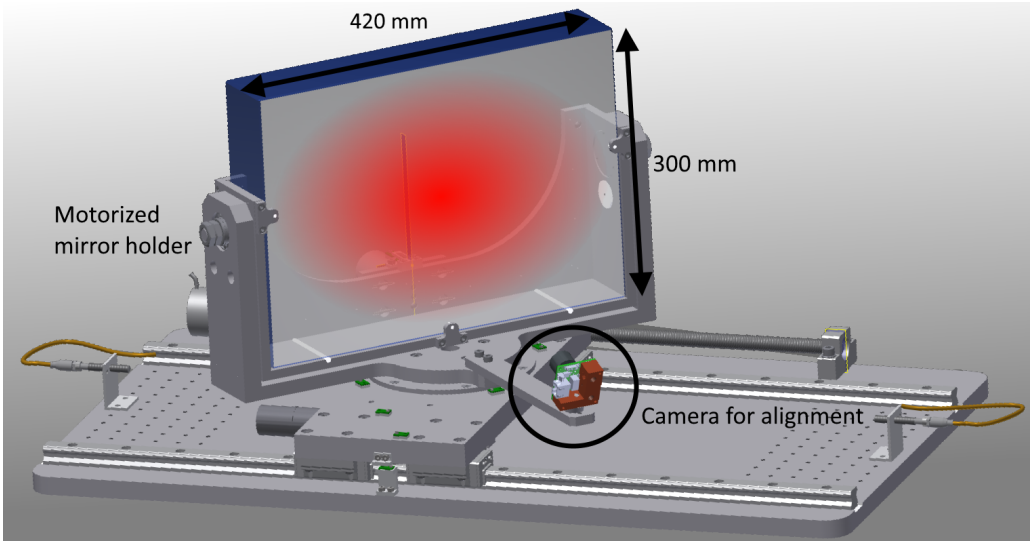

Figure 6.2: Optomechanics of a LBD mirror in CALA. Camera is used for alignment purpose

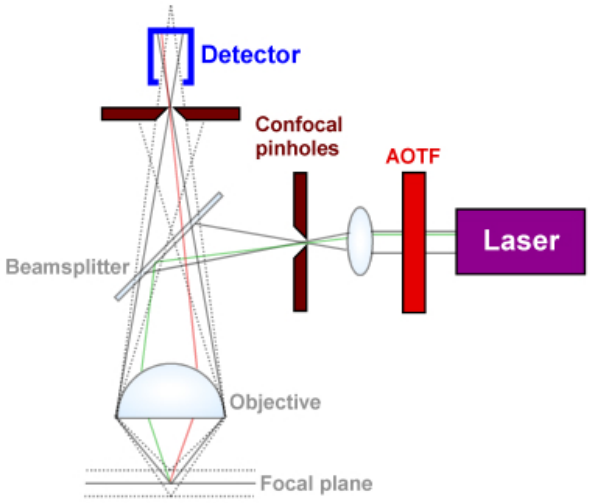

Figure 6.3: Principle of confocal microscopy. Picture taken from [102]

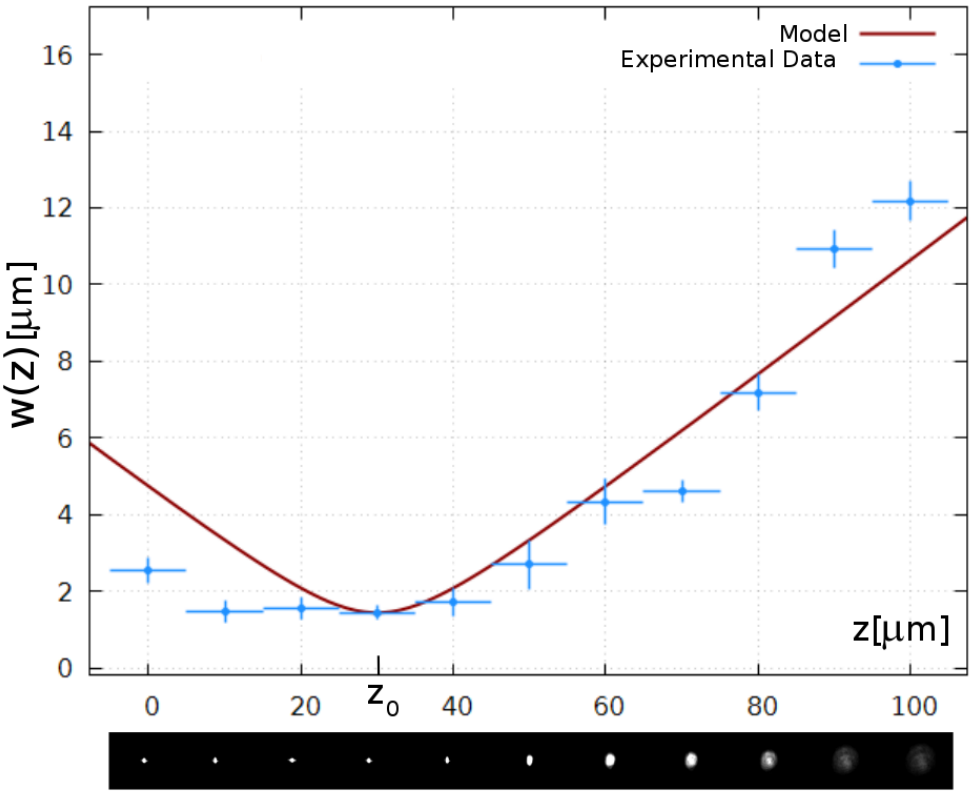

Figure 6.4: Measurement of displacement of a target with the confocal method. While the resolution close to the target range is low, with this method large displacements can quickly be calculated. Picture taken from [35]

and by measuring of the spot diameter, the z position can be calculated. In figure 6.4 a proof of concept measurement of this technique implemented into the microscope can be seen. The blue points represent the measured size of the laser diameter in respect to the displacement. The red curve represents the expected diameter assuming a Gaussian beam. The pictures below the measured spots show the recored frames in the camera. With this method, also targets which are hard to focus in a bright field microscope[1] can be detected and positioned by measurement of the reflected laser light. Moreover

[1]Perfect clean targets with no modulation of brightness in the field of view of a microscope can not be focused by judging if the image is 'sharp'. With improved target production techniques and proper target handling, the amount of stains and dust is drastically reduced, which leads to more difficulties for z positioning.

with this technique, similar to the WLI technique it is possible to detect if a target is present or not, which is also difficult, if the target is very clean.
At this state we showed the proof of principle of this technique, while an optimization was not applied yet. To increase resolution a higher control of illumination intensity has to be implemented and also an improved fitting model. However we could show, that with this technique a large displacement can be easily detected, while target detection is also highly improved.

6.3 Single frame high dynamic range (HDR) imaging

The microscope is used to measure the laser focus which will later shine on the target. The total size of the focus determines the intensity which will be present in the interaction. The dynamic range of a typical scientific camera is in the order of 66 dB and the signal to noise ratio is at max 41 dB[22]. Neither can the full dynamic range of such cameras be used, nor do we have conditions for highest signal to noise ratio. We typically have a camera which is able to detect 2-3 orders of magnitudes in a single frame. Having short pulse lasers we cannot change the integration time to change the energy on the camera chip. Several single pictures with different laser attenuations have to be recorded and a higher dynamic range image has to be calculated from these images.
With modification the microscope presented in this thesis is able to record such images in a single frame. A additional beam splitter is used in the high magnifying part and send on a 2D grating. This grating separates the beam into 9 different replicas. Each of these replicas have a different nd filter in front and thus hitting the camera with a different intensity. All these focus replicas can be used to calculate a single HDR image. Figure 6.5 illustrates this principle. This method is much faster, than recording single images with different attenuations and also is not sensitive to vibration and focus jitter. Additionally this method allows an automized calculation of a HDR focus image, because the foci all have the same relative distance.

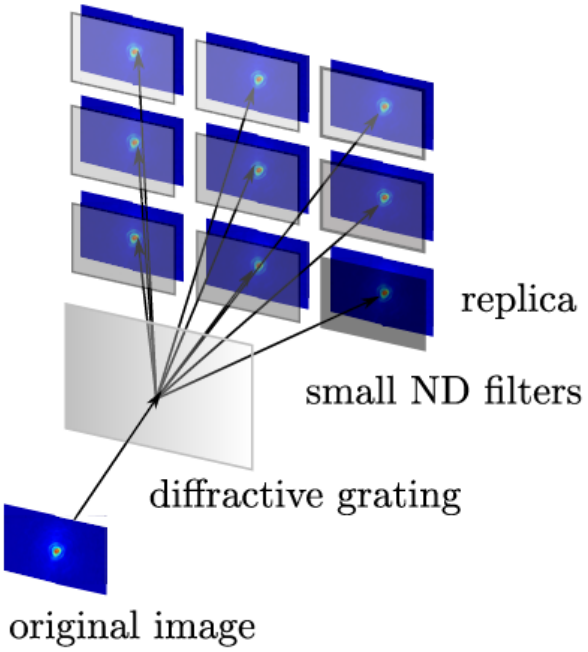

Figure 6.5: HDR imaging with a 2D grating dividing the original picture in 9 replicas which can be filtered independently. Picture taken from [8]

Appendix A

Non laser damages on optics in vacuum

We experienced in 2014 also non laser related damages on optics when exposed to vacuum. In our case we observed an exfoliation of the coating on the substrate. Figure A.1 illustrates the problem. The exact reasons for this behavior remain unclear. However communication with optic manufacturer revealed that this behavior can be addressed to 3 layer optics. Dielectric mirrors usually are made with two alternating refractive index materials. However, the layer composition can also be extended to 3 layers. Apparently the inter layer adhesion can be problematic as the example proofs.

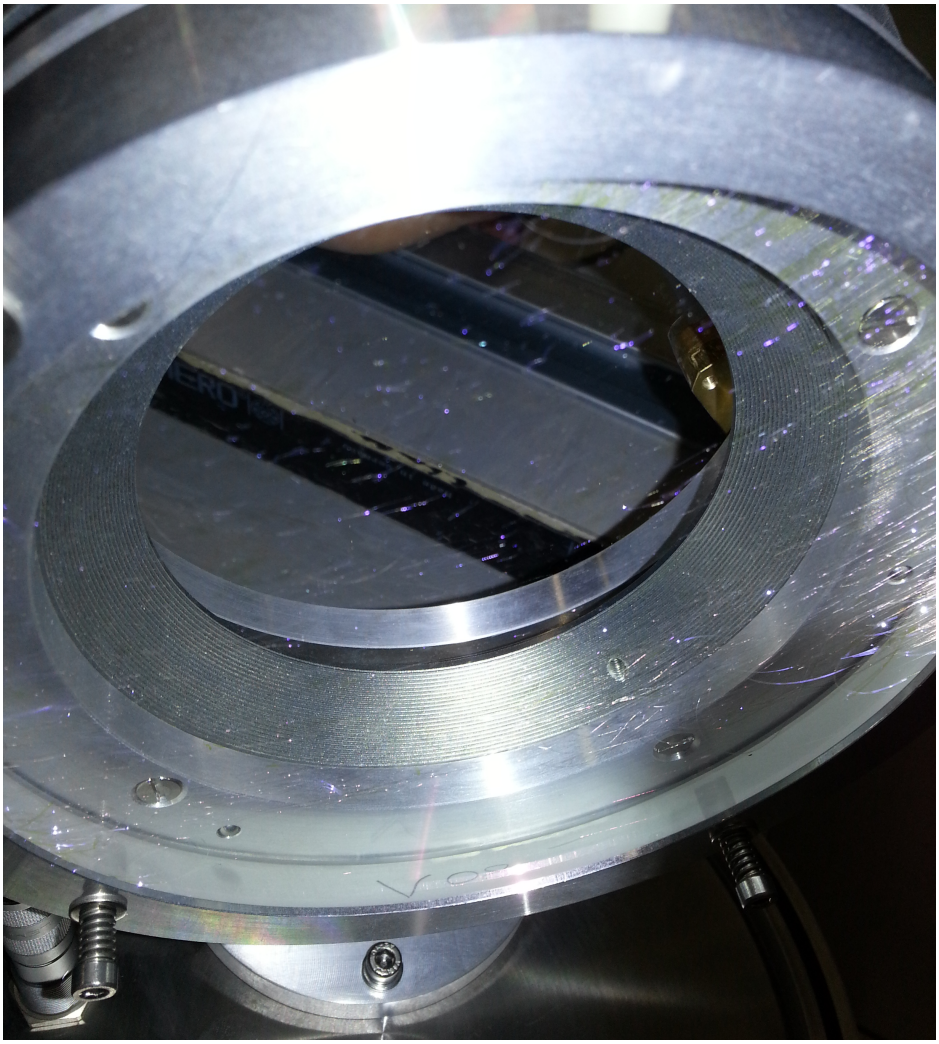

Figure A.1: Non laser related damage of optic in vacuum. The dielectric coating was exfoliated due to unknown reasons.

Bibliography

[1] Ceyhun Akcay, Pascale Parrein, and Jannick P. Rolland. Estimation of longitudinal resolution in optical coherence imaging. *Appl. Opt.*, 41(25):5256–5262, Sep 2002.

[2] D Ashkenasi, M Lorenz, Razvan Stoian, and a Rosenfeld. Surface damage threshold and sturcturing of dielectrics using femtosecond laser pulses: the role of incubation. *Applied Surface Science*, 150:101–106, 1999.

[3] H. Baumhacker, G. Pretzler, K. J. Witte, M. Hegelich, M. Kaluza, S. Karsch, A. Kudryashov, V. Samarkin, and A. Roukossouev. Correction of strong phase and amplitude modulations by two deformable mirrors in a multistaged ti:sapphire laser. *Opt. Lett.*, 27(17):1570–1572, Sep 2002.

[4] J. Bin, W. Ma, K. Allinger, D. Kiefer, P. Hilz, S. Reinhardt, W. Assmann, D. Habs, J. Schreiber, G. A. Drexler, A. A. Friedl, N. Humble, D. Michalski, M. Molls, T. E. Schmid, O. Zlobinskaya, and J. J. Wilkens. Laser driven ion source from ultrathin foils and its biomedical application. In *2012 Abstracts IEEE International Conference on Plasma Science*, pages 5C–6–5C–6, July 2012.

[5] J. H. Bin, W. J. Ma, K. Allinger, H. Y. Wang, D. Kiefer, S. Reinhardt, P. Hilz, K. Khrennikov, S. Karsch, X. Q. Yan, F. Krausz, T. Tajima, D. Habs, and J. Schreiber. On the small divergence of laser-driven ion beams from nanometer thick foils. *Physics of Plasmas*, 20(7):073113, 2013.

[6] E. S. Bliss, D. Milam, and R. A. Bradbury. Dielectric mirror damage by laser radiation over a range of pulse durations and beam radii. *Appl. Opt.*, 12(4):677–689, Apr 1973.

[7] N Bloembergen. Role of cracks, pores, and absorbing inclusions on laser induced damage threshold at surfaces of transparent dielectrics. *Applied optics*, 12(4):661–664, 1973.

[8] Christina Bömer. Optical diagnostics of high energetic laser plasma interactions. Master's thesis, LMU Muenchen, 10 2014.

[9] Alain Bosseboeuf and Sylvain Petitgrand. Characterization of the static and dynamic behaviour of m(o)ems by optical techniques: status and trends. *Journal of Micromechanics and Microengineering*, 13(4):S23, 2003.

[10] C. W. Carr, H. B. Radousky, and S. G. Demos. Wavelength dependence of laser-induced damage: Determining the damage initiation mechanisms. *Phys. Rev. Lett.*, 91:127402, Sep 2003.

[11] A. M. Chen, H. F. Xu, Y. F. Jiang, L. Z. Sui, D. J. Ding, H. Liu, and M. X. Jin. Modeling of femtosecond laser damage threshold on the two-layer metal films. *Applied Surface Science*, 257(5):1678–1683, 2010.

[12] B. Chimier, O. Utéza, N. Sanner, M. Sentis, T. Itina, P. Lassonde, F. Légaré, F. Vidal, and J. C. Kieffer. Damage and ablation thresholds of fused-silica in femtosecond regime. *Physical Review B - Condensed Matter and Materials Physics*, 84(9):1–10, 2011.

[13] F. Brunei Corkum P. B. and N. K. Sherman. Thermal Response of Metals to Ultrashort-Pulse Laser Excitation. *Physical Review Letters*, 61(25):2886–2889, 1988.

[14] Hiroyuki Daido, Mamiko Nishiuchi, and Alexander S Pirozhkov. Review of laser-driven ion sources and their applications. *Reports on progress in physics. Physical Society (Great Britain)*, 75(5):056401, 2012.

[15] P. Davidocits and M. D. Egger. Scanning laser microscope. *Nature*, 223:831, 1969.

[16] Peter de Groot, Jim Biegen, Jack Clark, Xavier Colonna de Lega, and David Grigg. Optical interferometry for measurement of the geometric dimensions of industrial parts. *Appl. Opt.*, 41(19):3853–3860, Jul 2002.

[17] Peter de Groot and Leslie Deck. Surface profiling by analysis of white-light interferograms in the spatial frequency domain. *Journal of Modern Optics*, 42(2):389–401, 1995.

[18] N. V. Didenko, A. V. Konyashchenko, A. P. Lutsenko, and S. Y. Tenyakov. Contrast degradation in a chirped-pulse amplifier due to generation of prepulses by postpulses. *Optics Express*, 16(5):3178, 2008.

[19] G. Doumy, F. Quéré, O. Gobert, M. Perdrix, Ph. Martin, P. Audebert, J. C. Gauthier, J.-P. Geindre, and T. Wittmann. Complete characterization of a plasma mirror for the production of high-contrast ultraintense laser pulses. *Phys. Rev. E*, 69:026402, Feb 2004.

[20] B. Dromey, S. Kar, M. Zepf, and P. Foster. The plasma mirror—a subpicosecond optical switch for ultrahigh power lasers. *Review of Scientific Instruments*, 75(3):645–649, 2004.

[21] D. Du, X. Liu, G. Korn, J. Squier, and G. Mourou. Laser-induced breakdown by impact ionization in SiO2 with pulse widths from 7 ns to 150 fs. *Applied Physics Letters*, 64(23):3071–3073, 1994.

[22] e2v. *EV76C560*, 2011.

[23] Micro Epsilon. Konfocale messsysteme für weg, abstand position und dicke. `http://www.micro-epsilon.de/displacement-position-sensors/confocal-sensor/`, 2017. [Online; accessed 26-October-2017].

[24] International Organization for Standardization. Test methods for laser-induced damage threshold – part 1: Definitions and general principles. *ISO21254-1:2011 Lasers and laser-related equipment*, 2011.

[25] S. Fourmaux, S. Payeur, A. Alexandrov, C. Serbanescu, F. Martin, T. Ozaki, A. Kudryashov, and J. C. Kieffer. Laser beam wavefront correction for ultra high intensities with the 200 tw laser system at the advanced laser light source. *Opt. Express*, 16(16):11987–11994, Aug 2008.

[26] James G. Fujimoto, Costas Pitris, Stephen A. Boppart, and Mark E. Brezinski. Optical coherence tomography: An emerging technology for biomedical imaging and optical biopsy. *Neoplasia*, 2(1):9 – 25, 2000.

[27] Ying Gao, Jianhui Bin, Daniel Haffa, Christian Kreuzer, Jens Hartmann, Martin Speicher, Florian H. Lindner, Tobias M. Ostermayr, Peter Hilz, Thomas F. Rösch, and et al. An automated, 0.5 hz nano-foil target positioning system for intense laser plasma experiments. *High Power Laser Science and Engineering*, 5, 2017.

[28] Rafael R. Gattass and Eric Mazur. Femtosecond laser micromachining in transparent materials. *Nature Photonics*, 2(4):219–225, 2008.

[29] Erhard W. Gaul, Mikael Martinez, Joel Blakeney, Axel Jochmann, Martin Ringuette, Doug Hammond, Ted Borger, Ramiro Escamilla, Skylar Douglas, Watson Henderson, Gilliss Dyer, Alvin Erlandson, Rick Cross, John Caird, Christopher Ebbers, and Todd Ditmire. Demonstration of a 1.1 petawatt laser based on a hybrid optical parametric chirped pulse amplification/mixed nd:glass amplifier. *Appl. Opt.*, 49(9):1676–1681, Mar 2010.

[30] Victor Garcia Gisbert. Applied optical metrology methods for target positioning and profiling in vacuum for laser plasma interaction. Master's thesis, LMU, 2016.

[31] E. Gubbini, G. Kommol, M. Schnürer, H. Schönagel, U. Eichmann, M.P. Kalashnikov, P.V. Nickles, F. Eggenstein, G. Reichardt, and W. Sandner. "on-line" cleaning of optical components in a multi-tw-ti:sa laser system. *Vacuum*, 76(1):45 – 49, 2004.

[32] D. Habs, P. G. Thirolf, M. Gross, K. Allinger, J. Bin, A. Henig, D. Kiefer, W. Ma, and J. Schreiber. Introducing the fission–fusion reaction process: using a laser-accelerated th beam to produce neutron-rich nuclei towards the n=126 waiting point of the r-process. *Applied Physics B*, 103(2):471–484, May 2011.

[33] Stephen P. Hatchett, Curtis G. Brown, Thomas E. Cowan, Eugene A. Henry, Joy S. Johnson, Michael H. Key, Jeffrey A. Koch, A. Bruce Langdon, Barbara F. Lasinski, Richard W. Lee, Andrew J. Mackinnon, Deanna M. Pennington, Michael D. Perry, Thomas W. Phillips, Markus Roth, T. Craig Sangster, Mike S. Singh, Richard A. Snavely, Mark A. Stoyer, Scott C. Wilks, and Kazuhito Yasuike. Electron, photon, and ion beams from the relativistic interaction of petawatt laser pulses with solid targets. *Physics of Plasmas*, 7(5):2076–2082, 2000.

[34] Eugene Hecht. *Optik*. De Gruyter Oldenbourg, 5 edition, 1989. page 695-696.

[35] Sebastian Herr. Design and implementation of an integrated device for laser beam and target analysis for laser ion acceleration. Master's thesis, LMU, 2017.

[36] A. Hertwig, S. Martin, J. Krüger, and W. Kautek. Surface damage and color centers generated by femtosecond pulses in borosilicate glass and silica. *Applied Physics A*, 79(4):1075–1077, 2004.

[37] Floyd E. Hovis, Bart A. Shepherd, Christopher T. Radcliffe, and Henry A. Maliborski. Mechanisms of contamination-induced optical damage in lasers. *Proc.SPIE*, 2428:2428 – 2428 – 12, 1995.

[38] IDS-Imaging. Ui-5241-camera finder. `https://en.ids-imaging.com/store/products/cameras/ui-5241le.html`, 2017. [Online; accessed 10-Decemberl-2017].

[39] Spectral Instruments Inc. 800s ccd camera. `http://www.specinst.com/Brochures%20Rev%20B/800S-camera-broch_revB.pdf`, 2017. [Online; accessed 03-November-2017].

[40] Lonzaga J. B., Avanesyan S. M., Langford S. C., and Dickinson J. T. Color center formation in soda-lime glass with femtosecond laser pulses. *Journal of Applied Physics*, 94(4332), 2003.

[41] Lan Jiang and Hai-Lung Tsai. Improved Two-Temperature Model and Its Application in Ultrashort Laser Heating of Metal Films. *Journal of Heat Transfer*, 127(10):1167, 2005.

[42] David B. Joyce and Frederick Schmid. Progress in the growth of large scale ti:sapphire crystals by the heat exchanger method (hem) for petawatt class lasers. *Journal of Crystal Growth*, 312(8):1138 – 1141, 2010. The 17th American Conference on Crystal Growth and Epitaxy/The 14th US Biennial Workshop on Organometallic Vapor Phase Epitaxy/The 6th International Workshop on Modeling in Crystal Growth.

[43] A. Jullien, J.-P. Rousseau, B. Mercier, L. Antonucci, O. Albert, G. Chériaux, S. Kourtev, N. Minkovski, and S.M. Saltiel. Highly efficient nonlinear filter for femtosecond pulse contrast enhancement and pulse shortening. *Optics Letters*, 33(20):2353–2355, 2008.

[44] Stefan Karsch, Zsuzsanna Major, József Fülöp, Izhar Ahmad, Tie-Jun Wang, Andreas Henig, Sebastian Kruber, Raphael Weingartner, Mathias Siebold, Joachim Hein, Christoph Wandt, Sandro Klingebiel, Jens Osterhoff, Rainer Hörlein, and Ferenc Krausz. The petawatt field synthesizer: A new approach to ultrahigh field generation. In *Advanced Solid-State Photonics*, page WF1. Optical Society of America, 2008.

[45] L. V. Keldysh. Ionization in the field of a strong electromagnetic wave. *Soviet Physics JETP*, 20(5):1307–1314, 1965.

[46] P. Ewen King-Smith. Three Interferometric Methods for Measuring the Thickness of Layers of the Tear Film. *Optometry and vision science*, 76:19–32, 1999.

[47] Maximilian Kögler. Construction of a vacuum microscope. Bachelor thesis, LMU-München, 9 2014.

[48] Jörg Krüger, Daniela Dufft, Robert Koter, and Andreas Hertwig. Femtosecond laser-induced damage of gold films. *Applied Surface Science*, 253(19):7815–7819, 2007.

[49] K. Krushelnick, E. L. Clark, R. Allott, F. N. Beg, C. N. Danson, A. Machacek, V. Malka, Z. Najmudin, D. Neely, P. A. Norreys, M. R. Salvati, M. I. K. Santala, M. Tatarakis, I. Watts, M. Zepf, and A. E. Dangor. Ultrahigh-intensity laser-produced plasmas as a compact heavy ion injection source. *IEEE Transactions on Plasma Science*, 28(4):1110–1155, Aug 2000.

[50] Peter Lebedew. Untersuchungen über die druckkräfte des lichtes. *Annalen der Physik*, 311(11):433–458, 1901.

[51] F. H. Lindner, J. H. Bin, F. Englbrecht, D. Haffa, P. R. Bolton, Y. Gao, J. Hartmann, P. Hilz, C. Kreuzer, T. M. Ostermayr, T. F. Rösch, M. Speicher, K. Parodi, P. G. Thirolf, and J. Schreiber. A novel approach to electron data background treatment in an online wide-angle spectrometer for laser-accelerated ion and electron bunches. *Review of Scientific Instruments*, 89(1):013301, 2018.

[52] F. H. Lindner, D. Haffa, J. H. Bin, F. Englbrecht, Y. Gao, J. Gebhard, J. Hartmann, P. Hilz, C. Kreuzer, S. Lehrack, T. M. Ostermayr, T. F. Rösch, M. Speicher, M. Würl, K. Parodi, J. Schreiber, and P. G. Thirolf. Towards swift ion bunch acceleration by high-power laser pulses at the Centre for Advanced Laser Applications (CALA). *Nuclear Instruments and Methods in Physics Research, Section B: Beam Interactions with Materials and Atoms*, 402:354–357, 2017.

[53] S Luan, M H R Hutchinson, R A Smith, and F Zhou. High dynamic range third-order correlation measurement of picosecond laser pulse shapes. *Measurement Science and Technology*, 4(12):1426, 1993.

[54] W. J. Ma, J. H. Bin, H. Y. Wang, M. Yeung, C. Kreuzer, M. Streeter, P. S. Foster, S. Cousens, D. Kiefer, B. Dromey, X. Q. Yan, J. Meyer-Ter-Vehn, M. Zepf, and J. Schreiber. Bright subcycle extreme ultraviolet bursts from a single dense relativistic electron sheet. *Physical Review Letters*, 113(23), dec 2014.

[55] Wenjun Ma, V. Kh Liechtenstein, J. Szerypo, D. Jung, P. Hilz, B. M. Hegelich, H. J. Maier, J. Schreiber, and D. Habs. Preparation of self-supporting diamond-like carbon nanofoils with thickness less than 5 nm for laser-driven ion acceleration. *Nuclear Instruments and Methods in Physics Research, Section A: Accelerators, Spectrometers, Detectors and Associated Equipment*, 655(1):53–56, 2011.

[56] Andrea Macchi. A Review of Laser-Plasma Ion Acceleration. *arXiv*, pages 1–24, 2017.

[57] Andrea Macchi, Marco Borghesi, and Matteo Passoni. Ion acceleration by superintense laser-plasma interaction. *Rev. Mod. Phys.*, 85:751–793, May 2013.

[58] T. H. Maiman. Stimulated Optical Radiation in Ruby. *Nature*, 187(4736):493–494, 1960.

[59] F. J. McClung and R. W. Hellwarth. Giant optical pulsations from ruby. *Appl. Opt.*, 1(S1):103–105, Jan 1962.

[60] M. J. Mead, D. Neely, J. Gauoin, and R. Heathcote. Electromagnetic pulse generation within a petawatt laser target chamber. *Review of scientif instruments*, 2004.

[61] M Mero, B Clapp, J C Jasapara, W Rudolph, D Ristau, K Starke, J Kruger, S Martin, and W Kautek. On the damage behavior of dielectric films when illuminated with multiple femtosecond laser pulses. *Optical Engineering*, 44(5):51107, 2005.

[62] M. Mero, J. Liu, W. Rudolph, D. Ristau, and K. Starke. Scaling laws of femtosecond laser pulse induced breakdown in oxide films. *Phys. Rev. B*, 71:115109, Mar 2005.

[63] A.A. Michelson and E.W. Morley. On the relative motion of the earth and the luminiferous ether. *American Journal of Science*, XXXIV(203), 1887.

[64] Robert C. Miller. Optical second harmonic generation in piezoelectric crystals. *Applied Physics Letters*, 5(1):17–19, 1964.

[65] Kazuhisa Nakajima, Jianjun Yuan, Liming Chen, and Zhengming Sheng. Laser-driven very high energy electron/photon beam radiation therapy in conjunction with a robotic system. *Applied Sciences*, 5(1):1–20, 2015.

[66] Daniel R. Neal, James Copland, and David A. Neal. Shack-Hartmann wavefront sensor precision and accuracy. *Proccedings of SPIE*, 4779:148, 2002.

[67] S. S. Nekrashevich and V. A. Gritsenko. Electronic structure of silicon dioxide (a review). *Physics of the Solid State*, 56(2):207–222, 2014.

[68] D Nguyen, L Emmert, P Schwoebel, D Patel, C Menoni, M Shinn, and W Rudolph. Femtosecond pulse damage thresholds of dielectric coatings in vacuum. *Optics Express*, 19(6):5690–7, 2011.

[69] Edmund optics. Using tube lenses with infinity corrected objectives. `https://www.edmundoptics.com/resources/application-notes/microscopy/using-tube-lenses-with-infinity-corrected-objectives/`, 2017. [Online; accessed 12-October-2017].

[70] T. M. Ostermayr, J. Gebhard, D. Haffa, D. Kiefer, C. Kreuzer, K. Allinger, C. Bömer, J. Braenzel, M. Schnürer, I. Cermak, J. Schreiber, and P. Hilz. A transportable paul-trap for levitation and accurate positioning of micron-scale particles in vacuum for laser-plasma experiments. *Review of Scientific Instruments*, 89(1):013302, 2018.

[71] Sasi Palaniyappan, Chengkun Huang, Donald C Gautier, Christopher E Hamilton, Miguel A Santiago, Christian Kreuzer, Adam B Sefkow, Rahul C Shah, and Juan C Fernández. Efficient quasi-monoenergetic ion beams from laser-driven relativistic plasmas. *Nature communications*, 6:10170, 2015.

[72] Charlotte A. J. Palmer, N. P. Dover, I. Pogorelsky, M. Babzien, G. I. Dudnikova, M. Ispiriyan, M. N. Polyanskiy, J. Schreiber, P. Shkolnikov, V. Yakimenko, and Z. Najmudin. Monoenergetic proton beams accelerated by a radiation pressure driven shock. *Phys. Rev. Lett.*, 106:014801, Jan 2011.

[73] M. D. Perry, D. Pennington, B. C. Stuart, G. Tietbohl, J. A. Britten, C. Brown, S. Herman, B. Golick, M. Kartz, J. Miller, H. T. Powell, M. Vergino, and V. Yanovsky. Petawatt laser pulses. *Opt. Lett.*, 24(3):160–162, Feb 1999.

[74] M. D. Perry, B. C. Stuart, P. S. Banks, M. D. Feit, V. Yanovsky, and A. M. Rubenchik. Ultrashort-pulse laser machining of dielectric materials. *Journal of Applied Physics*, 85(9):6803–6810, 1999.

[75] M.C. Polo, J.L. Andújar, A. Hart, J. Robertson, and W.I. Milne. Preparation of tetrahedral amorphous carbon films by filtered cathodic vacuum arc deposition. *Diamond and Related Materials*, 9(3–6):663 – 667, 2000.

[76] V. S. Popov, V. D. Mur, B. M. Karnakov, and S. G. Pozdnyakov. On the relativistic generalization of Keldysh ionization theory. *Physics Letters, Section A: General, Atomic and Solid State Physics*, 358(1):21–26, 2006.

[77] B. Qiao, M. Zepf, M. Borghesi, and M. Geissler. Stable gev ion-beam acceleration from thin foils by circularly polarized laser pulses. *Phys. Rev. Lett.*, 102:145002, Apr 2009.

[78] P. Raczka, J.-L. Dubois, S. Hulin, V. Tikhonchuk, M. Rosinski, A. Zaras-Szydlowska, and J. Badziak. Strong electromagnetic pulses generated in high-intensity short-pulse laser interactions with thin foil targets. *Laser and Particle Beams*, page 1–10, 2017.

[79] S Reinhardt, W Draxinger, J Schreiber, and W Assmann. A pixel detector system for laser-accelerated ion detection. *Journal of Instrumentation*, 8(03):P03008, 2013.

[80] Wolfram Research. Fourier transform spectrometer – from eric weinstein's world of physics. `http://scienceworld.wolfram.com/physics/FourierTransformSpectrometer.html`, 2017. [Online; accessed 01-December-2017].

[81] Wolfgang Riede, Paul Allenspacher, Helmut Schröde, Denny Wernham, and Yngve Lien. Laser-induced hydrocarbon contamination in vacuum. *Proc.SPIE*, 5991:5991 – 5991 – 13, 2006.

[82] Detlev Ristau. *Laser-induced damage in optical materials*. CRC-press, 2015. page 3-23.

[83] Williams R.T. Optically generated lattice defects in halide crystals. *Optical Engineering*, 28(281034), 1989.

[84] Ewa Schab-Balcerzak, Anna Sobolewska, Andrzej Miniewicz, Jan Jurusik, and Bozena Jarzabek. Photoinduced Holographic Gratings in Azobenzene-Functionalized Poly(amideimide)s. *Polymer Journal*, 39(7):659–669, 2007.

[85] Chris B Schaffer, André Brodeur, and Eric Mazur. Laser-induced breakdown and damage in bulk transparent materials induced by tightly focused femtosecond laser pulses. *Measurement Science and Technology*, 12(11):1784–1794, 2001.

[86] H. Schwoerer, S. Pfotenhauer, O. Jäckel, K. U. Amthor, B. Liesfeld, W. Ziegler, R. Sauerbrey, K. W D Ledingham, and T. Esirkepov. Laser-plasma acceleration of quasi-monoenergetic protons from microstructured targets. *Nature*, 439(7075):445–448, 2006.

[87] Lovisa Senje, Mark Yeung, Bastian Aurand, Stephan Kuschel, Christian Rödel, Florian Wagner, Kun Li, Brendan Dromey, Vincent Bagnoud, Paul Neumayer, Markus Roth, Claes-Göran Wahlström, Matthew Zepf, Thomas Kuehl, and Daniel Jung. Diagnostics for studies of novel laser ion acceleration mechanisms. *Review of Scientific Instruments*, 85(11):113302, 2014.

[88] Sebastian Seuferling, Matthias Alexander Otto Haug, Peter Hilz, Daniel Haffa, Christian Kreuzer, and Jörg Schreiber. Efficient offline production of freestanding thin plastic foils for laser-driven ion sources. *High Power Laser Science and Engineering*, 5, 2017.

[89] R. V. Shack and B. C. Platt. Production and Use of a Lenticular Hartmann Screen. In Dow S. Chairman, editor, *Spring Meeting of the Optical Society of America*. Optical Society of America, Optical Society of America, April 1971.

[90] Prashant Kumar Singh, K.F. Kakolee, T.W. Jeong, and Sargis Ter-Avetisyan. A diagnostic for micrometer sensitive positioning of solid targets in intense laser-matter interaction. *Nuclear Instruments and Methods in Physics Research Section A: Accelerators, Spectrometers, Detectors and Associated Equipment*, 829(Supplement C):363 – 366, 2016. 2nd European Advanced Accelerator Concepts Workshop - EAAC 2015.

[91] R. A. Snavely, M. H. Key, S. P. Hatchett, T. E. Cowan, M. Roth, T. W. Phillips, M. A. Stoyer, E. A. Henry, T. C. Sangster, M. S. Singh, S. C. Wilks, A. MacKinnon, A. Offenberger, D. M. Pennington, K. Yasuike, A. B. Langdon, B. F. Lasinski, J. Johnson, M. D. Perry, and E. M. Campbell. Intense high-energy proton beams from petawatt-laser irradiation of solids. *Phys. Rev. Lett.*, 85:2945–2948, Oct 2000.

[92] M. J. Soileau. 40 Year Retrospective of Fundamental Mechanisms. *Laser-Induced Damage in Optical Materials*, 7132(Lid):713201–713201–14, 2008.

[93] W.H. Southwell. Wave-front estimation from wave-front slope measurements. *Journal of the Optical Society of America*, 70(8):998, 1980.

[94] Martin Speicher. Optical probing for on-target laser contrast measurement. Master's thesis, LMU Muenchen, 2016.

[95] Donna Strickland and Gerard Mourou. Compression of amplified chirped optical pulses. *Optics Communications*, 55(6):447 – 449, 1985.

[96] B. C. Stuart, M. D. Feit, S. Herman, A. M. Rubenchik, B. W. Shore, and M. D. Perry. Nanosecond-to-femtosecond laser-induced breakdown in dielectrics. *Physical Review B*, 53(4):1749–1761, 1996.

[97] B. C. Stuart, M. D. Feit, A. M. Rubenchik, B. W. Shore, and M. D. Perry. Laser-induced damage in dielectrics with nanosecond to subpicosecond pulses. *Physical Review Letters*, 74(12):2248–2251, 1995.

[98] Toshiki Tajima, Dietrich Habs, and Xueqing Yan. Laser acceleration of ions for radiation therapy. *Reviews of Accelerator Science and Technology*, 02(01):201–228, 2009.

[99] An-Chun Tien, Sterling Backus, Henry Kapteyn, Margaret Murnane, and Gérard Mourou. Short-Pulse Laser Damage in Transparent Materials as a Function of Pulse Duration. *Physical Review Letters*, 82(19):3883–3886, 1999.

[100] E. Treacy. Optical pulse compression with diffraction gratings. *IEEE Journal of Quantum Electronics*, 5(9):454–458, Sep 1969.

[101] European Union. Ted tender electronic daily. `http://ted.europa.eu/udl?uri=TED:NOTICE:25425-2016:TEXT:DE:HTML&src=0`, 2016. [Online; accessed 11-April-2017].

[102] Brandeis University. A practical guide for fluorescent confocal microscopy. https://blogs.brandeis.edu/marderlab/a-practical-guide-for-fluorescent-confocal-microscopy/, 2017. [Online; accessed 19-November-2017].

[103] E. W. Van Stryland, M. J. Soileau, Arthur L. Smirl, and William E. Williams. Pulse-width and focal-volume dependence of laser-induced breakdown. *Phys. Rev. B*, 23:2144–2151, Mar 1981.

[104] F. Wagner, C. Brabetz, O. Deppert, M. Roth, T. Stöhlker, An. Tauschwitz, A. Tebartz, B. Zielbauer, and V. Bagnoud. Accelerating ions with high-energy short laser pulses from submicrometer thick targets. *High Power Laser Science and Engineering*, 4(2016):e45, 2016.

[105] Christian Weindl. Entwicklung eines emp-sicheren kameragehäuses. Bachelor thesis, LMU-München, 2016.

[106] S. S. Wellershoff, J. Hohlfeld, J. Güdde, and E. Matthias. The role of electron-phonon coupling in femtosecond laser damage of metals. *Applied Physics A: Materials Science and Processing*, 69(7):99–107, 1999.

[107] Wikipedia. Laser - wikipedia. https://en.wikipedia.org/wiki/Laser, 2017. [Online; accessed 10-April-2017].

[108] S. C. Wilks, A. B. Langdon, T. E. Cowan, M. Roth, M. Singh, S. Hatchett, M. H. Key, D. Pennington, A. MacKinnon, and R. A. Snavely. Energetic proton generation in ultra-intense laser–solid interactions. *Physics of Plasmas*, 8(2):542–549, 2001.

[109] Maciej Wojtkowski, Vivek Srinivasan, James G. Fujimoto, Tony Ko, Joel S. Schuman, Andrzej Kowalczyk, and Jay S. Duker. Three-dimensional retinal imaging with high-speed ultrahigh-resolution optical coherence tomography. *Ophthalmology*, 112(10):1734 – 1746, 2005.

[110] XCAM. Cavacam (s) – camera for vacuum applications fully vacuum immersible. http://www.xcam.co.uk/cavacam-s-%E2%80%93-camera-vacuum-applications-fully-vacuum-immersible, 2017. [Online; accessed 03-November-2017].

[111] V Yanovsky, V Chvykov, G Kalinchenko, P Rousseau, T Planchon, T Matsuoka, A Maksimchuk, J Nees, G Cheriaux, G Mourou, and K Krushelnick. Ultra-high intensity- 300-TW laser at 0.1 Hz repetition rate. *Optics Express*, 16(3):2109–2114, 2008.

[112] M. Yeung, B. Dromey, S. Cousens, T. Dzelzainis, D. Kiefer, J. Schreiber, J. H. Bin, W. Ma, C. Kreuzer, J. Meyer-Ter-Vehn, M. J V Streeter, P. S. Foster, S. Rykovanov, and M. Zepf. Dependence of laser-driven coherent synchrotron emission efficiency on pulse ellipticity and implications for polarization gating. *Physical Review Letters*, 112(12), dec 2013.

[113] Tae Jun Yu, Seong Ku Lee, Jae Hee Sung, Jin Woo Yoon, Tae Moon Jeong, and Jongmin Lee. Generation of high-contrast, 30 fs, 1.5 pw laser pulses from chirped-pulse amplification ti:sapphire laser. *Opt. Express*, 20(10):10807–10815, May 2012.

[114] Yiming Zhang, Julian R. G. Evans, and Shoufeng Yang. Corrected values for boiling points and enthalpies of vaporization of elements in handbooks. *Journal of Chemical & Engineering Data*, 56(2):328–337, 2011.

Publications and conference talks

Peer reviewed publication

2018

- J.H. Bin, M. Yeung, Z. Gong, H.Y. Wang, **C. Kreuzer**, M.L. Zhou, M.J.V. Streeter, P. S. Foster, S. Cousens, B. Dromey, J. Meyer-ter-Vehn, M. Zepf and J. Schreiber. Enhanced laser-driven ion acceleration by superponderomotive electrons generated from near-critical-density plasma. *Physical review letters*, doi.10.1103/PhysRevLett.120.074801, 2018.

- T.M. Ostermayr, J. Gebhard, D. Haffa, I. Cermak, **C. Kreuzer**, J. Schreiber and P. Hilz. A transportable Paul-trap for levitation and accurate positioning of micron-scale particles in vacuum for laser-plasma experiments. *Review of Scientific Instruments*, doi:10.1063/1.4995955, 2018.

- F. H. Lindner, J. H. Bin, F. Englbrecht, D. Haffa, P. R. Bolton, Y. Gao, J. Hartmann, P. Hilz, **C. Kreuzer**, T. M. Ostermayr, T. F. Rösch, M. Speicher, K. Parodi, P. G. Thirolf and J. Schreiber. A novel approach to electron data background treatment in an online wide-angle spectrometer for laser-accelerated ion and electron bunches. *Review of Scientific Instruments*, doi:10.1063/1.5001990, 2018.

2017

- Y. Gao, J. H. Bin, D. Haffa, **C. Kreuzer**, J. Hartmann, M. Speicher. F. H. Lindner, T. M. Ostermayr, P. Hilz, T. F. Rösch, S. Lehrack, F. Englbrecht, S. Seuferling, M. Gilljohann, H. Ding, W. Ma, K. Parodi and J. Schreiber, An automated, 0.5 Hz nano-foil target positioning

system for intense laser plasma experiments, *High Power Laser Science and Engineering*, doi:10.1017/hpl.2017.10, 2017.

- F.H. Lindner, D. Haffa, J.H. Bin, F. Englbrecht, Y. Gao, J. Gebhard, J. Hartmann, P. Hilz, **C. Kreuzer**, S. Lehrack, T.M. Ostermayr, T.F. Rösch, M. Speicher, M. Würl, K. Parodi, J. Schreiber and P.G. Thirolf. Towards swift ion bunch acceleration by high-power laser pulses at the Centre for Advanced Laser Applications (CALA), *Nuclear Instruments and Methods in Physics Research Section B: Beam Interactions with Materials and Atoms*, doi:10.1016/j.nimb.2017.02.088, 2017.

- S. Seuferling, M.A.O. Haug, P. Hilz, D. Haffa, **C. Kreuzer** and J. Schreiber. Efficient offline production of freestanding thin plastic foils for laser-driven ion sources. *High Power Laser Science and Engineering*, doi:10.1017/hpl.2017.7, 2017.

2016

- T. M. Ostermayr, D. Haffa, P. Hilz, V. Pauw, K. Allinger, K. U. Bamberg, P. Böhl, C. Bömer, P. R. Bolton, F. Deutschmann, T. Ditmire, M. E. Donovan, G. Dyer, E. Gaul, J. Gordon, B. M. Hegelich, D. Kiefer, C. Klier, **C. Kreuzer**, M. Martinez, E. McCary, A. R. Meadows, N. Moschüring, T. Rösch, H. Ruhl, M. Spinks, C. Wagner and J. Schreiber. Proton acceleration by irradiation of isolated spheres with an intense laser pulse. *Phys. Rev. E*, doi:10.1103/PhysRevE.94.033208, 2016.

2015

- S. Palaniyappan, C. Huang, D. C. Gautier, C. E. Hamilton, M. A. Santiago, **C. Kreuzer**, A. B. Sefkow, R. C. Shah and J. C. Fernández. Efficient quasi-monoenergetic ion beams from laser-driven relativistic plasmas. *Nature Communications*, doi:10.1038/ncomms10170, 2015.

- J. H. Bin, W. J. Ma, H. Y. Wang, M. J. V. Streeter, **C. Kreuzer**, D. Kiefer, M. Yeung, S. Cousens, P. S. Foster, B. Dromey, X. Q. Yan, R. Ramis, J. Meyer-ter-Vehn, M. Zepf, and J. Schreiber. Ion acceleration using relativistic pulse shaping in near-critical-density plasmas. *Physical Review Letters* doi:10.1103/PhysRevLett.115.064801, 2015.

2014

- W. J. Ma, J. H. Bin, H. Y. Wang, M. Yeung, **C. Kreuzer**, M. Streeter, P. S. Foster, S. Cousens, D. Kiefer, B. Dromey, X. Q. Yan, J. Meyer-ter-Vehn, M. Zepf and J. Schreiber. Bright subcycle extreme ultraviolet bursts from a single dense relativistic electron sheet, *Physical Review Letters*, doi:10.1103/PhysRevLett.113.235002, 2014.

- M. Yeung, B. Dromey, S. Cousens, T. Dzelzainis, D. Kiefer, J. Schreiber, J. H. Bin, W. Ma, **C. Kreuzer**, J. Meyer-ter-Vehn, M. J. V. Streeter, P. S. Foster, S. Rykovanov and M. Zepf Dependence of laser-driven coherent synchrotron emission efficiency on pulse ellipticity and implications for polarization gating

2013

- J. Braenzel, C. Pratsch , P. Hilz, **C. Kreuzer**, M. Schnürer, H. Stiel and W. Sandner. Thickness determination of freestanding ultra-thin foils using a table top laboratory extreme ultraviolet source, *Review of Scientific Instruments*, doi:10.1063/1.4807153, 2013.

- S. Steinke, P. Hilz, M. Schnürer, G. Priebe, J. Bränzel, F. Abicht, D. Kiefer, **C. Kreuzer**, T. Ostermayr, J. Schreiber, A. A. Andreev, T. P. Yu, A. Pukhov and W. Sandner. Stable laser-ion acceleration in the light sail regime. *Physical Review Accelerators and Beams*, doi:10.1103/PhysRevSTAB.16.011303, 2013.

Presentations on international conferences

- Preparing for 3 PW at the Centre for Advanced Laser Applications (CALA) in Munich: Laser damage of optics in vacuum under the microscope, *Laser damage symposium*, Boulder, Colorado, (2016)

- A Paul trap for levitated micron to submicron sized particles, (Stand-in for Peter Hilz), *5th Target fabrication workshop*, St. Andrews, Scotland, (2014)

- Freestanding thin film production at LMU Munich for laser ion acceleration, *4th Target fabrication workshop*, Mainz, Germany (2012)

Acknowledgments

At this point, I would like to take the opportunity to thank all my colleagues, collaborators and all my friends that supported me during my PhD time and helped me to successfully complete this thesis.
First of all I would like to thank my supervisor **Prof. Dr. Jörg Schreiber** for giving me the opportunity to be part of his group and also for the freedom to focus on technological developments in this Phd-thesis.
I also want to thank **Prof. Dr. Katia Parodi** for giving us laser ion accelerators insight into real world medical physical problems.
I want to thank **Prof. Dr. Ulrich Schramm** for agreeing to be my second referee of my PhD thesis.
Special thanks goes to **Prof. Dr. Paul Bolton** for various fruitful discussions and for sharing stories of his scientific career.
Special thanks go to all my colleagues. I want to thank **Peter Hilz, Dr. Tobias Ostermayr, Daniel Haffa, Andreas Welmüller, Markus Poitner, Franz Englbrecht, Florian H. Lindner, Matthias Alexander Otto Haug, Sebastian Herr, Daniel Hahner, Sebastian Seuferling, Jens Hartmann, Martin Speicher, Johannes Gebhard, Ying Gao, Matthias Würl, Victor Gisbert** and **Dr. Jianhui Bin** for the great time together. I always enjoyed working with you guys.
Special thanks go to my Master students **Andreas Welzmüller**, **Victor Gisbert** and **Sebastian Herr** and my Bachelor students **Tobias Rumpf**, **Maximillian Kögler** and **Christian Weindl** for supporting my projects and the fun time together. This is especially true for **Andreas Welzmüller** who supported my projects even with his personal equipment.
I want to thank **Peter Hilz** for sharing all his knowledge about vacuum systems, target production and of course for the countless funny projects and discussions about topics that really matter. No snowman was safe from us.
Dr. Tobias Ostermayr deserves special thanks for the time at the Texas petawatt laser and for countless motivations during the writing of this thesis.
Special thanks go to **Daniel Haffa** for leading the LION experiments in LEX and for is endless perseverance at dealing with problems during the experi-

ment.
I want to thank the technological lab: **Jerzy Szerypo, Hans-Jörg Maier, Dagmar Fischke, Ulli Friebel** and **Simon Stork** for their support and sharing of their knowledge about targets.
The mechanical workshop around **Rolf Öhm** deserves special thanks for their help in realization of simple to very complicated constructions.
I want to thank **Verena Priesack** for proof reading this thesis.
A very warm word of thanks goes to my girlfriend **Resi** who always supported me during this phd work. Thank you very much!
Zu guter Letzt möchte ich meiner Familie für ihre unablässige Unterstützung meines Werdegangs danken. **Hannelore** und **Michael Kreuzer** danke ich von Herzen für ihre finanzielle und seelische Unterstützung während all der Jahre. Meinen Brüdern **Tobias**, **Johannes** und **Daniel Kreuzer** möchte ich ebenso für ihren Rückhalt bedanken. Ohne meine Familie wäre diese Doktorarbeit nicht möglich gewesen.